UiT
THE ARCTIC
UNIVERSITY
OF NORWAY

FACULTY OF SCIENCE AND TECHNOLOGY

Department of Geology

Fluid flow features and gas hydrates in the outer Vøring Basin

—

Carita Elisabeth Eira Varjola

EOM-3901 Master's thesis in Energy, Climate and Environment

December 2015

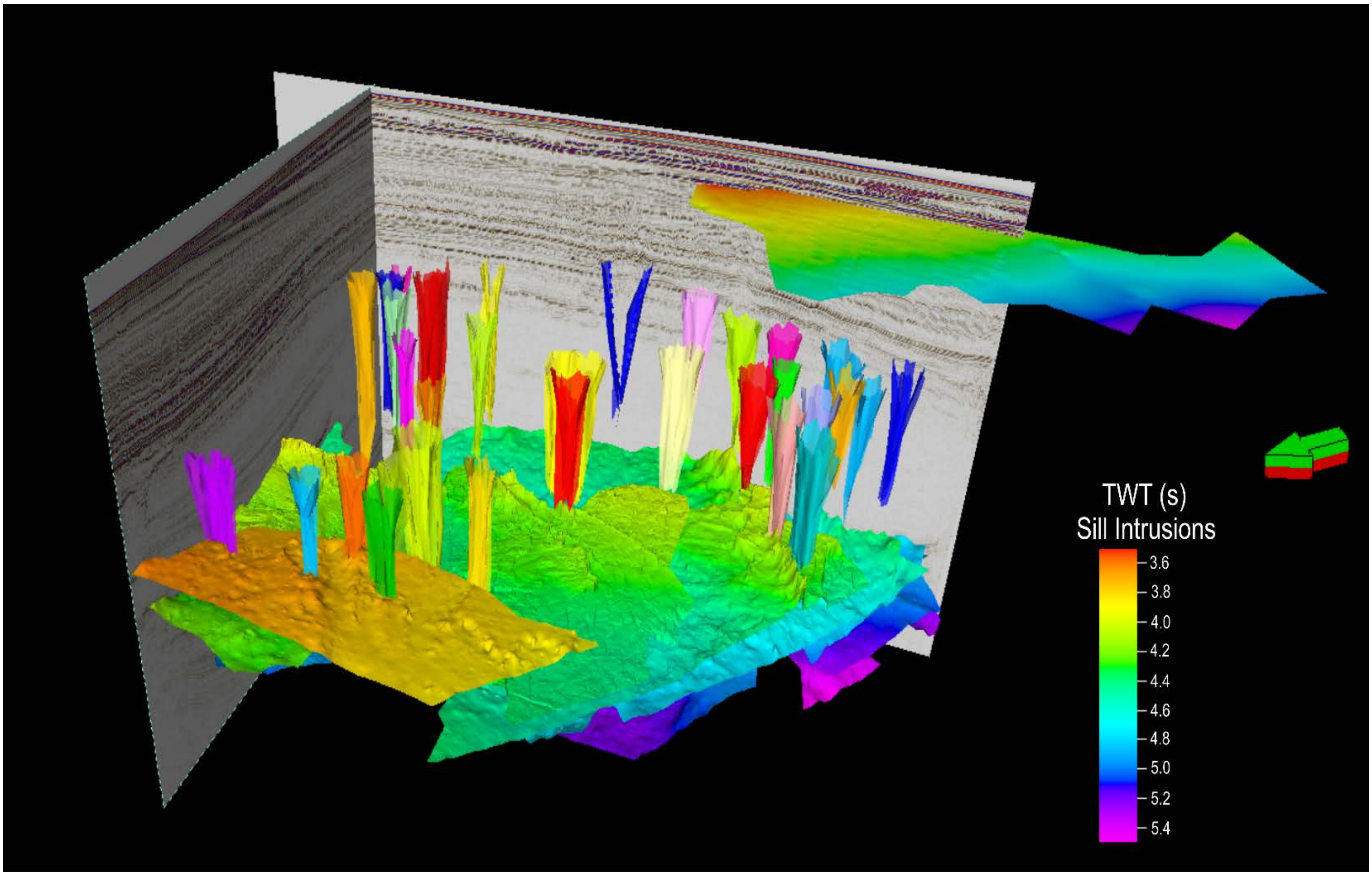

FACULTY OF SCIENCE AND TECHNOLOGY
Department of Geology

Fluid flow features and gas hydrates in the outer Vøring Basin

—
Carita Elisabeth Eira Varjola

EOM-3901 Master's thesis in Energy, Climate and Environment

December 2015

Supervisor:
Dr. Stefan Bünz, UiT- The Arctic University of Norway

Cover page picture:

Interpretations done by Carita Elisabeth Eira Varjola on the public 3D seismic data set ST0827 from StatoilHydro

Abstract

The 3D seismic survey ST0827 in the outer Vøring Basin reveals a complex fluid flow system consisting of hydrothermal vents, polygonal faults and acoustic pipes. The polygonal faults are bound to the fine-grained Top Brygge Formation and ooze-dominated Kai Formation. The Kai Formation is overlain by the Naust Formation, in which glacigenic debris flow units are observed. As polygonal faults can be sensitive to movement, the rapid loading from the debris flows is assumed to have reactivated polygonal faults in the area, thus allowing fluid to flow through the faults. Fluid flow indicators such as bright spots and acoustic masking in the proximity of the faults imply that fluid flow along faults has occurred, thus making polygonal faults one of the main controlling mechanisms for fluid flow development in the area. Above the termination of faults, high amplitude anomalies are found within the interbedded debris flow deposits, implying entrapment of gas. Glacigenic deposits make up one of the accumulation mechanisms in the study area.

The north-north-western part of the study area is not affected by glacigenic deposits. Pockmarks would be expected, but even with acoustic masking extending all the way to the seabed, the seismic character of the seafloor reflection inhibits pockmark-identification.

In addition to focussed fluid flow features, the 3D seismic data enabled identification and mapping of a gas-hydrate related bottom-simulation reflector (BSR). The BSR marks the base of the gas hydrate stability zone (BGHSZ). The BSR has a behaviour in which it crosscuts the sedimentary strata. Enhanced reflections terminate against the polarity-reversed BSR-reflection. The formation and origin of the gas hydrate and the gas hydrate-related BSR is closely related to the fluid flow in the area. A fluid flux of thermogenic origin is believed to result from the hydrothermal vents and sill intrusions. However, biogenic methane flux from the Kai Formation is also suggested as a source. The observed BSR appears between the modelled BGHSZ for 100% methane and the BGHSZ for 99% methane including 1% ethane. This supports the theory for the origin of the hydrate-forming gases being a combination of thermogenic gases from deeper depths, and biogenic gases from the Kai Formation.

Acknowledgements

The finalisation of this master thesis would not have been possible without the help and contributions of others.

I hereby want to express my sincere gratitude to my supervisor, Assoc. Prof. Stefan Bünz, for giving me the opportunity to write this thesis, for his valuable advice, assistance and corrections.

I am also very grateful to Kate Alyse Waghorn for providing me with stratigraphic interpretations.

I also want to thank my fellow students and friends whom I have had the pleasure to work and socialise with over the course of my studies. You have all made my study time memorable. The good discussions and many laughs are greatly appreciated.

Finally, I want to thank my family for all the help and continuous support they have given me during my studies.

With great gratitude,

Carita Elisabeth Eira Varjola

TABLE OF CONTENTS

1 Introduction

1.1 Objective

The first goal of this paper is to better understand controlling mechanisms for the occurrence and development of focussed fluid flow features (faults, pipes, chimneys and/or hydrothermal vents) and their relationship to the structural development of the region. A second major goal is to map a gas hydrate-related bottom-simulating reflector (BSR) and understand its origin.

The main part of the work involves interpretation of 3D seismic data from the Vøring Basin to identify fluid flow features and BSR. In addition to the main 3D data set, 2D seismic lines have been used when mapping the extent of gas hydrates. To support the work of identifying and mapping gas hydrates, modelling of the gas hydrate stability zone (GHSZ) is done based on the geothermal gradient and ocean bottom temperatures found in the region. Well-log data has been used for correlation and as an aid in stratigraphic interpretation.

1.2 Structure and outline

The thesis is structured in 7 chapters.

Chapter 1 starts with presenting the objectives and structure of the paper. Examples of how fluid flow and gas hydrates can be both hazardous and beneficial will be given to show their significance.

Chapter 2 describes the fundamental theory behind fluid flow and presents some fluid migration models. The chapter also includes theory about gas hydrate formation and dissociation. The last part of the chapter presents basic theory behind seismic reflection.

Chapter 3 consists of a presentation of the study site in terms of its tectonic development and stratigraphy. Previous work will be presented as well.

Chapter 4 gives an overview of the data and methods applied in the paper. The chapter includes seismic indications for e.g. fluid flow and gas hydrates.

Chapter 5 presents the results obtained from seismic interpretation and modelling.

Chapter 6 discusses the observations from chapter 5 in terms of how they are related. The chapter aims to explain the connection between fluid flow and gas hydrates.

Chapter 7 summarises the work with some concluding remarks based on the results and discussion.

1.3 The significance of fluid flow and gas hydrates

There is extensive ongoing research on subsurface fluid flow and gas hydrates as they have a great variety of implications. The implications can be both beneficial and hazardous. Investigations of fluid flow and gas hydrates are carried out in relation to e.g. petroleum exploration and production, global climate change and marine biology. The significance of fluid flow and gas hydrates also serves as the motivation to study them. In this section there will be examples of how fluid flow and gas hydrates can be both hazards and benefits. Starting with the hazards, Figure 1.1 shows a summary of issues regarding gas hydrates. These issues will be discussed in detail in the following subsections.

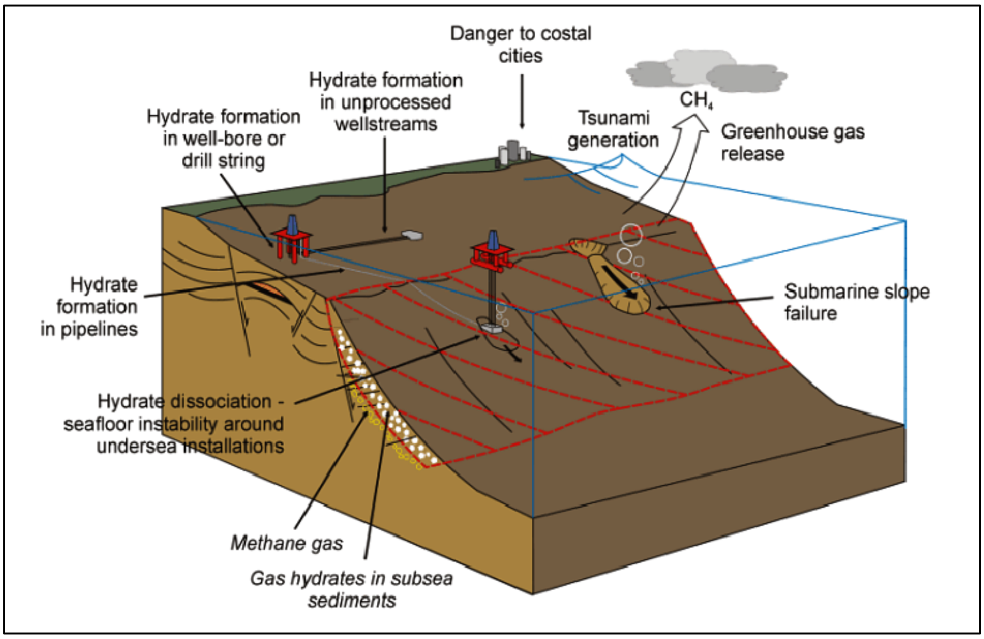

Figure 1.1: Major issues of gas hydrates. Courtesy of the Center for Gas Hydrate Research at the Institute of Petroleum Engineering, Heriot-Watt University (HWU, 2015)

1.3.1 Fluid flow and gas hydrates as geohazards

In Figure 1.1 submarine slope failure is shown as one of the implications from gas hydrates. Submarine slides can have negative impacts on offshore installations such as platforms and pipelines, but the associated tsunamis also impose a risk for coastal cities (Bondevik et al., 2005; Judd & Hovland, 2007). Slope failure occurs when gravitational forces (vertical stress), which pull sediment masses downslope exceed the resisting forces (shear strength)(Judd & Hovland, 2007). Both dissociation of gas hydrates and fluid flow reaching shallow subsurface depths or the seabed are hazardous. Fluid flow becomes a hazard when thermogenic gas sources are present and gas migrates upwards to porous layers capped by impermeable layers. Depending on drainage conditions, this can result in excess pore pressure and a reduction of the effective shear strength (Judd & Hovland, 2007). Gas hydrates become a hazard when they are not longer in a stable state and start decomposing. The solid ice-like structure changes to a liquid and gas mixture(Kvenvolden, 1999). In some cases the gas escapes through the sediment, leaving water behind. This results in sediment liquefaction giving weak layers with a reduced shear strength (Judd & Hovland, 2007). For the case where the gas is not able to escape, it results in excess pore pressure, having the same result as discussed above for fluid flow. Figure 1.2 shows a model of how sediments can break off and slide down slope. The decomposed hydrate layer acts as a gliding plane (McIver, 1982). An acknowledged fact seems to be that submarine slides related to gas (fluid flow) and gas hydrates occur in a combination with several other factors. These factors could be rapid sedimentation, cyclic loading, sea level changes, water mass temperature changes and earthquakes (Bryn, Berg, Forsberg, Solheim, & Kvalstad, 2005; Bryn, Berg, Lien, & Solheim, 2005; Judd & Hovland, 2007; McIver, 1982; Mienert et al., 2005; Rise et al., 2006).

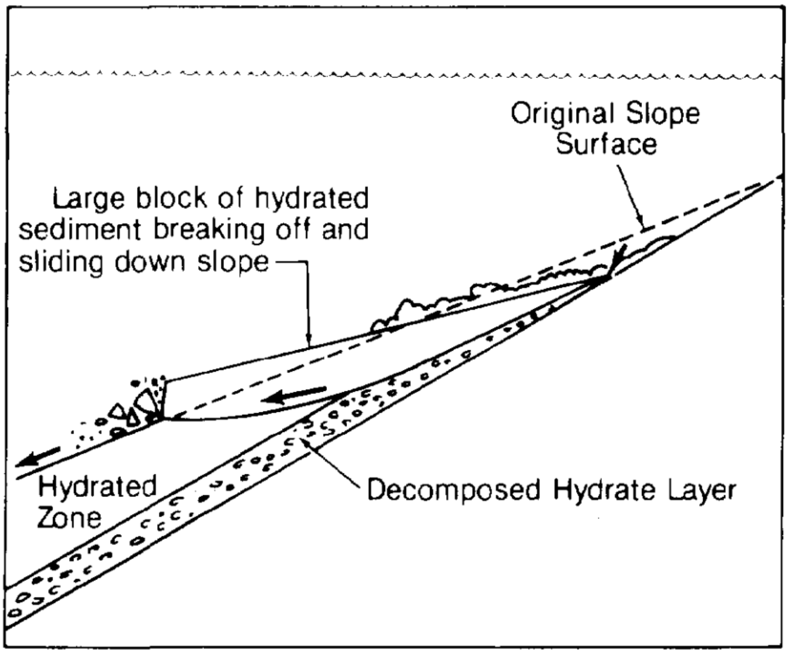

Figure 1.2: Model for mass movement. A block of sediment sliding down slope along a glide plane set up by a layer with hydrate decomposition. From McIver (1982).

Gas in shallow sediments, either coming from fluid flow or the dissociation of gas hydrates, imposes a risk not only in slope settings. In shelf areas, fluid flow and hydrate dissociation can create gassy sediments with a greater compressibility than that of the same sediment without the gas. This can cause problems for heavy installations (Judd & Hovland, 2007).

1.3.2 Fluid flow and gas hydrates as drilling and production hazards

Fluid flow itself does not directly impose a risk for drilling or production. It is however an important factor in gas accumulation. Such accumulations, if overpressured, can give blowouts. Overpressured gas is one of the main hazards in offshore drilling (Judd & Hovland, 2007).

Now to gas hydrates. Drilling through hydrates is not hazardous itself. The biggest concern with gas hydrates in terms of it being a drilling hazard seems to be hydrate dissociation during drilling. Conventional rotary drilling operations can cause rapid pressure and temperature changes in the surrounding formations. A temperature increase can come from e.g. a hot drill bit, warm drilling fluids, or because high-temperature reservoir fluids rise through the well due to pressure differences. The changes in conditions can result in hydrate dissociation, which in turn can give uncontrolled gas leakage, borehole instability, collapsed casings and damaged drilling equipment (Judd & Hovland, 2007; Yakushev & Collett, 1992).

In production, gas-hydrate related problems have been known for long. As one of the first to report hydrates in the natural gas industry, E.G Hammerschmidt (1934) wrote a paper regarding formation of snow and ice-like solid compounds that partly or completely blocked the flow in pipes used to transport natural gas. Hydrates blocking flow is indeed one of the most common ways for hydrates to cause problems in production (Sloan, 2005; Sloan & Koh, 2007; Zerpa, Salager, Koh, Sloan, & Sum, 2011). Figure 1.3 shows a conceptual model of how hydrate formation leads to flow blockage. Hammerschmidt's pivotal discovery was followed by extensive studies on how hydrates form and how to inhibit their formation in pipes. With today's petroleum exploration and production moving progressively into colder and deeper waters, the challenges are vast and complex (Kvenvolden, 1999). Gas hydrates forming inside wells (casing, blowout preventer (BOP) or wellheads) give a variety of hazardous problems in addition to flow blockage. Problems can be loss of circulation in formation and drilling fluids, hindrance to drill string movement and removal of water from drilling fluids (Barker & Gomez, 1989).

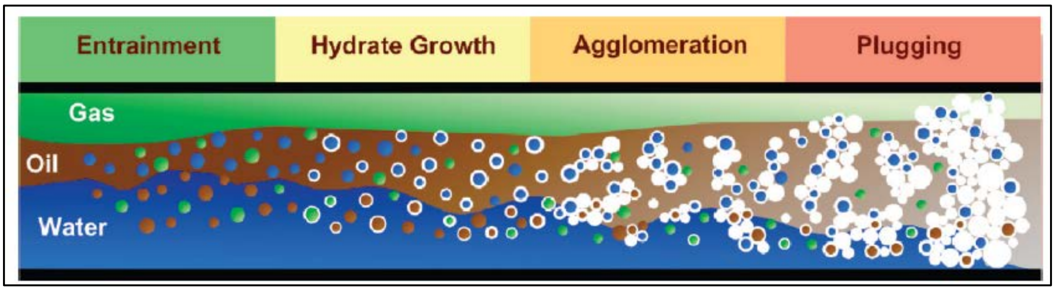

Figure 1.3: Model for hydrate formation in pipes with multiphase flow consisting of water, oil and gas. From Zerpa et al. (2011)

To deal with these problems, research on new technologies for transportation and storage of gas hydrates is needed. Future solutions such as the Cold Flow concept by SINTEF and NTNU are under development. The Cold Flow concept allows for controlled formation of gas hydrates for transportation of natural gas (Akpabio, 2013; Gudmundsson, 2002; Ilahi, 2006). It has been proposed that the cost of natural gas hydrate (NGH) transportation is lower than that of an equivalent liquefied natural gas (LNG) transport (Gudmundsson & Børrehaug, 1996; Taheri, Shabani, Nazari, & Mehdizaheh, 2014).

1.3.3 Gas hydrates as a climate hazard

Gas hydrates can also be a hazard for climate. If hydrates decompose, methane gets released. As discussed above, the dissociation of hydrates can come from many reasons. Two of them being elevation in ocean temperature and sea-level rise. How methane is transferred to the atmosphere is illustrated in Figure 1.4. Because methane is a greenhouse gas, a release of methane into the atmosphere will have a global warming effect. Global warming potentials (GWP) are used to compare the effect of different greenhouse gases. It compares the global warming effect from 1kg of a certain gas to 1 kg of CO_2. A time horizon needs to be defined because the lifetime of gases vary (Houghton, 2009). The GWP of methane is 20 times larger than that of CO_2 when using a 100-year time horizon (Kvenvolden, 1993). It their reports, IPCC operates with GWP of 25 for methane (IPCC et al., 2007).

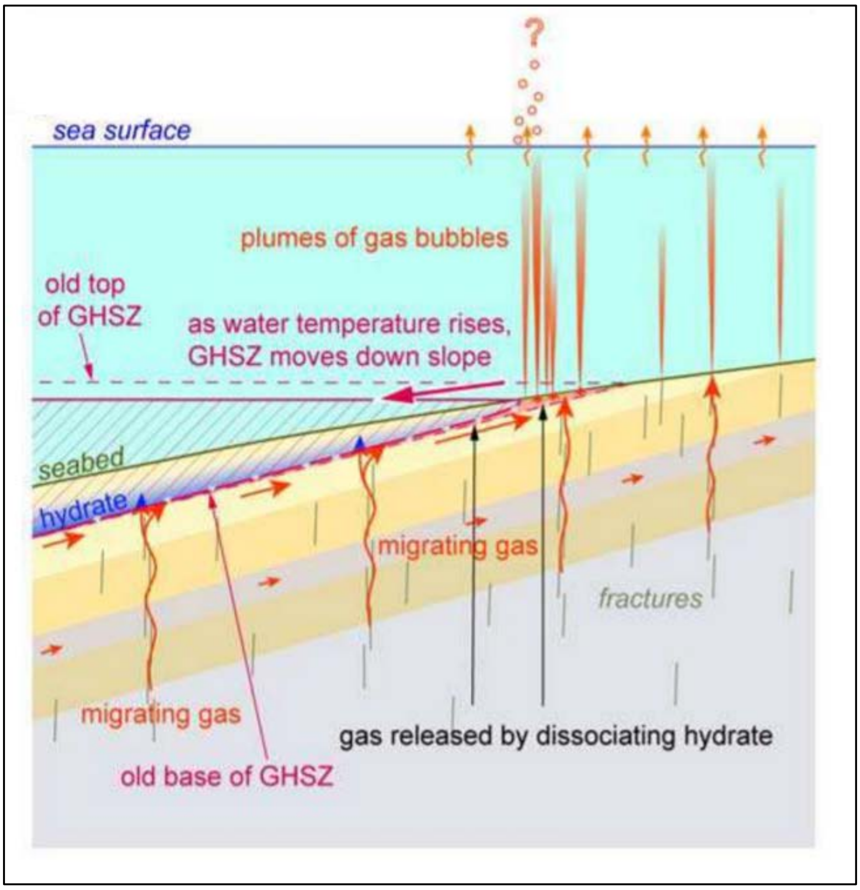

Figure 1.4: Illustration on how an increase in the seawater temperature can cause the gas-hydrate stability zone to move deeper, resulting in a dissociation of hydrate to methane and water. Methane may be released. From Westbrook et al. (2009)

1.3.4 Fluid flow as a benefit for petroleum exploration

Fluid flow can benefit us, as it can serve as an indicator for the presence of a hydrocarbon source and deeper prospective reservoirs. Fluid flow features can also indicate that the source rock is mature and that migration has taken place. This is important in hydrocarbon exploration (Heggland, 1998; Judd & Hovland, 2007).

1.3.5 Gas hydrate as an energy resource

The global demand for energy is increasing. This increase in energy demand comes from an overall growth in population and because highly populated areas such as Asia and Africa are under economic growth. It is projected that fossil fuels(coal, oil and natural gas) will make up 75-80% of energy sources in 2030 (EIA, 2013; Holditch & Chianelli, 2008; IEA, 2013). Natural gas is preferred over oil and coal as a fossil fuel because it produces less CO_2. The methane from gas hydrates can potentially solve the world's energy needs for many centuries (Demirbas, 2010; Makogon, 2010).

Gas hydrates are attractive as an energy resource firstly because of the enormous amount of methane that is trapped within them, secondly because of their wide geographical distribution (Kvenvolden, 1993, 1999; Ruppel & Noserale, 2012). Figure 1.5 shows the worldwide distribution of gas hydrates. Studies report that the carbon found in gas hydrates is larger than the carbon-amount present in all known deposits of coal, oil and natural gas (Demirbas, 2010; Judd & Hovland, 2007; Kvenvolden, 1993).

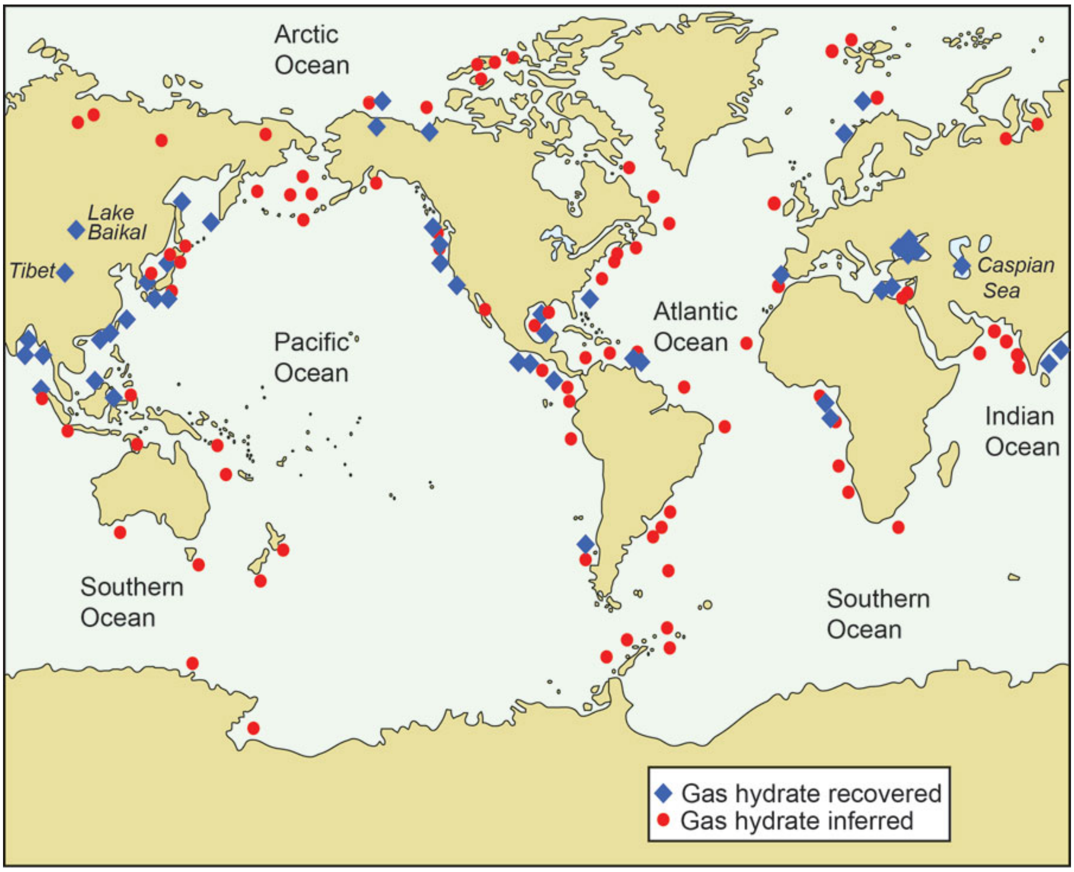

Figure 1.5: The worldwide distribution of gas hydrates. The figure distinguishes between sites where gas hydrate is inferred and sites where it has been physically recovered.
From Ruppel & Noserale (2012)

Gas hydrates will however not be viable as a resource without the technology to exploit them. The main technologies for hydrate production include technologies where hydrates are decomposed through pressure reduction, heat injection or by injection of inhibitors (Birkedal, 2013; Judd & Hovland, 2007; Moridis, 2003). There is also ongoing research on methane production from natural gas hydrates by CH_4-CO_2 replacement. This technology is promising as it allows production of methane and sequestration of carbon dioxide at the same time (Birkedal, 2013; Liu et al., 2013).

1.3.6 Benefits for marine biology

There are also benefits for the fishing industry as hydrothermal vents and fluid flows systems that reach the seabed can enhance the biological activity (Judd & Hovland, 2007; Westbrook et al., 2008) The activity around hydrothermal vents and deep-sea cold seeps includes chemosynthetic organisms like microbial mats and tubeworms. Organisms like snails, clams, mussels and other grazing animals then feed on the bacterial mats and tubeworms. Crabs and shrimp eating the grazers attract larger organisms like octopi and fish (Grassle, 1985; Judd & Hovland, 2007).

2 Fundamental theory

This chapter contains fundamental theory about the petroleum system, the dynamics of fluid migration, and theory for gas hydrates. The chapter also introduces the basic principle behind seismic reflection.

2.1 Petroleum system

The term petroleum covers natural gas, crude oil and bitumens (Judd & Hovland, 2007). A petroleum system is a system of geological elements and processes necessary for the generation and accumulation of hydrocarbons. The elements included in a petroleum system are source rock, reservoir, seal and overburden. The processes needed are generation, trap formation, migration and accumulation (Magoon & Dow, 1994; Selley, 1998). Figure 2.1 shows a petroleum system.

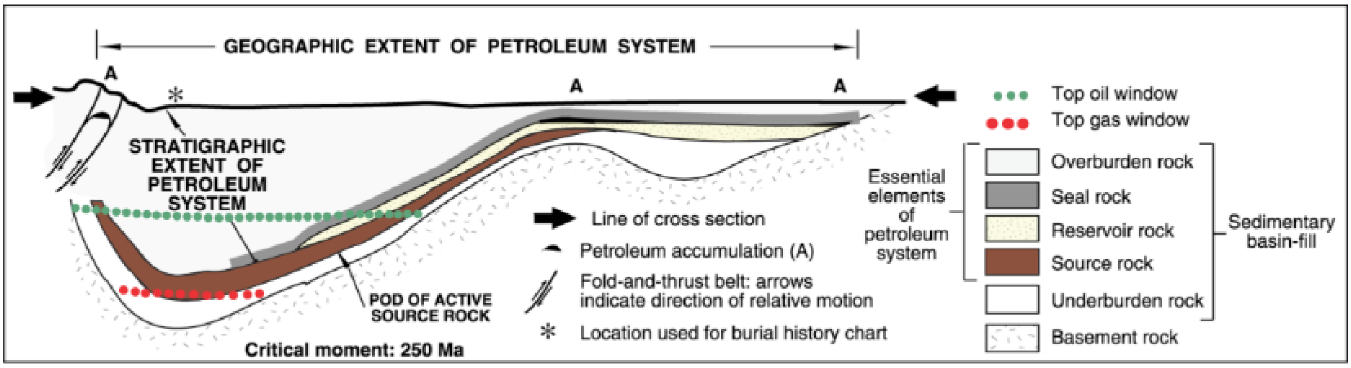

Figure 2.1: Illustration showing the main elements of a petroleum system. Modified from Magoon & Dow (1994).

The source rock, as the name implies, is the source of the petroleum. Source rocks are often clays or shales that contain large amounts of organic matter that can be turned into oil and gas if the rock reaches right temperature and pressure regimes (Selley, 1998). For hydrocarbons to accumulate, a trap needs to be formed before generation and migration occurs (Bjørlykke, 2010; Selley, 1998). The geometric arrangement of seal rock around and above a reservoir rock is known as a trap. The reservoir within a trap provides storage for hydrocarbons. A good reservoir rock is porous. This porosity can be depositional (primary) or diagenetic (secondary). The pores in a reservoir rock need to be connected to allow the movement of fluids, in other words it needs to have permeability. Sandstones and limestones are typical reservoir rocks. (Biddle & Wielchowsky, 1994; Selley, 1998). A seal is an impermeable rock lying above the reservoir in a way that allows hydrocarbons to accumulate. Shales are known to be good seals. There are four common categories of traps: Structural traps, stratigraphic traps, hydrodynamic traps and combination traps (Biddle & Wielchowsky, 1994; Bjørlykke, 2010; Selley, 1998).

Structural traps are formed by syn- to post-depositional processes such as folding, doming or faulting. Structural traps can be subdivided into fold (anticlinal) traps, traps associated with faults, traps associated with piercement (diapir) features and traps with any combination of the foregoing (Biddle & Wielchowsky, 1994; Bjørlykke, 2010). Figure 2.2 shows examples of structural traps. There are several varieties of the different trap types.

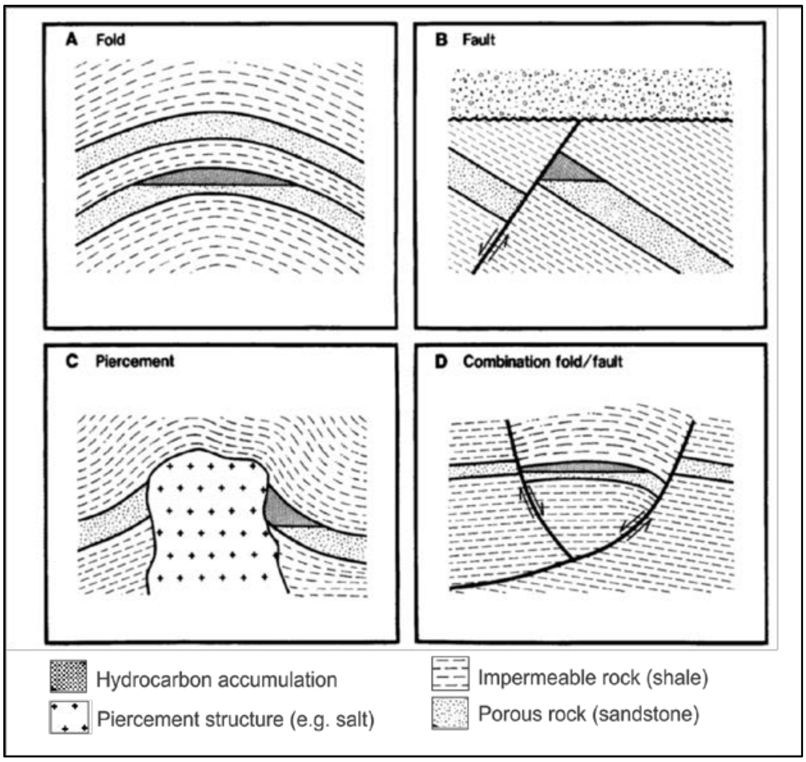

Figure 2.2: Structural traps. A) fold trap, B) fault trap, C) piercement (diapir) trap and D) fold/fault combination trap. Modified from Biddle & Wielchowsky (1994)

Stratigraphic traps are traps formed because of lithology differences. These traps can either be formed in association with unconformities, or they may be depositional and diagenetic traps. Figure 2.3 shows examples of stratigraphic traps caused by variation in deposition (Biddle & Wielchowsky, 1994). Facies variation, pinchout, channels, bars, dunes and reefs are all examples of depositional (primary) traps. Other kinds of traps that do not necessarily require an unconformity, are traps caused by diagenetic changes.

Diagenetic (secondary) traps are formed because of porosity/permeability variations (Figure 2.4A). Traps associated with unconformities can come from e.g. truncation (Figure 2.4B) (Biddle & Wielchowsky, 1994; Bjørlykke, 2010; Selley, 1998).

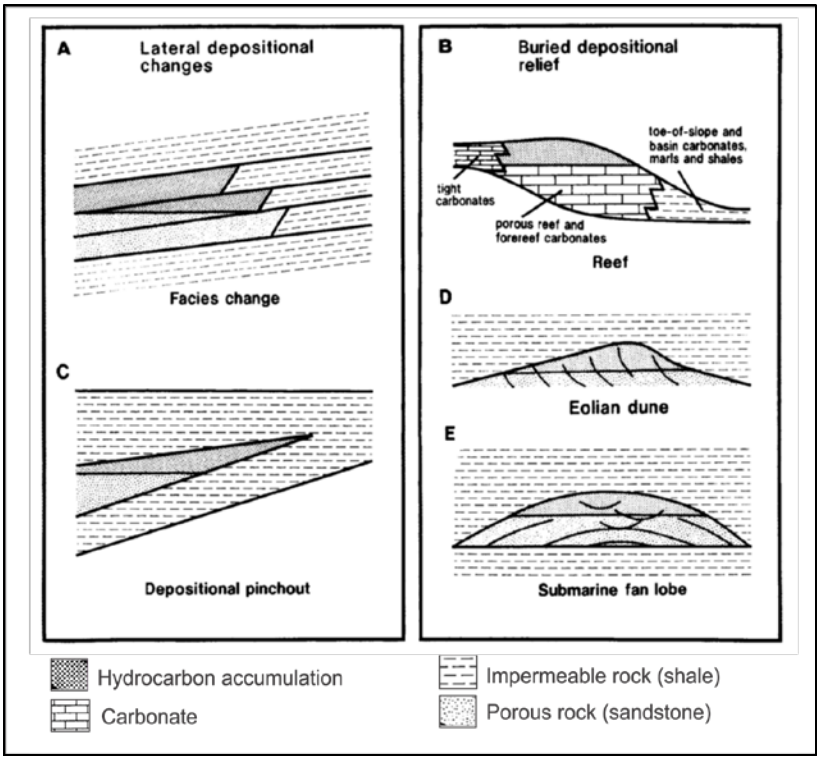

Figure 2.3: Depositional traps. A) trap caused from facies variation, B) trap caused by buried reef, C) trap caused from pinchout, D) trap caused by eolian dune and E) trap caused by submarine fan lobe. Modified from Biddle & Wielchowsky (1994)

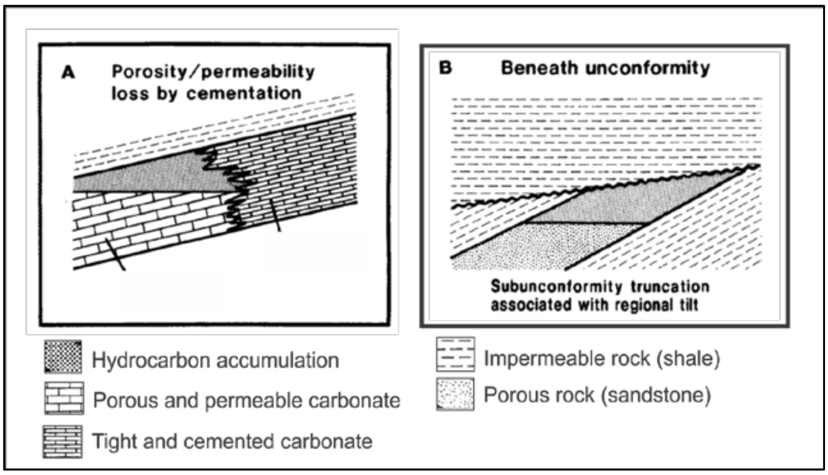

Figure 2.4 Stratigraphic traps. A) Diagenetic trap. B) Trap associatied with an unconformity. Modified from Biddle & Wielchowsky (1994)

2.2 Generation

Petroleum can have an organic or inorganic origin. Petroleum with an organic origin can be divided into two main classes: biogenic (microbial) and thermogenic hydrocarbons. These are also known as biotic hydrocarbons as they come from once living organisms. If the origin of petroleum is inorganic, it is termed abiogenic (abiotic) (Judd & Hovland, 2007; Selley, 1998).

2.2.1 Petroleum with organic origin

Petroleum with an organic origin contains organic matter that may be derived from algae or plants. For petroleum to be generated, organic matter needs to be preserved under anoxic conditions. If the preserved organic matter gets buried to depths with sufficiently high temperature and pressure it may transform into kerogen. The three major phases for this transformation are diagenesis, catagenesis and metagenesis.

Diagenesis occurs in shallow depths. During early diagenesis microbial activity is the main agent in transforming the organic matter. In this phase, kerogen forms by removal of functional groups as acid groups, aldehydes and ketones from the organic material. Water, carbon dioxide and nitrogen is also given off. The result of the diagenesis is that oxygen is removed. The kerogen is left with a higher hydrogen:carbon ratio than that of the initial compounds. During diagenesis, the most important hydrocarbon formed is methane. This process is also known as methanogenesis. This methane is often referred to as biogenic methane or microbial methane (Bjørlykke, 2010; Selley, 1998; Tissot & Welte, 1984). As burial continues and temperature and pressure increases, the second phase known as catagenesis starts. During this phase, the kerogen matures and releases petroleum. With increasing maturity, first oil gets released, then later thermogenic gas (sometimes referred to as “dry gas”) (Bjørlykke, 2010; Selley, 1998; Tissot & Welte, 1984). Metagenesis is the third stage. It occurs at very high temperatures and pressures, close to metamorphism. The last hydrocarbons in the kerogen are expelled. This is often methane. After this, the kerogen is inert and the source rock is overmature (Bjørlykke, 2010; Selley, 1998; Tissot & Welte, 1984).

Figure 2.5 shows the different phases of kerogen transformation. Note that biogenic gas forms at shallow depths with low temperatures, whereas thermogenic gas forms at much higher temperatures. Significant oil generation occurs at temperatures around 60-120ºC. This is known as the “oil window”. The “gas window” occurs at temperatures between 120 ºC and 225 ºC (Selley, 1998). Hydrothermal and igneous activity may influence the maturity of source rocks, and thus also the hydrocarbon generation (Bjørlykke, 2010).

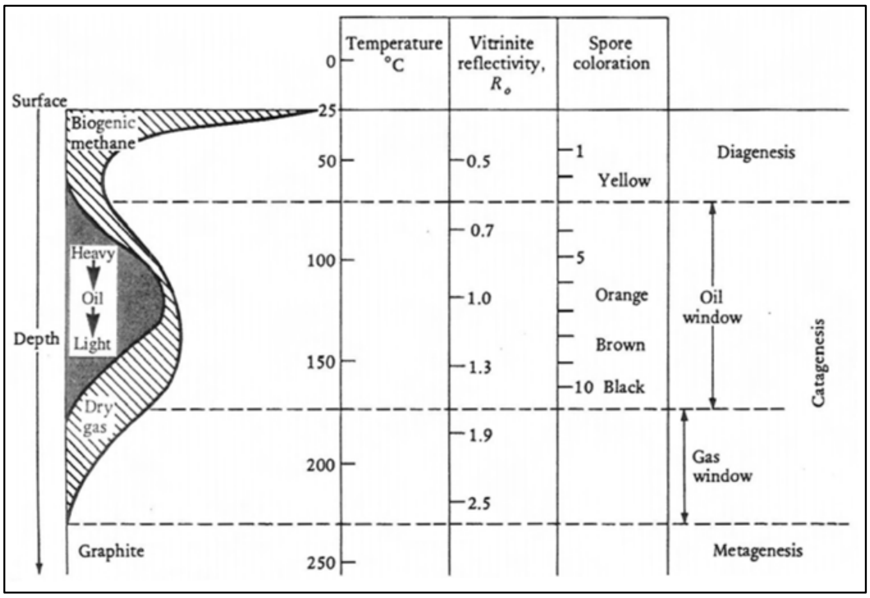

Figure 2.5: Maturation curve for hydrocarbons. Figure illustrates the relationship between depth, temperature and amount and type of petroleum generated. From Selley (1998)

2.2.2 Petroleum with inorganic origin

As mentioned above, the origin of hydrocarbons can be inorganic. Abiogenic (abiotic) petroleum is made through chemical reactions in igneous rocks (Selley, 1998). The abiogenic hydrocarbons are dominated by light hydrocarbons as methane, ethane, propane and butane. There are two main classes for the formation of abiogenic gas: magmatic processes and gas-water-rock reactions (Etiope & Schoell, 2014). Methane can be derived from the mantle through high temperature reactions but it can also be preserved in the mantle after being delivered by meteorites during the accretion of the Earth (Etiope & Schoell, 2014; Judd & Hovland, 2007). However, not all abiogenic gases are mantle-derived. Results show that a variety of low temperature gas-rock-water reactions can produce abiogenic gases, e.g Fischer-Tropsch Type (FTT) reactions (Etiope & Schoell, 2014; Selley, 1998; Sherwood Lollar et al., 2006). The Fischer-Tropsch synthesis is an industrial process in which CO_2 reacts with H_2 to produce synthetic hydrocarbons (Selley, 1998), but FTT reactions are also among the most common mechanisms for abiotic methane production in natural settings (Etiope & Schoell, 2014). The carbon dioxide needed in the reaction can come from e.g. metamorphism of carbonates whereas the hydrogen can come from the serpentinization of ultramafic rocks. Serpentization is the hydration of olivine and/or pyroxene. All FFT reactions are catalysed by metallic minerals (Ni, Fe, Co, Cr, Ru) and related oxides. Nickel and iron are some of the most abundant metals in ultramafic rocks (Etiope & Sherwood Lollar, 2013).

2.2.3 Identifying the origin

The most effective tool for differentiating elements of different origins is stable isotope analysis. For identifying the origin of hydrocarbons, the isotopes of carbon ($\delta^{13}C$) and hydrogen ($\delta^{2}H$) are commonly used (Etiope & Sherwood Lollar, 2013; Judd & Hovland, 2007). This can be used to distinguish between biogenic, thermogenic and abiogenic hydrocarbons.

A major component of both biotic and abiotic natural gas is methane. The focus in terms of identifying the origin will therefore be on CH_4. There are certain standards used when investigating isotope compositions of $\delta^{2}H$ and $\delta^{13}C$ in methane, namely Vienna Pee Dee Belemnite (VPDB) and Vienna Standard Mean Ocean Water (VSMOW), respectively. Figure 2.6 shows a “Schoell Plot”. A “Schoell plot” can be helpful in identifying the origin of methane. A “Schoell Plot” can be inconclusive, but is often used as a first step in determining whether gas is biotic or abiotic. The use of noble gases (helium isotopes), assessment of the molecular distribution of the hydrocarbon alkanes (Schulz-Flory distribution tests), the molecular and isotopic composition of associated gases (other than hydrocarbons and CO_2) and methane versus ethane mixing plots are additional investigations that can be carried out to determine the origin of methane (Etiope & Sherwood Lollar, 2013).

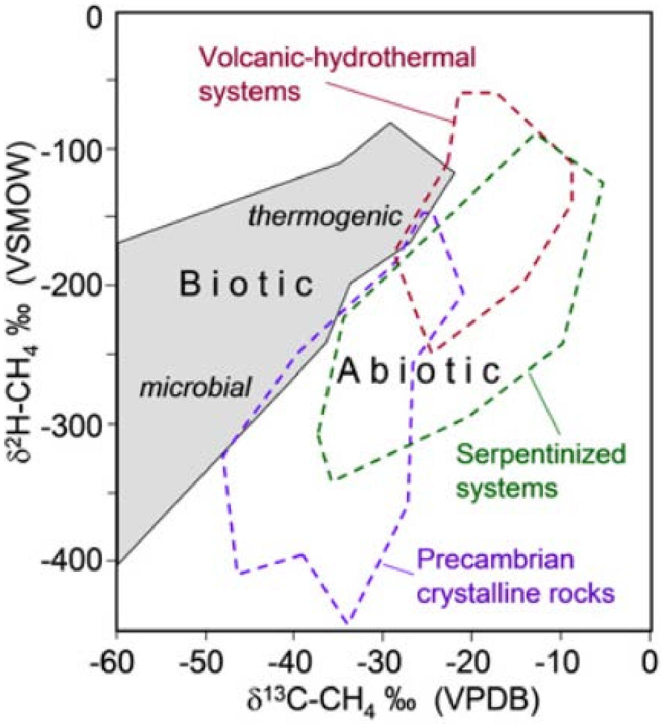

Figure 2.6: Schoell Plot showing $\delta^{13}C$ versus $\delta^{2}H$ for methane. The plot allows us to distinguish between biotic (microbial and thermogenic) and abiotic methane. It also provides insight into whether the abiotic methane originates from volcanic-hydrothermal systems, serpentinized systems or Precambrian crystalline rocks. From Etiope & Schoell (2014)

2.3 Fluid migration dynamics

Fluid migration is the movement of fluids in the subsurface. For petroleum related migration, an important distinction is made between primary, secondary and tertiary migration (Figure 2.7). The expulsion of petroleum from a source rock into surrounding rocks is known as primary migration. The mechanisms behind primary migration are widely debated, and will not be discussed in this thesis. The subsequent movement of oil and gas within carrier beds, the reservoir rock, is called secondary migration (Bjørlykke, 2010; Selley, 1998). Tertiary migration is when hydrocarbons are remobilised and move from one reservoir to another or all the way to the surface (Durand, 1988). The movement of hydrocarbons out from a trap is also known as dismigration (Tissot & Welte, 1978). The following sections will present the dynamics behind subsurface fluid migration with a focus on secondary and tertiary migration. The main driving and resisting forces will be presented.

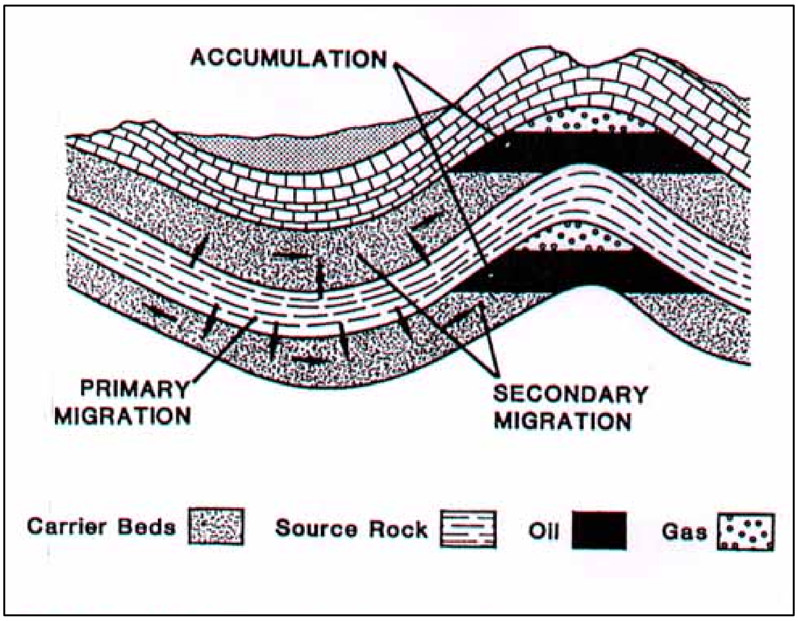

Figure 2.7: Sketch of a source rock, carrier beds and impermeable seal. Note the distinction between primary and secondary migration. From Tissot and Welte (1984)

2.3.1 Subsurface pressure

Pressure can be caused due to the weight of overlying rock (lithostatic pressure). In the subsurface we can also find pressures caused by fluids. These include hydrostatic pressure, hydrodynamic pressure and pore pressure. For hydrodynamic pressure, it is common to look at the gradient, also known as fluid potential gradient. This is caused by fluid flow. Groundwater flow is one of the forces driving hydrocarbon migration (Bjørlykke, 2010; Hindle, 1997).

Hydrostatic pressure is caused by the weight of a column of fluid at rest. The atmospheric pressure (P_a) at sea level needs to be added to the pressure exerted by the fluid column (Selley, 1998). Pressure exceeding the hydrostatic pressure is termed overpressure. Mechanisms such as differential compaction, sedimentation or generation of biogenic or thermogenic gas can cause overpressure (Berndt, 2005; Osborne & Swarbrick, 1997). Equation 1 shows the hydrostatic pressure exerted by a fluid with density ρ and a column height h where g is the gravitational acceleration.

$$P = \rho g h + P_a \qquad \textit{(Equation 1)}$$

From basic physics, we know that pressure is equal to force per unit area. Rearrangement gives us that force is equal to pressure multiplied with area. The force (equation 2) exerted by a fluid column on a surface with given area is:

$$F = pA = \rho g h A = \rho g V \qquad \textit{(Equation 2)}$$

The force at a given point due to a body of fluid is thus given by the density(ρ) of the fluid, the volume(V) of the fluid, times the gravitational acceleration.

2.3.2 Buoyancy force

During expulsion from the source rock, hydrocarbons may form small oil globules or gas bubbles. When two immiscible fluids (hydorcarbons and water) occur in a rock, a buoyant force is created due to density differences (Matthews, 1996; Schowalter, 1979). The density of oil and gas are lower than that of water. The dominant mechanism of fluid migration in the subsurface is buoyancy. Buoyancy force (BF) is a function of the density contrast between fluids (Judd & Hovland, 2007). The case for gas bubbles in water will be used as an example, but a similar equation can be derived for the oil-water case. Inserting the densities of water and gas into Equation 2 gives:

$$BF_b = \frac{4}{3}\pi r_b^3 \left(\rho_{water} - \rho_{gas}\right) \cdot g \qquad \textit{(Equation 3)}$$

Where BF_b is the buoyancy force of a gas bubble, r_b is the radius of the gas bubble, ρ_{water} is the density of seawater, ρ_{gas} is the density of the gas and g is the gravitational acceleration. The density of seawater varies with temperature and salinity, but is typically typically 1024 kg/m^3. Gases are compressible and the density thus varies with temperature and pressure (Judd & Hovland, 2007). The density of e.g. methane can be 200-300 kg/m^3 beneath 3-4 km of water (Clennel, Judd, & Hovland, 2000).

In the subsurface hydrocarbons need to migrate through the pores of rock. This sets up forces resisting the movement of fluids. As long as the buoyancy force is greater than the resisting forces, fluid can migrate. The forces acting against the buoyancy forces and migration are the capillary forces and forces set up by low permeable rocks (Bjørlykke, 2010; Schowalter, 1979). These forces will be explained in the following sections.

2.3.3 Capillary force

Capillary forces are set up by capillary pressure that arises when fluid is forced through the pore throats of rocks (Figure 2.8). The factors determining the magnitude of capillary pressure is the radius of the pore throats of the rock, the hydrocarbon-water interfacial tension (or surface tension), and wettability (Berg, 1975; Schowalter, 1979). Capillary pressure is commonly given with the following equation:

$$P_c = \frac{2\gamma}{r} \qquad \textit{(Equation 4)}$$

Where γ is the interfacial tension between hydrocarbon and water and r is the radius of curvature of the drop (Berg, 1975). The interfacial between gas and water is 5-35 dynes/cm, whereas between oil and water it is 5- 35 dynes/cm. The capillary pressure is greater for the gas-water case than for the case with oil-water. Note however that the buoyancy force is much bigger for the gas because of the low density of gas (Bjørlykke, 2010).

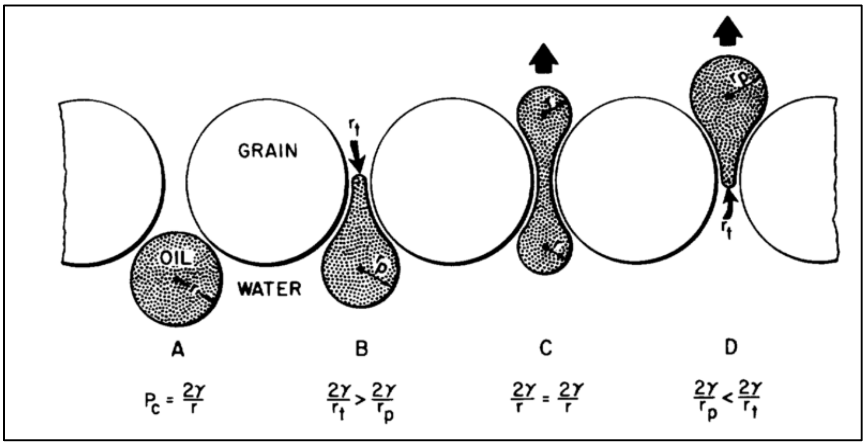

Figure 2.8: Illustration of oil globule migrating through pores in a water-wet rock. r_t denotes the radius of the pore throat, while r_p denotes the radius of the pore in which the oil globule is initially sitting. From Berg (1975)

2.3.4 Darcy's law

As mentioned, subsurface fluids will migrate through porous spaces in rocks. The resistance of flow of a fluid in porous media is known as permeability. The lower the permeability, the higher will the force which is resisting fluid migration be (Bjørlykke, 2010; Selley, 1998).

Fluid flow through porous and permeable medium is described by Darcy’s law as follows:

$$\frac{Q}{A} = \frac{-\kappa}{\mu} \nabla \mathrm{P} \qquad \textit{(Equation 5)}$$

where Q is the volumetric flow per unit sectional area A, κ is the intrinsic permeability, μ is the viscosity of a fluid and ∇P is pressure gradient (Clennel et al., 2000). Other forms of this equation use fluid potential ∇Φ instead of pressure gradient, but the unit for the two is the same. Fluids flow from higher to lower fluid potentials (Bjørlykke, 2010; England, Mackenzie, Mann, & Quigley, 1987). The intrinsic permeability relates solely to the properties of the rock. Permeability can also be given as relative (effective) permeability which is the permeability of one immiscible fluid in the presence of another fluid, compared to the permeability with 100% saturation of one fluid (Bjørlykke, 2010; Clennel et al., 2000; Selley, 1998). In marine sediments, the permeabilities range from $10^{-8}\mathrm{m}^2$ in sand and $10^{-19}\mathrm{m}^2$ in consolidated muds. The permeabilities in deep continental margin sediments typical for gas hydrates are around $3 \cdot 10^{-16}\mathrm{m}^2$ to $3 \cdot 10^{-16}\mathrm{m}^2$ (Clennel et al., 2000; Clennell, Hovland, Booth, Henry, & Winters, 1999).

2.3.5 Fluid flow mechanisms

The driving and resisting forces for fluid migration in the subsurface have now been presented. There are however several mechanisms for this migration.

2.3.5.1 Advection

The transport mechanism for a substance due to a fluids bulk motion is known as advection. This transport happens because of pressure differences. The substance (i.e. silt, pollutants, gas, oil) will be totally immersed in water. Both oil and gas advection exists, but focus will here be on the advective flux of gas. An advective flux is the product of volumetric flow rate(Equation 5) and the concentration of the substance in solution, e.g. methane in water. When inserting the permeabilities for marine sediments mentioned above into Equation 5, low flow velocities are obtained. Low flow velocities combined with e.g. the low solubility of methane results in the advective flux of methane being low (Clennel et al., 2000; Judd & Hovland, 2007).

If flow occurs through cracks, pipe-like features or highly permeable layers the “cubic law” can be used to obtain the flow velocity. The flow(Q) can in this case be calculated using Poiseuilles’ law:

$$Q = \frac{\pi r^4}{8\mu} \frac{\Delta P}{l} \qquad \textit{(Equation 6)}$$

where r is the radius and l is the length of the pipe (or crack), μ is the viscosity of the fluid and ΔP is the pressure difference between the top and bottom of the pipe. Provided that there is an excess pressure at depth, the flow rates may become higher (Clennel et al., 2000; Judd & Hovland, 2007).

2.3.5.2 Diffusion

If the pore water in the subsurface is not in motion, diffusion of gases can occur. Diffusion is the net flow of molecules due to a concentration gradient (Figure 2.9). Diffusion will go from high to low concentrations. Diffusive flux can be calculated using Fick’s first law:

$$J = -D\, \nabla \mathrm{c} \qquad \textit{(Equation 7)}$$

where J_g is the flow rate of gas per unit area, D is the diffusion coefficient or diffusivity and ∇c_g is the concentration (Berndt, 2005; Clennel et al., 2000; Schroeder, 2000).

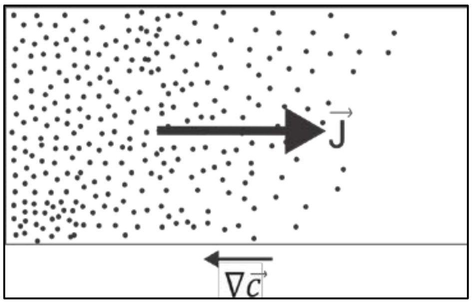

Figure 2.9: Diffusion of gas. Note how diffusion goes in the opposite direction of the concentration gradient.

Because the gas concentration gradients often are small, diffusion is very inefficient at transporting gas over long distances. It is a slow process and will disperse the gas more than concentrate it. Diffusion is a defocused leakage mechanism (Løseth, Gading, & Wensaas, 2009) The presence of diffusion is however ubiquitous in systems that are out of chemical and thermal equilibrium (Clennel et al., 2000).

2.3.4.3 Convection

Convection is the heat transfer caused by the bulk motion of a fluid (Schroeder, 2000). The motion is caused by fluids expanding or contracting due to heating or cooling, respectively. If a fluid is heated from below, or cooled from above, convection occurs as an overturning motion (Marshall & Plumb, 2008). For the scope of this thesis, hydrothermal systems driven by convection are of interest. Hydrothermal systems are common at divergent plate boundaries, but can also exist because of intraplate igneous activity. Igneous activity, such as sill intrusions in sedimentary basins may occur at passive continental margin (Jamtveit, Svensen, Podladchikov, & Planke, 2004; Judd & Hovland, 2007).

2.4 Fluid migration models

Fluids in the subsurface will migrate in advection, diffusion or convection according to the driving and resisting forces mentioned in the previous sections. As a recapitulation, the migration is greatly dependent on the fluid potential gradient (or pressure gradient) as explained by Darcy's law. Buoyancy forces due to density differences are the main driving forces for fluid flow, but groundwater flow may also play a role. Capillary forces put up by pore throats give a resistance to flow (Clennel et al., 2000; England et al., 1987; Hindle, 1997; Judd & Hovland, 2007; Selley, 1998). Fluids can migrate laterally, or vertically through pathways such as faults, chimneys and pipes. These migration models will be discussed in the following sections.

2.4.2 Vertical migration

Vertical migration of hydrocarbons occurs when the driving forces for migration are greater than the excess capillary pressure of overlying seal rock. Fluids will force through the seal, and continue migrating vertically through the strata until another seal is reached (England et al., 1987; Hindle, 1997; Thrasher, Fleet, Hay, Hovland, & Düppenbecker, 1996). Fluid migration through strata can permanently change rocks and damage the primary sedimentary layering (Løseth et al., 2009). Gas chimneys and pipes are examples of features with vertical fluid migration (Cathles, Su, & Chen, 2010; Judd & Hovland, 1992). The seismic identification and more details about chimneys and pipes will be presented in chapter 4.

2.4.1 Lateral migration

A direct result obtained when investigating the capillary pressure and Darcy's law, is that petroleum fluids will migrate through preferred migration pathways put up by well-connected large pores and pore throats. Carrier beds with sufficient porosities and permeabilities can thus act like transport ways for fluids (Bjørlykke, 2010). Deviation from pathways may occur because of lateral sealing barriers. Fluids will stay in porous carrier beds until they overcome the capillary pressure in pores in overlying seals (England et al., 1987; Hindle, 1997). A working seal has capillary pressures higher than the driving forces in the reservoir, and is able to trap hydrocarbons if the right trap geometry is encountered. This phenomenon is known as capillary sealing (England et al., 1987; Selley, 1998). Lateral fluid migration occurs in most sedimentary basins on Earth, but is prevalent in sedimentary basins that have undergone little tectonic activity (Thrasher et al., 1996).

2.4.3 Faults

Faults and fractures are structures formed by compressional or tensional forces in the Earth's crust. Both faults and fractures can be good fluid conduits through otherwise impermeable strata (Fossen & Gabrielsen, 2005; Ligtenberg, 2005). In many sedimentary basins around the world faults act as the main migration pathways (Ligtenberg, 2005; Løseth et al., 2009). Fault zones are complex systems of smaller faults and fractures. It is inferred that fluid migrates along local, weak sections within the fault zone and not across the entire fault (Ligtenberg, 2005). The migration depends greatly on the properties of the rocks in the fault zone. In the absence of clay-rich sediments, faults generally increase the effective permeability in a rock. Fractures in the fault zones often have lower capillary pressure than that of the pore throats in the original rock. If the faults in addition are held open by cements, fluid may flow freely (Judd & Hovland, 2007).

Fault systems belong to the largest of the three main groups of geological features characterized as seal bypass systems (SBS) by Cartwright et al. (2007). SBS encompasses large-scale, seismically resolvable geological structures that can breach sealing and allow fluids to flow either vertically or subvertically (Cartwright, Huuse, & Aplin, 2007).

2.4.4 Polygonal faults

Cartwright et al. (2003) define polygonal faults as:
"*an array of layer-bound extensional faults within a mainly fine-grained stratigraphic interval that exhibit a diverse range of fault strikes which partially or fully intersect to form a polygonal pattern in map view*".

Polygonal faults ca be both planar and listric. The vertical throw is usually in the range of 10-100m. The strikes of polygonal faults often have many orientations resulting in the characteristic pattern geometry (Figure 2.10A) (Cartwright, James, & Bolton, 2003; Lonergan, Cartwright, & Jolly, 1998).

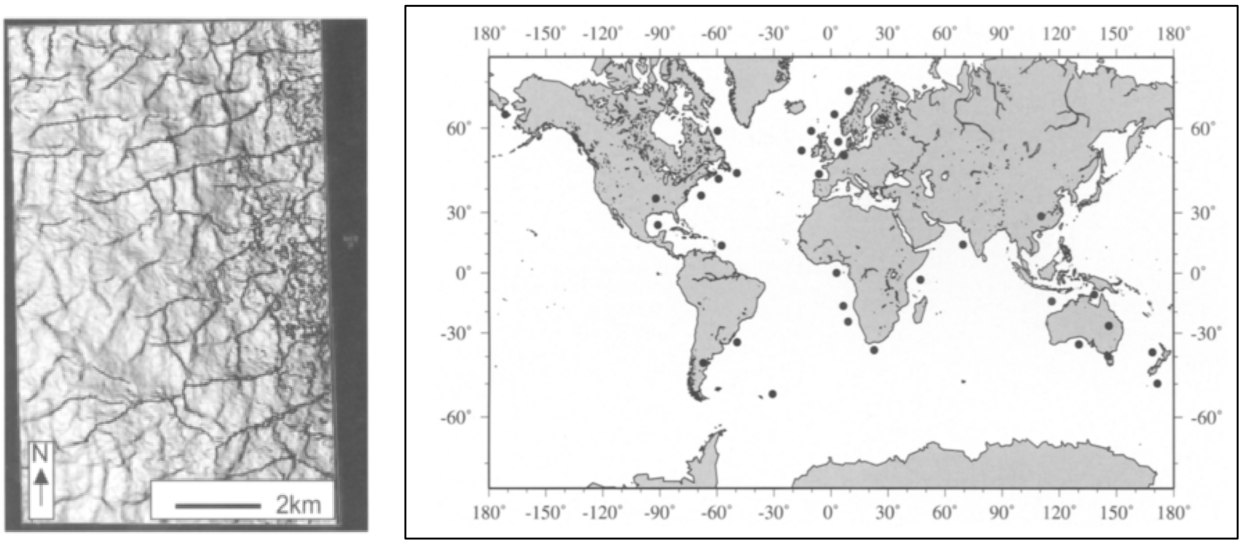

Figure 2.10: A) Map view of polygonal faults with a rectangular pattern. B) Black dots are marking the global distribution of polygonal faults recognized from seismic data and field evidence. Modified from Cartwright et al. (2003)

Polygonal faults are formed by processes such as gravity sliding/collapse, density inversion, syneresis and compactional loading. Cartwright et al. (2003) argued that syneresis is the most likely process in polygonal fault genesis. Syneresis is when a gel made of colloidal particles contracts spontaneously without the evaporation of a solvent. Clay particles have a high surface area to mass ratio and can potentially form gels that can synerese. As figure 2.10B shows, polygonal faults are found in many basins worldwide. However, they are most commonly located in passive margins or intra-cratonic settings (Cartwright et al., 2003; Dewhurst, Cartwright, & Lonergan, 1999).

2.4.6 Hydrothermal vents

As mentioned earlier, convection due to volcanism is one of the fluid flow mechanisms. When fluids come into contact with magma or hot volcanic rocks, hydrothermal systems are created. In contact with the magma, water gets heated and chemically altered. The hot water becomes buoyant and ascends towards the seabed (Jamtveit et al., 2004; Judd & Hovland, 2007). If this occurs in organic-rich sediments, large amounts of thermogenic gas can be transported upwards through the strata (Berndt, 2005).

2.4.7 Mud volcanoes and diapirism

Judd & Hovland (2007) proposed the term “mud volcano” for a topographically expressed geological feature on the seabed constructed mainly of mud which periodically or continuously vents liquid mud, including water, oil and gas.

A mud diapir differs from a mud volcano by not having any obvious venting. A diapir is a structure that has pierced or deformed younger sediments in an upward movement. Diapirism is not constricted to mud, but includes e.g. shale and salt piercement structures as well.

2.5 Gas hydrates

The second goal of this thesis is regarding gas hydrates and the mapping of a gas-hydrate related bottom-simulating reflector. This chapter aims to give the reader an overview over what gas hydrates are, how and where they form and what affects their stability.

2.5.1 Fundamental science of gas hydrates

Gas hydrates are ice-like crystalline compounds where gas molecules of low-molecular weight are enclosed by a framework of water molecules (Sloan, 1998). However, the term hydrate defines a general substance that is formed when water molecules are bound to other molecules. For the framework in which a guest molecule is enclosed within cavities in the crystal lattice of another, the term clathrate is used. The term clathrate comes from the Latin word “clathratus” which means “enclosed by bars or grating” (Kvenvolden, 1993, 1998; Max, 2003; Sloan, 1998; Sloan & Koh, 2007). The correct term would therefore be “gas clathrate hydrate”, but the more common term “gas hydrate” will be used in this thesis.

Gas hydrates include gases such as methane (CH_4), ethane (C_2H_6), propane (C_3H_8), butane (C_4H_{10}), iso-butane (C_4H_{10}), nitrogen (N_2), carbon dioxide (CO_2), hydrogen sulphide (H_2S) and hydrogen (H_2) (Kvenvolden, 1993; Sloan, 1998). The term “natural gas hydrate” firstly indicates naturally occurring gas hydrate. Secondly, it indicates that the hydrate contains natural gas, which includes all gases derived from natural chemical and biochemical processes. Natural gas hydrates are typically composed of methane accompanied by higher molecular weight hydrocarbon gases and non-hydrocarbon gases (Max, 2003).

Depending on the guest molecules, three different structural types I, II and H can be formed (Figure 2.11). The structure is referring to the framework of H_2O, and defines the internal space available for guest molecules. Structure I forms with small natural gas molecules smaller than propane, but molecules of similar size such as carbon dioxide and hydrogen sulphide may serve as guest molecules as well. Structure II forms with molecules greater than ethane but smaller than pentane. Structure H has gotten its name from the hexagonal framework, and can be formed with components from naphtha and gasoline or with smaller molecules like methane as well (Kvenvolden, 1993; Sloan, 1998; Sloan & Koh, 2007).

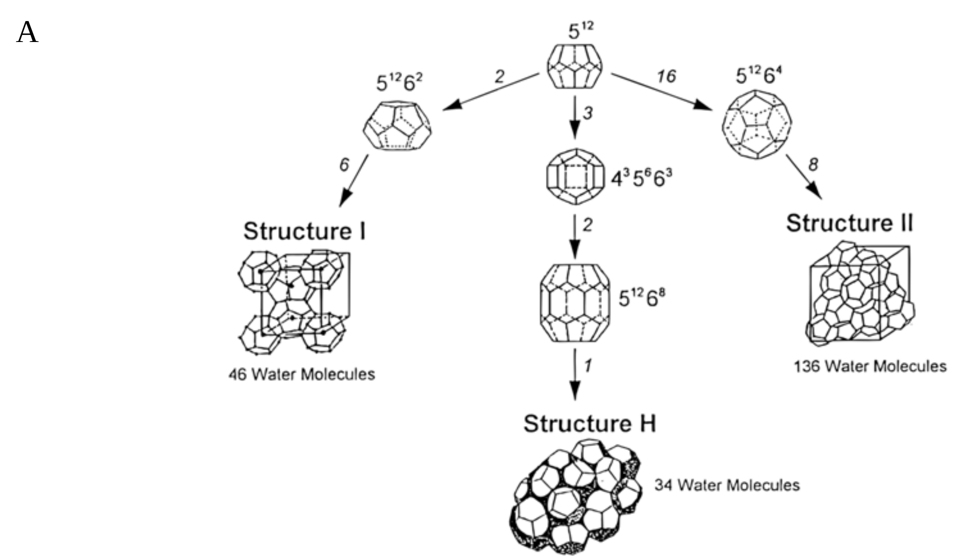

B

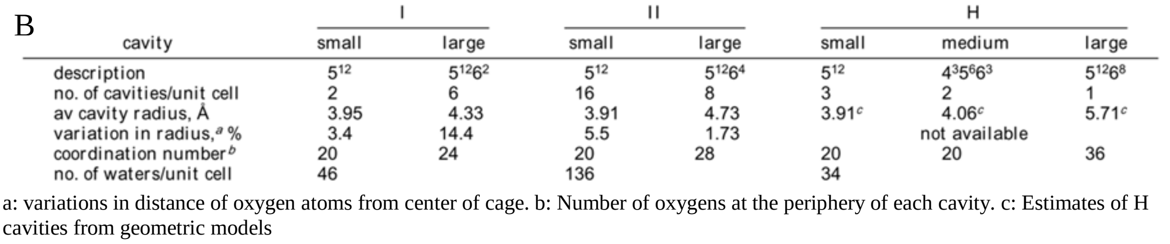

cavity	I small	I large	II small	II large	H small	H medium	H large
description	5^{12}	$5^{12}6^{2}$	5^{12}	$5^{12}6^{4}$	5^{12}	$4^{3}5^{6}6^{3}$	$5^{12}6^{8}$
no. of cavities/unit cell	2	6	16	8	3	2	1
av cavity radius, Å	3.95	4.33	3.91	4.73	3.91^{c}	4.06^{c}	5.71^{c}
variation in radius,^{a} %	3.4	14.4	5.5	1.73		not available	
coordination number^{b}	20	24	20	28	20	20	36
no. of waters/unit cell	46		136		34		

a: variations in distance of oxygen atoms from center of cage. b: Number of oxygens at the periphery of each cavity. c: Estimates of H cavities from geometric models

Figure 2.11: Diagram of different hydrate structures. A) The three different hydrate structures; Structure I, Structure II and Structure H. B) Summary of the geometry of cages in the three hydrate structures in A). From Sloan (1998).

2.5.2 Hydrate formation

Gas hydrates occur generally in two main type of settings. Both onshore and offshore permafrost settings in polar regions can contain hydrates. The second main type of setting where gas hydrates occur are deep oceanic settings (Kvenvolden, 1993, 1999). For distribution, see Figure 1.5. The pressure and temperature conditions at these settings allow hydrates to form. Gas hydrate formation is in addition determined by the presence of water, the supply of hydrate-forming gas, the presence of inhibitors (e.g. salt) and whether there is space for hydrate to grow in (host rock) (Kvenvolden, 1993, 1998; Senger, 2009; Sloan, Koh, & Sum, 2010).

With the right conditions, as outlined above, hydrates may form in the host rock as cement in pore spaces, as a layered structure, as nodules of pure hydrate or in a disseminated form within the pore space. Hydrates replacing pore fluids and completely filling pores will result in a reduced porosity and permeability in the host sediments. The capillary pressure will then resist fluids in migrating. This can trap free gas below the base of the hydrate (Chand & Minshull, 2003).

2.5.3 Hydrate stability

2.5.3.1 Phase equilibrium

After the formation of gas hydrate, the pressure (P)-temperature (T) conditions and gas composition determine when the hydrate will be stable or not. The P-T conditions can be illustrated using a phase equilibrium diagram (Sloan et al., 2010). Figure 2.12 shows the methane hydrate phase boundaries for permafrost (A) and marine settings (B). The zone in which the gas hydrate is stable is known as the gas hydrate stability zone (GHSZ). In both permafrost and marine settings, the geothermal gradient plays a major role in determining the extent of the GHSZ. For the marine case, the extent of the GSHZ is affected by the bottom-water temperature as well (Sloan et al., 2010). Typical values for hydrate formation in marine settings are bottom-water temperatures around 273K and with pressures >0.6 MPa (Sloan, 1998).

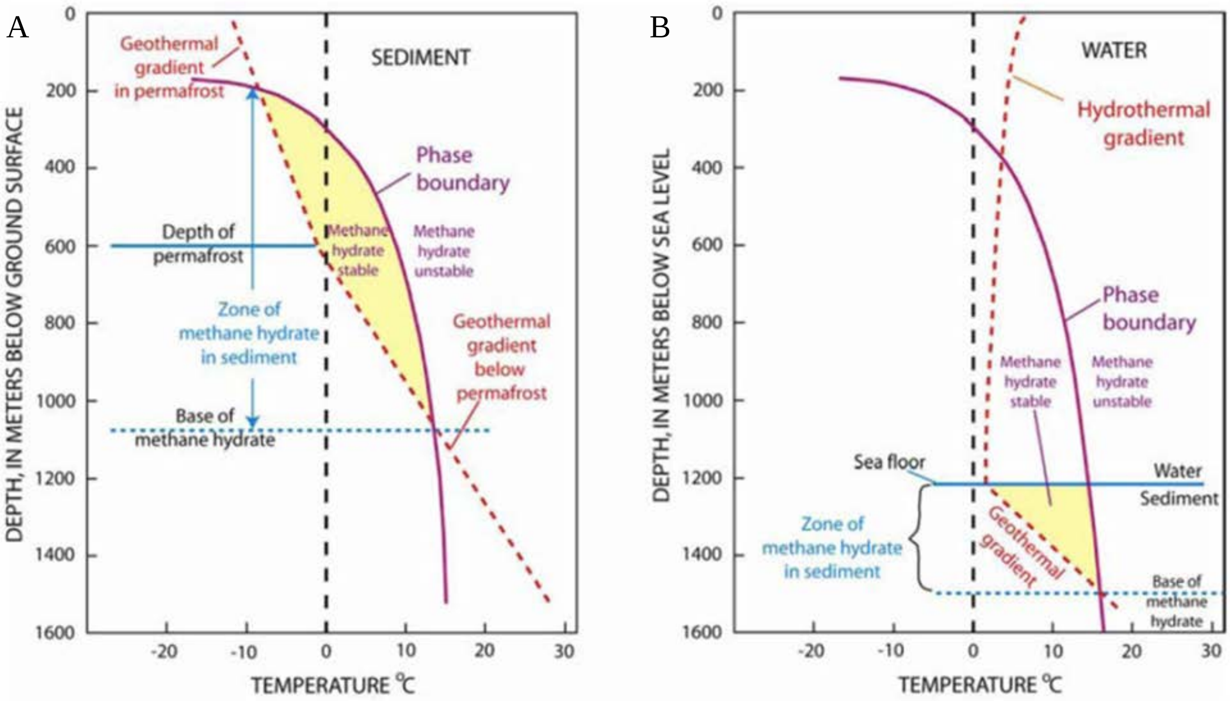

Figure 2.12: Phase equilibrium conditions for hydrate. A) Conditions in permafrost setting. B) Conditions in oceanic settings. The gas hydrate stability zone (GHSZ) is marked In yellow. From Sloan et al. 2010

2.5.3.2 Dissociation

Dissociation of hydrates can occur if there are changes in temperature and/or pressure. The temperature and pressure can be affected by a variety of processes, e.g. bottom-water variations, erosion, slumping/sliding, sedimentation, subsidence and uplift (Hornbach et al., 2001; Jung & Vogt, 2004; Max, 2003). Addition of inhibitors can also affect the stability (Sloan & Koh, 2007).

Not only the conditions in which the hydrate is present determines how stable it is. The properties of the hydrate itself also plays a role in how easily it dissociates when subject to temperature and pressure changes. The different hydrate structures (I, II and H) determine the type and concentration of gas within a volume of hydrate. This in turn determines the heat of dissociation (ΔH_d), defined as the enthalpy change (heat) required to dissociate the hydrate phase to free gas and liquid (water) (Sloan, 1998). The dissociation is thus determined greatly by the structure of the hydrate. Structure I dissociates at a lower temperature than structure II at a given pressure (Max, 2003).

2.6 Seismic reflection

The first seismic reflection survey was carried out by K. C. Karcher between 1919 and 1921 in Oklahoma, USA. Within 10 years, seismic reflection had become the dominant method for hydrocarbon exploration, as it is today. In addition to hydrocarbon exploration, seismic methods have a considerable number of other applications within geology, hydrology and environmental studies (Reynolds, 2011).

The basic technique of seismic exploration is to generate seismic waves and measure the time taken for the wave to travel from a source down into the subsurface where it is reflected back to the surface to be detected by a receiver (geophone or hydrophone). The time it takes from source to receiver is known as the two-way travel time (TWTT) or two-way time (TWT) (Reynolds, 2011; Sheriff & Geldart, 1995).

2.6.1 Seismic waves and elastic moduli

Seismic waves are elastic waves. How well the waves are transmitted depends on the elasticity of the medium. When an external force F from either an artificial source or an earthquake is applied to the Earth, the Earth's crust is subjected to stress. Stress (σ) is the ratio of a force to area. Stress can be divided into two components, one at right-angles to the surface (normal or dilatational stress) and one in the plane of the surface (shear stress (τ)) As a consequence of the stress, the material undergoes strain (ε), which means that the material's shape is distorted. The amount of deformation (strain) is expressed as the ratio of the change in length to the original length. Strain can also be given by the ratio of change in volume to the original volume. The stress and strain relationship for a materian is defined by various elastic moduli such as Young's modulus, bulk modulus, shear modulus and axial modulus (Reynolds, 2011; Sheriff & Geldart, 1995). Only bulk modulus and shear modulus will be shown here.

The bulk modulus is given as:

$$K = \frac{volume\ stress}{volume\ strain} = \frac{\Delta P}{\Delta V/V} \qquad \text{(Equation 8)}$$

The shear modulus is given as:

$$\mu = \frac{shear\ stress}{shear\ strain} = \frac{\tau}{\varepsilon} \qquad \textit{(Equation 9)}$$

There are three types of elastic waves that can be generated: Compressional waves (P-waves), shear waves (S-waves) and surface waves. In P-waves a particle in a material oscillates about a fixed point in the direction of wave propagation. The movement of the particle is determined by the compressional or dilatational strain. In S-waves a particle in the material moves at right angles to the direction in which the wave is propagating. This occurs by shear strain. The seismic velocity of a wave propagating through elastic media is determined by the elastic moduli and densities of the material (Reynolds, 2011; Sheriff & Geldart, 1995) and is given in m/s.

The velocity of P-waves is given as:

$$v_p = \sqrt{\frac{K + \frac{4}{3}\mu}{\rho}} \qquad \textit{(Equation 10)}$$

The velocity of S-waves is given as:

$$v_s = \sqrt{\mu/\rho} \qquad \textit{(Equation 11)}$$

Note that $\mu = 0$ for fluids, as fluids cannot support shear. This results in the velocity of S-waves being 0, $v_s = 0$. In both *Equation 10* and *Equation 11*, ρ is the effective bulk density of the rock. This density is determined by the rock’s matrix as well as the fluids included (Castagna, 1993). The density can be expressed by the following equation:

$$\rho = (1 - \varphi)\rho_{matrix} + \varphi\rho_{fluid} \qquad \textit{(Equation 12)}$$

Where ρ_{matrix} is the rock matrix(grain) density, ρ_{fluid} is the pore fluid density and φ is the porosity of the rock. The equation can be derived further by resolving the pore fluid density into two components: pore water and e.g. gas.

$$\rho = (1 - \varphi)\rho_{matrix} + \varphi(S_w\rho_w + S_g\rho_g) \qquad \textit{(Equation 13)}$$

Where S_w and ρ_w denote the saturation and density of pore water, respectively. ρ_g and S_g represent the saturation and density of the gas included within the pores (Castagna, 1993).

2.6.2 Seismic reflection theory

Seismic reflection is based on the presence and interpretation of impedance contrasts in the subsurface. An impedance contrast gives a seismic reflector. Seismic reflectors can be generated by lithology contrasts, faults, phase changes (solid-liquid-gas) or seismic artefacts (Veeken, 2007). Figure 2.13 illustrates a seismic wave propagating through medium 1 with density ρ_1 and velocity v_1. The wave then hits an interface between medium 1 and medium 2 where there are contrasts in density and/or velocity, i.e. an interface with a contrast in the acoustic impedance (Z). A part of the incident wave will then be reflected, and one part with continue through as a transmitted wave (Reynolds, 2011).

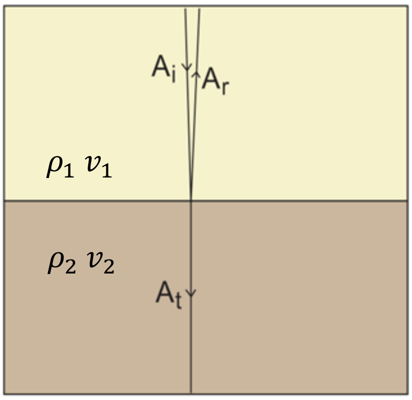

Figure 2.13: Reflection at the interface between two different rocks. A_i is the amplitude of the incident wave, A_r is the amplitude of the reflected wave and A_t is the amplitude of the transmitted wave. ρ is the density and v is the seismic velocity for the specific rock.

Acoustic impedance is the product of seismic velocity (v) at which the wave is propagating, and the density (ρ) of a layer, as follows:

$$Z = \rho \cdot v \qquad \textit{(Equation 14)}$$

The ratio of the amplitudes of the reflected (A_r) and incident (A_i) waves is known as the reflection coefficient (R) (*Equation 15*). Reflection coefficient gives a measure of the strength of a reflection generated at a subsurface interface. A positive reflection coefficient reflects an interface where the overlying medium (Z_1) has a lower acoustic impedance than the medium below (Z_2). If the overlying medium (Z_1) has a higher impedance contrast than the medium below (Z_2), a negative reflection coefficient will be produced (Reynolds, 2011; Selley, 1998; Sheriff & Geldart, 1995).

Reflection coefficient (R) at normal incidence is defined as:

$$R = \frac{A_r}{A_i} = \frac{(Z_2 - Z_1)}{(Z_2 + Z_1)} = \frac{(\rho_2 v_2 - \rho_1 v_1)}{(\rho_2 v_2 + \rho_1 v_1)} \qquad \textit{(Equation 15)}$$

In reality, the incident wave does not always come at right angles. For the situation where the incident wave hits the interface with a given angle, Snell's law (*Equation 16*) gives the relationship between the angles and velocities of the incident, reflected and transmitted waves (Figure 2.14)(Veeken & Moerkerken, 2013).

Snell's law is defined as:

$$\frac{\sin \theta_{ind}}{v_1} = \frac{\sin \theta_{trans}}{v_2} = \frac{\sin \theta_{refl}}{v_1} \qquad \textit{(Equation 16)}$$

Where θ_{ind} is the angle formed by the incident wavefront, θ_{trans} is the angle of the transmitted wave in the second medium (2), θ_{refl} is the angle of the reflected wave, v_1 and v_2 are the propagation velocities in medium 1 and 2, respectively.

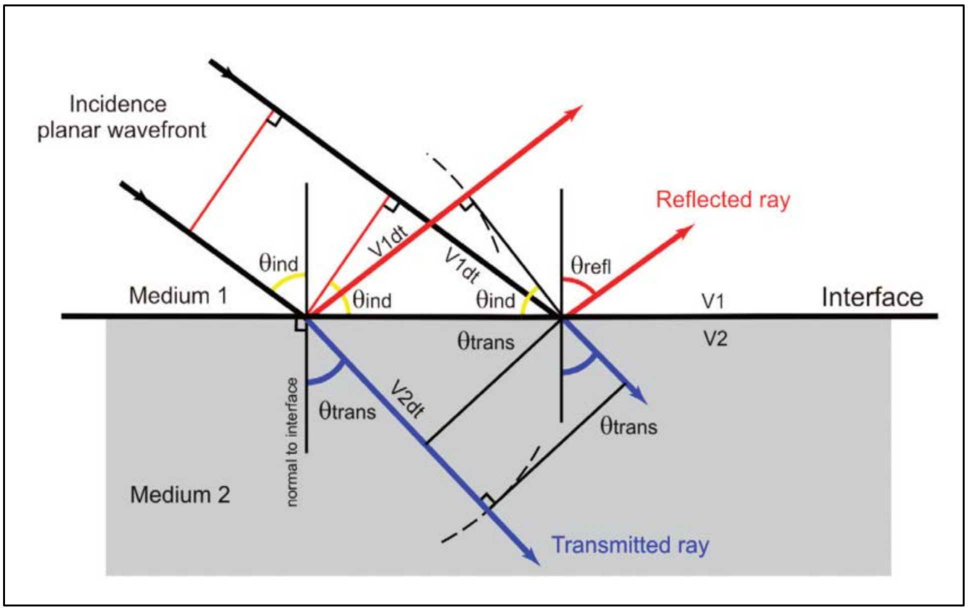

Figure 2.14: Seismic waves propagating across an interface with an acoustic impedance contrast. Some of the energy from the incident wave gets reflected back into medium 1 and some of the energy gets transmitted into medium 2. From Veeken & Moerkerken (2013).

2.7 Seismic response

As discussed in the previous sections, a seismic reflector is set up by an impedance contrast. A common way to describe reflections is to use polarity. There are different polarity conventions, but this paper will follow the SEG (Society of Exploration Geophysicists) standard (Sheriff, 2006). For a normal polarity zero-phase wavelet, an increase in acoustic impedance (positive reflection coefficient) is represented by a central peak. For a minimum-phase wavelet, a reflection indicating an increase in acoustic impedance begins with a trough, a downward deflection. For a reverse polarity wavelet, the representations will be the opposite (Figure 2.15) (Sheriff, 2006).

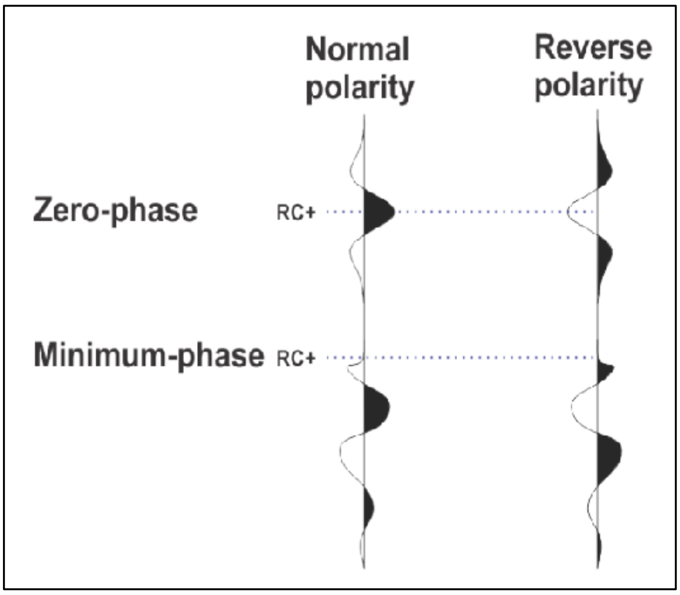

Figure 2.15: SEG (Society of Exploration Geophysicists) polarity convention used in this study. From Sheriff (2006).

The following sections will look at the seismic response of e.g. gas hydrates, hydrocarbons and sills.

2.7.1 Bottom-simulating reflectors (BSR)

Bottom-simulating reflectors (BSR) often lie at a constant depth beneath the seabed and mimics the seabed topography. Another characteristic of the BSR is that it represents an abrupt change in acoustic impedance. When stratigraphic horizons do not lie parallel to the seabed, the BSR is crosscutting (Bünz & Mienert, 2004; Judd & Hovland, 2007). BSR can be caused by the presence of gas hydrates or by diagenesis (Berndt, Bünz, Clayton, Mienert, & Saunders, 2004).

2.7.1.1 Gas hydrate-related BSR

Gas-hydrate related BSR is caused by the impedance contrast between the overlying gas hydrates and the underlying free gas and gas-saturated sediments (Bünz & Mienert, 2004; Haacke, Westbrook, & Hyndman, 2007; MacKay, Jarrard, Westbrook, & Hyndman, 1994). The reflection often has a reversed polarity (negative phase) compared to the seabed (Bünz & Mienert, 2004; Judd & Hovland, 2007). The BSR often corresponds to the base of the gas hydrate stability zone (BGHSZ). Below the GHSZ the gas hydrates become unstable and start to dissociate (Berndt et al., 2004; Judd & Hovland, 2007). Free gas may accumulate below the GHSZ giving a reduction in velocity directly under the BSR (Figure 2.16). The presence of gas often results in enhanced reflections. The amplitude anomaly associated with gas-hydrate related BSR is due to the presence of free gas beneath the GHSZ, not the gas hydrate itself (Bünz & Mienert, 2004; Chand & Minshull, 2003; Haacke et al., 2007). Figure 2.17 shows an example of a gas-hydrate related BSR that coincides with the expected depth of the BGHSZ (Berndt et al., 2004).

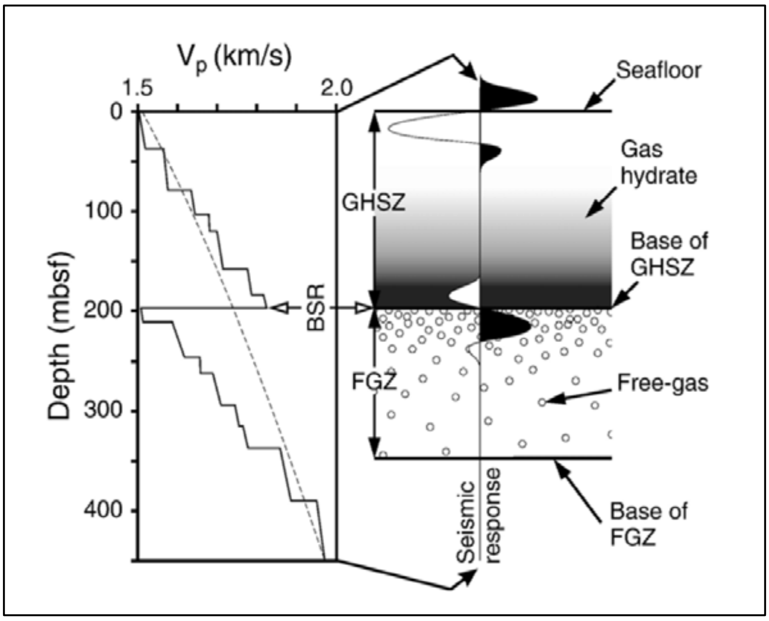

Figure 2.16: Illustration of a section of gas hydrate and underlying free gas. The BSR marks the base of the gas hydrate stability zone (BGHSZ). Note the reversed polarity of the BSR. From Haacke et al. (2007).

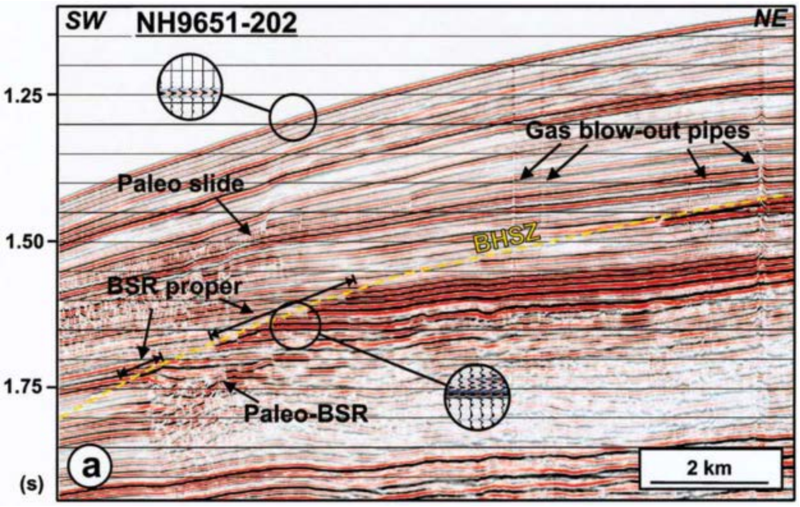

Figure 2.17: Gas-hydrate related BSR from the southern Vøring Plateau. Note how the BSR is crosscutting the stratigraphic horizons and has a reversed polarity. Modified from Berndt et al. (2004).

As mentioned in chapter 2.5, the stability and thus the GHSZ are determined by temperature and pressure. The conditions can be affected by e.g. bottom-water variations, erosion, slumping/sliding, sedimentation, subsidence and uplift. If the conditions change, the BGHSZ may shift either up or down. Figure 2.18 shows how the depth of the BSR can change as a result of erosion. This leaves a paleo-BSR reflection.

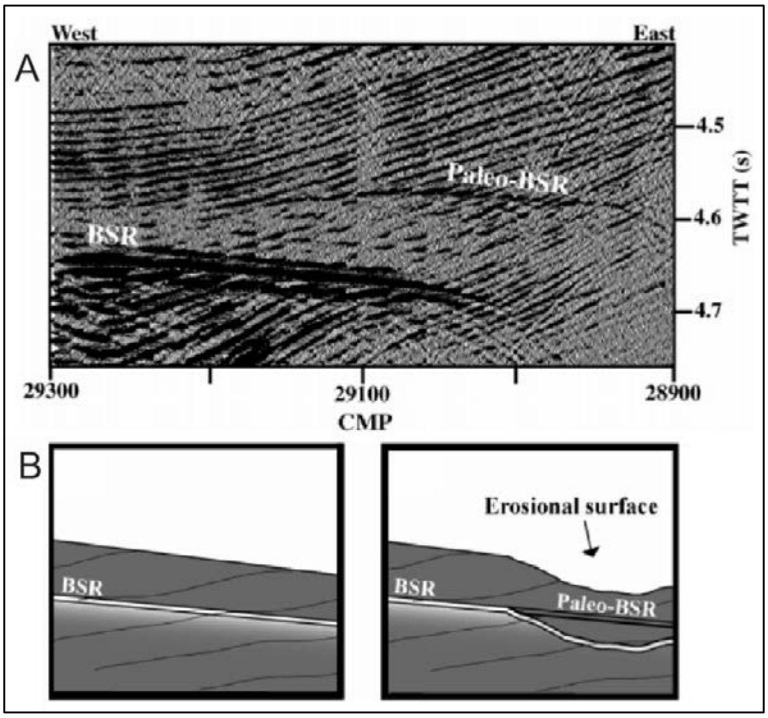

Figure 2.18: A) Seismic section in variable wiggle showing a Paleo-BSR and a present-day BSR. B) Illustration showing how the BGHSZ may shift to a deeper level due to erosion. This results in the BSR forming at a deeper level as well, leaving a Paleo-BSR. Modified from Hornbach et al. (2003).

The BSR does always crosscut the stratigraphic horizons at such a high angle as Figure 2.17 shows. An example of a BSR occurring in Lake Baikal (Siberia) shows how high-amplitude reflections can terminate at the base of the gas hydrate stability zone at small angles (Figure 2.19). This can also occur in marine settings where the seafloor is relatively levelled.

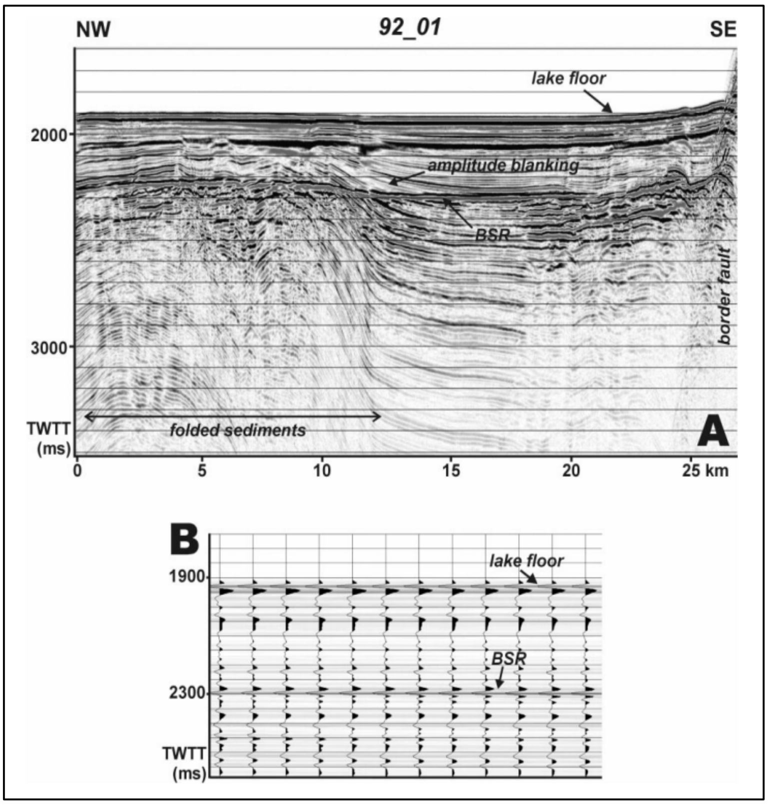

Figure 2.19: A) Illustration of the seismic characteristics of a BSR formed in lake sediments with small dip angles. B) Illustration of how the BSR reflection has a reversed polarity compared to the lake floor. From Vanneste et al. (2001).

2 7.1.2 Diagenesis-related BSR

Bottom-simulating reflectors can be caused by the diagenesis of siliceous-rich sediments with the transformation of Opal A to Opal C/T, Opal C/T to quartz or smectite to illite. The depth of the given diagenetic transformation depends on the temperature and pressure. The Opal A to Opal C/T BSR occurs at a lower temperature (shallower) than the BSR resulting from Opal C/T to quarts transformation. As opposed to the gas hydrate-related BSR, the diagenesis-related BSR (DBSR) has the same polarity as the seafloor reflection. Figure 2.20 shows a seismic section containing two BSRs at different depths. These BSRs are believed to result from different diagenetic transformations, determined by the pressure-temperature conditions (Berndt et al., 2004).

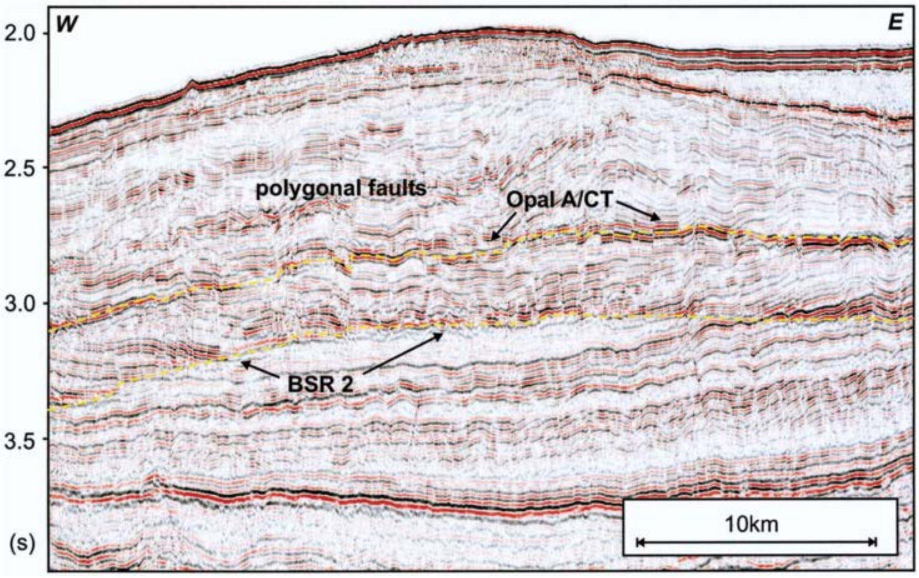

Figure 2.20: Diagenesis-related BSR. From Berndt et al. (2004).

Another example of a seismic section containing multiple diagenetic BSRs at different depths, is shown in Figure 2.21. Since the diagenetic BSR is dependent on pressure and temperature conditions, if often appears to have a roughly constant depth. However, DBSRs do not mimic the seafloor as closely as gas hydrate-related BSRs tend to do (Chand et al., 2011).

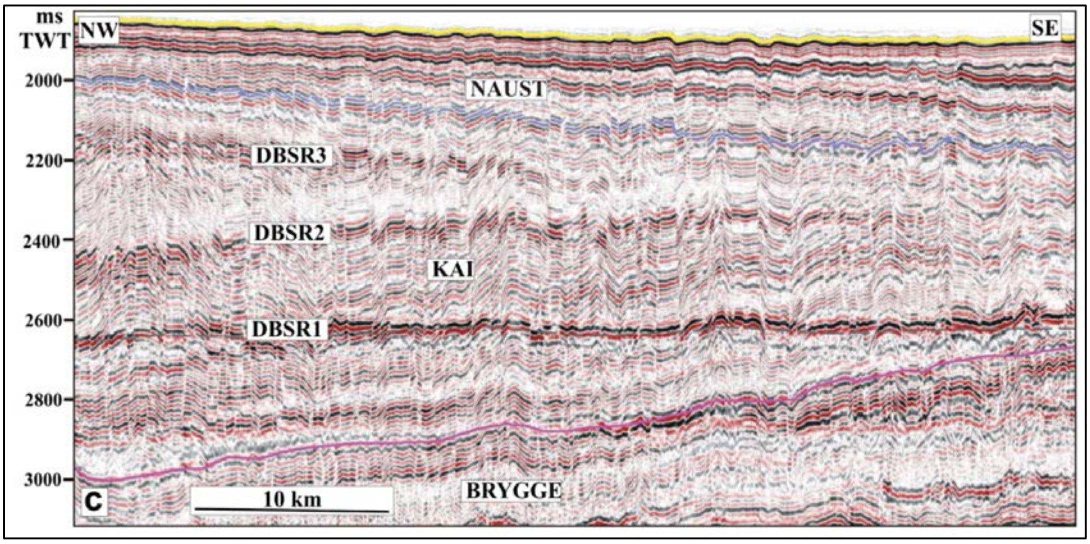

Figure 2.21: Seismic section showing three DBSRs observed in the Vøring Basin. From Chand et al. (2011).

2.7.2 Seismic indications of hydrocarbons

Hydrocarbons can be recognized in seismic data in various ways. Accumulation of hydrocarbons can often give high amplitude anomalies. These amplitude anomalies are known as hydrocarbon indicators and can be either of positive or negative amplitudes. Amplitude anomalies can be divided into bright spots and dim spots. Other hydrocarbon indicators are flat spots, velocity effects, polarity/phase reversal and other effects such as loss of frequencies (Andreassen, Nilssen, & Ødegaard, 2007; Løseth et al., 2009).

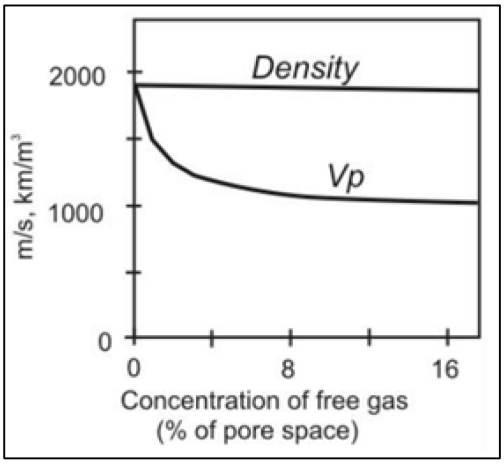

Figure 2.22: Illustration of how free gas in pore spaces affects P-wave velocity ($v_{P,}$ in ms/s) and density (in kg/m^3). The graphs are given as a function of gas saturation for sediments with porosity 0.4 and v_p = 1900 m/s. From Andreassen et al. (2007).

If gas is present in the pore spaces, there will be a reduction in the p-wave velocity (v_P) as shown in figure 2.22. If the concentration of free gas is high enough, an acoustic impedance contrast with a negative reflection coefficient will occur at the top of the gas bearing sediment (Figure 2.23 and Figure 2.24). On the seismic section this will be shown as a bright spot. The higher the gas saturation, the higher the acoustic impedance contrast will be, giving a brighter amplitude anomaly. The gas-water contact will appear as a flat reflection, known as a flat spot (Figure 2.23 and Figure 2.24).

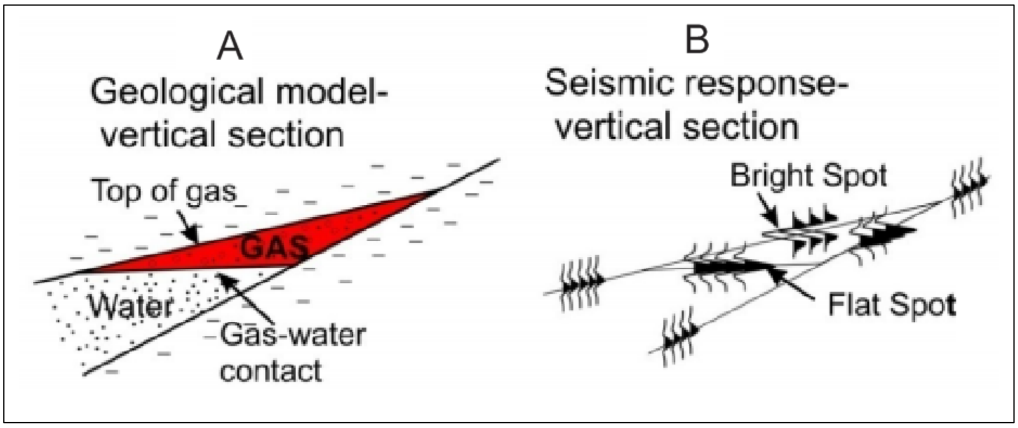

Figure 2.23: A) Geological model of a gas bearing sand. B) Seismic response of the gas wedge in A. Note how the top of the gas gives a bright spot and the gas-water contact gives a flat spot with reversed polarity. Modified from Andreassen et al. (2007)

The flat spot occurs because of the density differences between water and gas (Andreassen et al., 2007; Løseth et al., 2009).

In Figure 2.24 dim spot and phase reversal can be seen in addition to bright and flat spots. A dim spot is a local decrease in negative of positive amplitude strength. A phase reversal is a phase shift along a continuous reflection, so that a peak becomes a trough and the opposite (Løseth et al., 2009). Other indications for the presence of gas in particular, are phenomena like push-down, acoustic turbidity/chaotic reflections, acoustic masking/blanking. Acoustic turbidity relates to a chaotic reflection pattern compared to surrounding areas. It is often a result due to scattering of acoustic wave-energy. Acoustic blanking or acoustic masking is when there is a faint in reflections. In some cases the reflections might be blanked out (absent). Acoustic masking can occur due to the absorption of acoustic energy by overlying gas-charged sediments, but can also be caused from interstitial gas bubbles in the sediment (Andreassen et al., 2007; Løseth et al., 2009) . A push-down (also called pull-down) is an apparent down-bending due to an overlying low-velocity region, typically gas. The opposite is a pull-up which occurs due to a shallower high-velocity region (Løseth et al., 2009). Figure 2.25 shows several of the hydrocarbon indicators discussed above, e.g. bright spots, pull-down and acoustic masking.

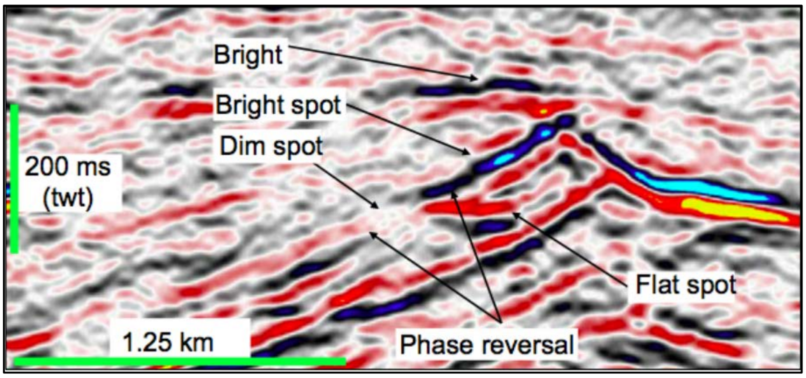

Figure 2.24: Seismic section with bright spot, dim spot, flat spot and phase reversal indication the presence of hydrocarbons. From Løseth et al. (2009).

2.7.3 Seismic indications of fluid flow

This section concerns the seismic response of fluid flow or fluid migration.

2.7.3.1 Chimneys and pipes

Acoustic masking can be an indication for gas bubbles present in sediment, but it is also an indication for fluid migration (Figure 2.25). Vertical or subvertical zones of acoustic masking may represent high fluid-flux paths. Such vertical zones of acoustic masking are commonly referred to as seismic chimneys (Andreassen et al., 2007; Heggland, 1997, 1998; Løseth et al., 2009). The shape of chimneys vary from diffuse shadows with chaotic reflections, funnels to distinct cigars or obelixes (Løseth et al., 2009).

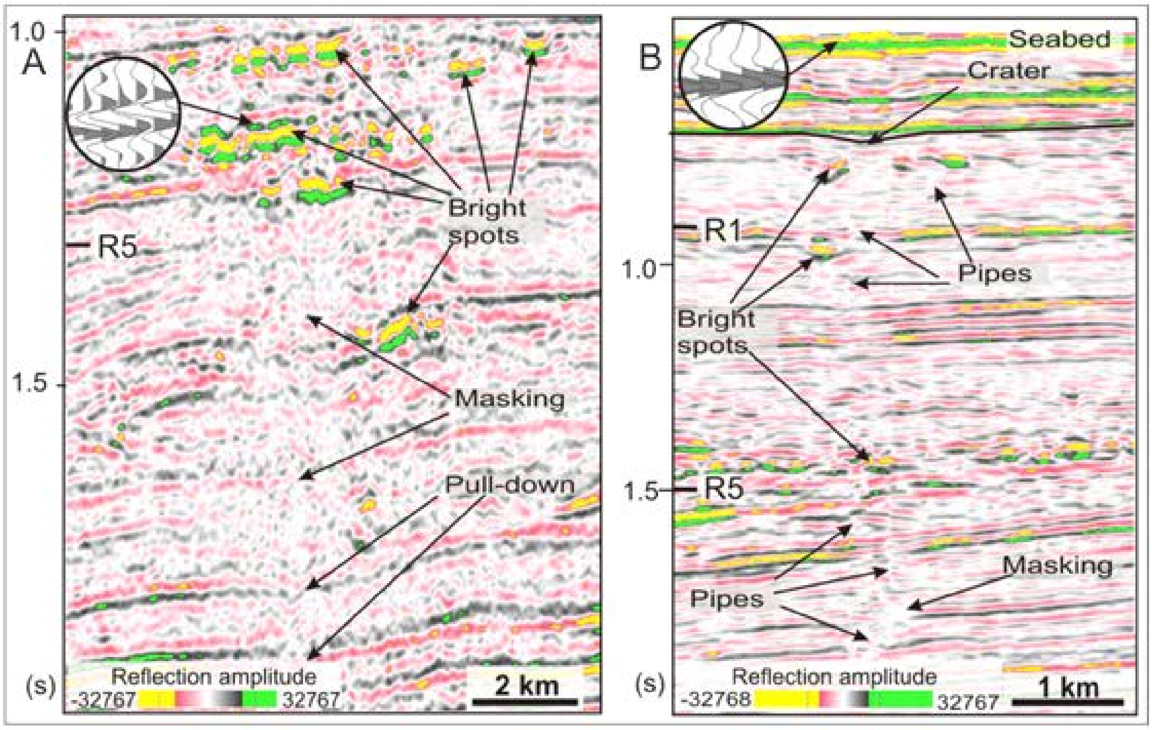

Figure 2.25: A) Seismic section showing a zone of acoustic masking with associated bright spots and pull-down (push-down). B) Seismic profile with acoustic pipes, including acoustic masking and bright spots. Modified from Andreassen et al. (2007).

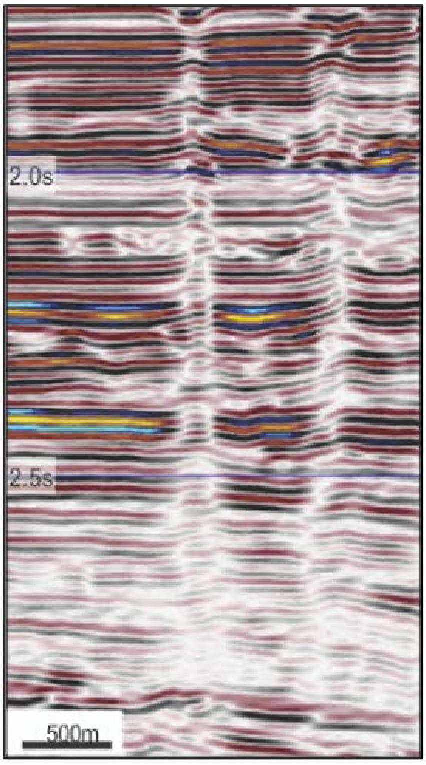

Figure 2.26: Seismic section showing acoustic pipe anomalies. Modified from Løseth et al. (2011).

An acoustic pipe is a special case of chimneys. Pipes occur as narrow vertical to near vertical columnar disturbances (Figure 2.26). Usually the reflections are disrupted over a long vertical extent. In map view pipes occur as circular to oval features 20-200m across (Berndt, Bünz, & Mienert, 2003; Løseth et al., 2011). Pipes are often interpreted as violent (fast flowing), episodic blowout structures (Løseth et al., 2009; Løseth et al., 2011). Pipes are one of the main groups of seal bypass systems, as described by Cartwright et al. (2007). Pipe bypass systems are divided into four families: dissolution pipes, hydrothermal pipes, blowout pipes and seepage pipes (Cartwright et al., 2007).

Dissolution pipes form as rocks dissolve at depth and create subsurface cavities. This can lead to instability in the overburden, which in turn can lead to the overburden collapsing. The formation rate is controlled by the rate of solution which can be gradual or rapid. Such pipes often occur in areas with evaporite and carbonate karst. Evaporites can make up high-quality seals, but can be breached by dissolution pipes and fluids can then migrate up through the overburden (Cartwright et al., 2007).

Hydrothermal pipes (vents) are related to high-flux fluid migration resulting from fluids coming into contact with igneous rock (Figure 2.27). The formation of hydrothermal vents is considered to be catastrophic with high-velocity focused fluid flow. On seismic data, hydrothermal pipes can be recognized by columnar disturbances with inward-dipping sedimentary strata and conical or crater-like terminations. Hydrothermal vents or pipes are typically developed directly above high-amplitude sill intrusions (Cartwright et al., 2007; Jamtveit et al., 2004; Planke, Rasmussen, Rey, & Myklebust, 2005).

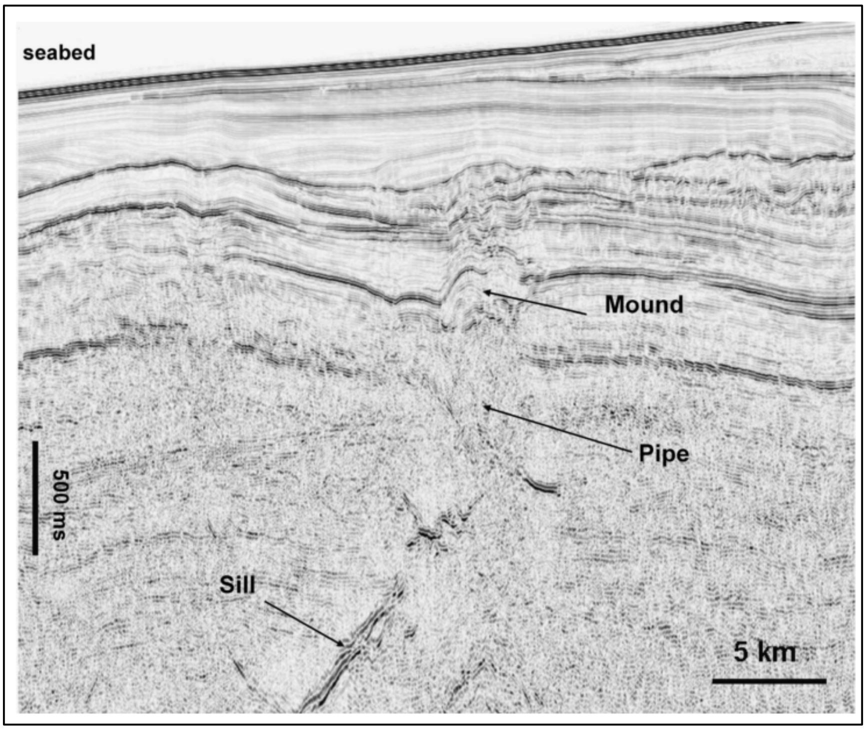

Figure 2.27: Seismic section showing a hydrotherm avent and underlying pipe. Note the igneous sill just below the pipe. From Cartwright et al. (2007)

Blowout pipes show the characteristics as outlined above, they occur as columnar disturbances with craters at the upper pipe termination. They can be distinguished from dissolution and hydrothermal pipes by their context. Blowout pipes are not found in relation to karstified units or in contact with sill intrusions. Instead, blowout pipes can be found in association with underlying overpressured intervals (Cartwright et al., 2007).

The seismic expression of seepage pipes resemble blowout pipes, but lack the blowout crates caused from violent outburst of fluid. Seepage pipes occur above accumulations of gas, such as gas reservoirs and structural crest in sand or silt-dominated sediments. The host rock in which seepage pipes occur is another way to differentiate them from blowout pipes, since the blowout pipes tend to occur in fine-grained sealing sequences (Cartwright et al., 2007).

2.7.3.2 Faults

The next and largest group of seal bypass systems are fault related systems. Faults have been discussed in section 2.4, thus only their seismic expression will be included here. Faults that are seismically resolvable often have throws greater than 10m. Faults can cross hundreds of metres of stratigraphic section, and therefore have great potential for long-range vertical fluid transmission. Faults can be divided into two main families: trap-defining and supratrap.

The first family includes faults that define and delimit a trap by laterally sealing it. The second includes faults that are embedded within the sealing sequence and lead fluids through the seal (Cartwright et al., 2007). Because fault zones have an uneven distribution and limited extent, migration along faults can be difficult to identify. If hydrocarbons migrate into permeable strata to the sides of the fault it can give hydrocarbon indicators such as bright spots, indicating that migration along the fault has occurred (Figure 2.28)(Løseth et al., 2009; Vadakkepuliyambatta, Bünz, Mienert, & Chand, 2013). Faults can have had periods where it acts as a seal and other periods where it is leaking (Cartwright et al., 2007; Løseth et al., 2009).

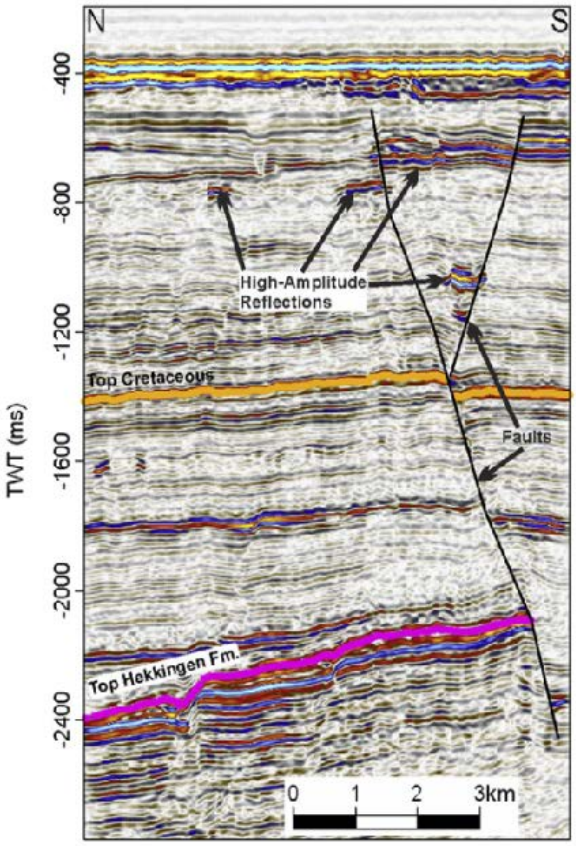

Figure 2.28: Fluid leakage along faults found in the Barents Sea. Note the high-amplitude anomalies to the sides of the faults. Modified from Vadakkepuliyambatta et al. (2013).

Polygonal faults belong to the supratrap family of fault bypass systems. Polygonal faults are common in fine-grained sediments (Cartwright et al., 2007). As mentioned, they show a polygonal pattern in plane view. The seismic expression of polygonal faults is characterised by discontinues reflections (Figure 2.29). Polygonal faults can be both planar and listric (Cartwright et al., 2003; Lonergan et al., 1998).

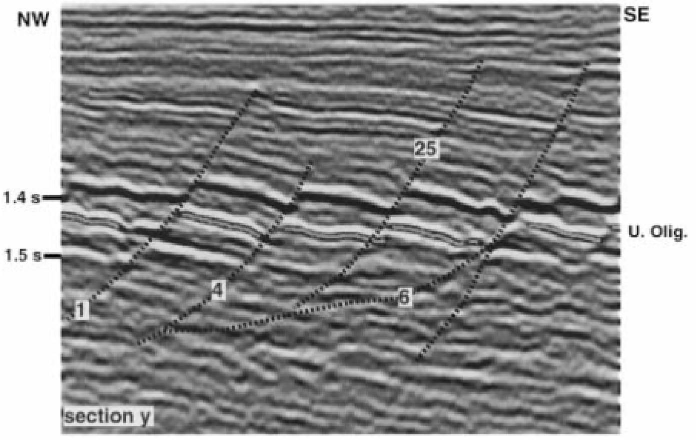

Figure 2.29: Seismic section showing polygonal faults. From Lonergan et al. (1998).

2.7.3.3 Intrusions

The last of the main groups of seal bypass systems, are intrusions. Intrusions can breach the seal in three different ways. The first way is when the intrusive event itself punctures the seal and allows fluids along with the intrusive material to transmit through the seal. Mud volcanoes are intrusive features that expel mud including fluids (water, oil and gas). The second, when the intruded material has higher permeability than the adjacent seal, e.g. when sandstone intrudes a shale. This allows fluids to flow through the intrusion. The third and last way intrusions act as seal bypass systems is when the intrusion process fractures and deforms the sealing sequence in such a way that fluid can flow through the areas with increased permeability. An example of an intrusion that can fold and fracture seals is a salt diapir. Diapirism often is episodic, thus the associated fluid flow is believed to be episodic as well (Cartwright et al., 2007)

2.7.3.4 Seabed expression of fluid flow

If the fluid migration paths terminate at the seafloor, they can create pockmarks, which are seabed expressions of fluid flow. Pockmarks are depressions in the seabed created from fluid discharge. They are often found in areas where gas is present in near-surface sediments and above zones with acoustic masking (pipes or chimneys) Pockmarks can be a few metres to tens of metres deep. The diameter can vary from 5m to several hundred of metres, but is typically several tens of metres. If the pockmark is 1 to 10m across and 0.5 m deep, it is defined as a unit pockmark. The shape of a pockmark can be circular, elliptical or composite when individual pockmarks merge into other pockmarks (Hovland, Gardner, & Judd, 2002; Judd & Hovland, 2007; Løseth et al., 2009). Figure 2.30 shows two normal pockmarks and associated strings of smaller pockmarks. Mud volcanoes also belong to seabed fluid flow features (Judd & Hovland, 2007).

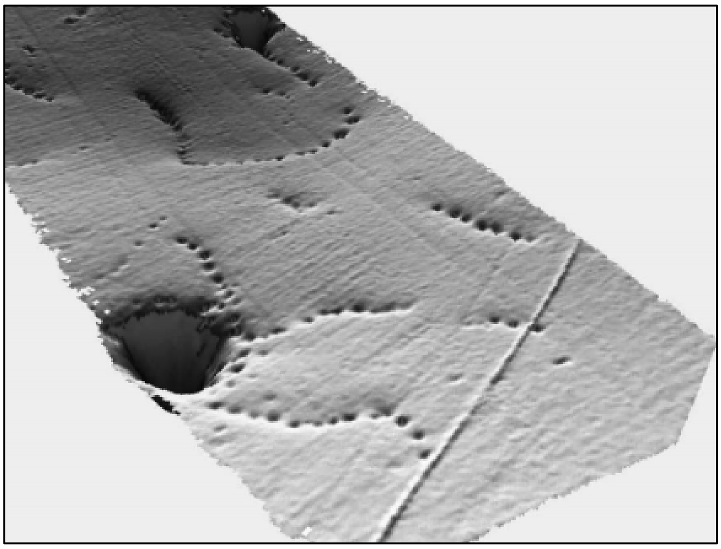

Figure 2.30: Perspective view of the seabed including pockmarks and strings of smaller (unit) pockmarks. The linear feature is a gas pipeline. From Hovland et al. (2002)

3 Study area

This thesis investigates fluid flow and gas hydrates within the outer Vøring Basin off mid-Norway. Vøring Basin is found in the Norwegian Sea which represents a passive continental margin stretching from 62 to 69°30'N (Blystad et al., 1995). The location of the study can be seen in Figure 3.1. The figure includes the main structural elements.

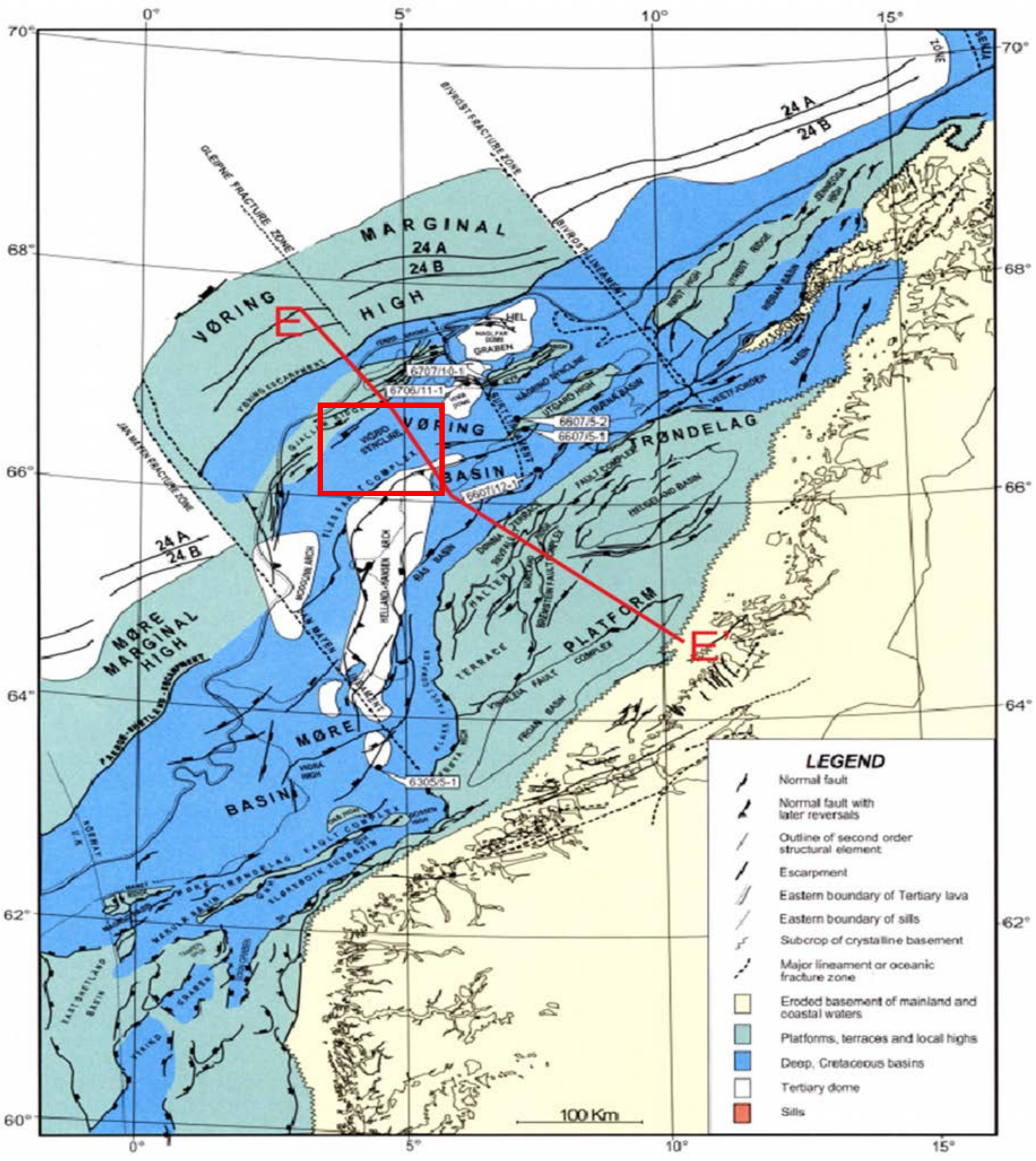

Figure 3.1: Structural map showing basins, highs, platforms, domes, faults and fault zones on the mid-Norwegian continental margin. Form Brekke (2000). The study site (marked with a red rectangle) is located in the Vigrid Syncline in Vøring Basin.

3.1 Tectonic setting

The tectonic history of the Norwegian Sea can be divided into three main epochs.
During the pre-Late Devonian epoch the region was under compressional stress. This epoch ended with the Caledonian Orogeny in Late Silurian and Early Devonian time, which lead to the final closure of the Iapetus Ocean. The stress regime changed from compressional to extensional, which marks the onset of the second major epoch lasting from Late Devonian to Paleocene. This epoch consisted of episodic extensional deformation and rifting that lead to the continental separation between Eurasia and Greenland at the Paleocene-Eocene transition. The last epoch spans from Early Eocene to present and is a period with active seafloor spreading in the Norwegian-Greenland Sea (Blystad et al., 1995; Brekke, 2000; Hjelstuen, Eldholm, & Skogseid, 1997; Ottesen, Rise, Andersen, & Bugge, 2009). The main epochs can be subdivided into several phases resulting in the formation of different structural elements found in the Norwegian Sea.

As can be seen in Figure 3.1, two major basins dominate the Norwegian Sea continental margin: The Vøring and Møre Basins. These basins were developed by Late-Jurassic to Cretaceous rifting. This was then followed by a regional subsidence in Cretaceous time resulting in the formation of these two deep basins. The Vøring and Møre Basins are separated by the Jan Mayen Lineament. The basins are bound to the west by Møre and Vøring Marginal Highs which were formed during the Paleocene-Eocene breakup mentioned above. The marginal highs are characterized by Early Eocene basalt flows. The magmatic event resulted in sill intrusions in the Vøring and Møre Basins. The sills were emplaced in Cretaceous sediments. Vøring Escarpment marks the boundary between Vøring Basin and Vøring Marginal High. To the north, Vøring Basin is bound by the Bivrost Lineament. To the east, the basin is bound by the uplifted Trøndelag Platform. Between Late-Eocene and Mid-Miocene, the mid-Norwegian margin went through several compression phases resulting in N-S trending dome structures. The past 3 My however, have been dominated by glacial deposition. Uplift of the Norwegian mainland provided additional sediment supply form the east which resulted in extensive deposition of glacigenic sediments (Blystad et al., 1995; Brekke, 2000; Hjelstuen et al., 1997; Hjelstuen, Sejrup, Haflidason, Berg, & Bryn, 2004). A regional profile EE’ is shown in Figure 3.2. The figure shows sub-elements of the Vøring Basin and Trøndelag Platform, such as Fenris Graben, Gjallar Ridge, Vigrid Syncline, Helland Hansen Arch and Fles Fault Complex.

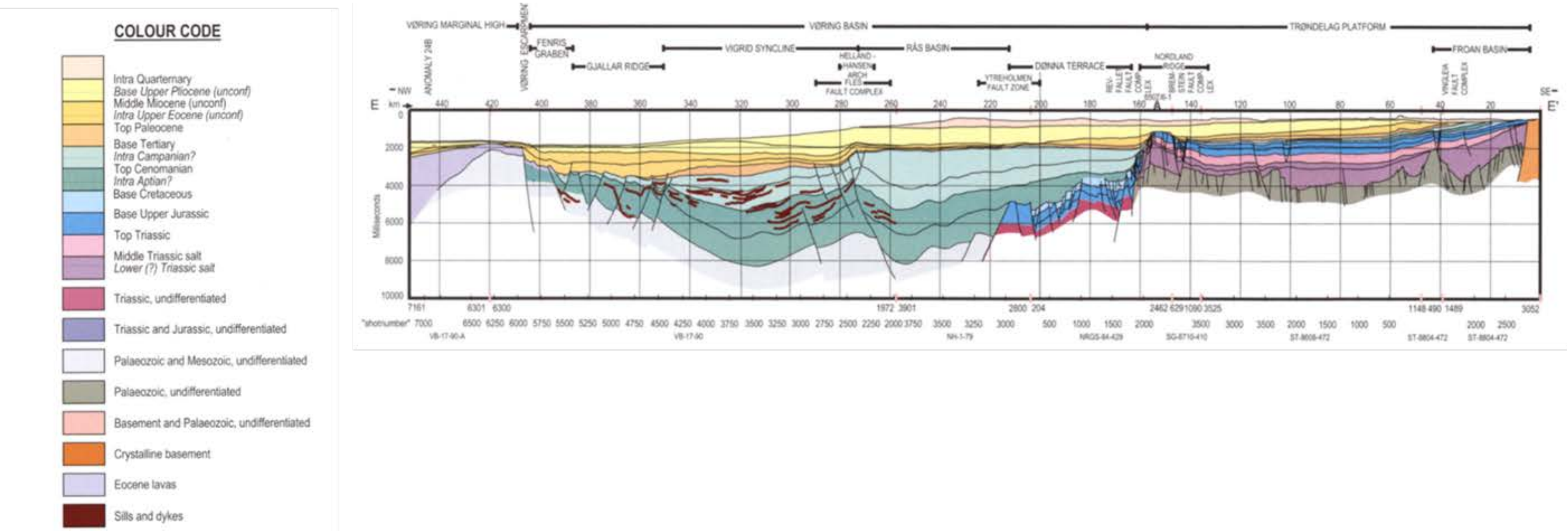

Figure 3.2: Regional profile across the mid-Norwegian continental margin. Note the sills emplaced in the Cretaceous sediments. From Brekke (2000).

3.2 Summary of previous work from the region

As mentioned, the sedimentary rocks in the Vøring and Møre Basins were intruded by sills during Paleocene-Eocene (Raum et al., 2006). These sill intrusions have had a significant impact on deformation, source-rock maturity and fluid flow. Hydrothermal vents associated with intrusive complexes have been mapped in both Møre and Vøring Basins (Dumke et al., 2014; Planke et al., 2005). Mud volcanoes and mud diapirs have been studied particularly at Gjallar Ridge. These are also interpreted in relation to the sill intrusions (Hansen, Cartwright, Huuse, & Clausen, 2005). The distribution of other fluid flow features e.g. chimneys and pipes have been studied together with associated pockmarks (Chand et al., 2011; Dumke et al., 2014; Hansen et al., 2005; Hjelstuen, Haflidason, Sejrup, & Nygård, 2010; Plaza-Faverola, Bünz, & Mienert, 2010, 2011; Westbrook et al., 2008). Polygonal faults are often linked with fluid flow and have also been mapped in Vøring Basin (Berndt et al., 2003; Hjelstuen et al., 1997; Hjelstuen et al., 2010; Hustoft, Mienert, Bünz, & Nouzé, 2007). Gas hydrates in the area are inferred through seismic detection of gas-hydrate related bottom-simulating reflector (BSR) (Andreassen, Mienert, Bryn, & Singh, 2000; Bouriak, Vanneste, & Saoutkine, 2000; Bünz, Mienert, & Berndt, 2003; Plaza-Faverola, Bünz, & Mienert, 2012). Hydrates have also successfully been recovered (Ivanov et al., 2007). In addition to the mentioned features, the area is also characterised by slide events. The largest slides in the region have been studied extensively e.g Storegga, Sklinnadjupet and Trænadjupet slides (Bryn, Berg, Forsberg, et al., 2005; Bryn, Berg, Lien, et al., 2005; Bugge, Belderson, & Kenyon, 1988; Haflidason, Lien, Sejrup, Forsberg, & Bryn, 2005; Rise et al., 2006). The location of the study area relative to some of the mentioned work, is shown in Figure 3.3. Note particularly the outline of polygonal faults and BSR.

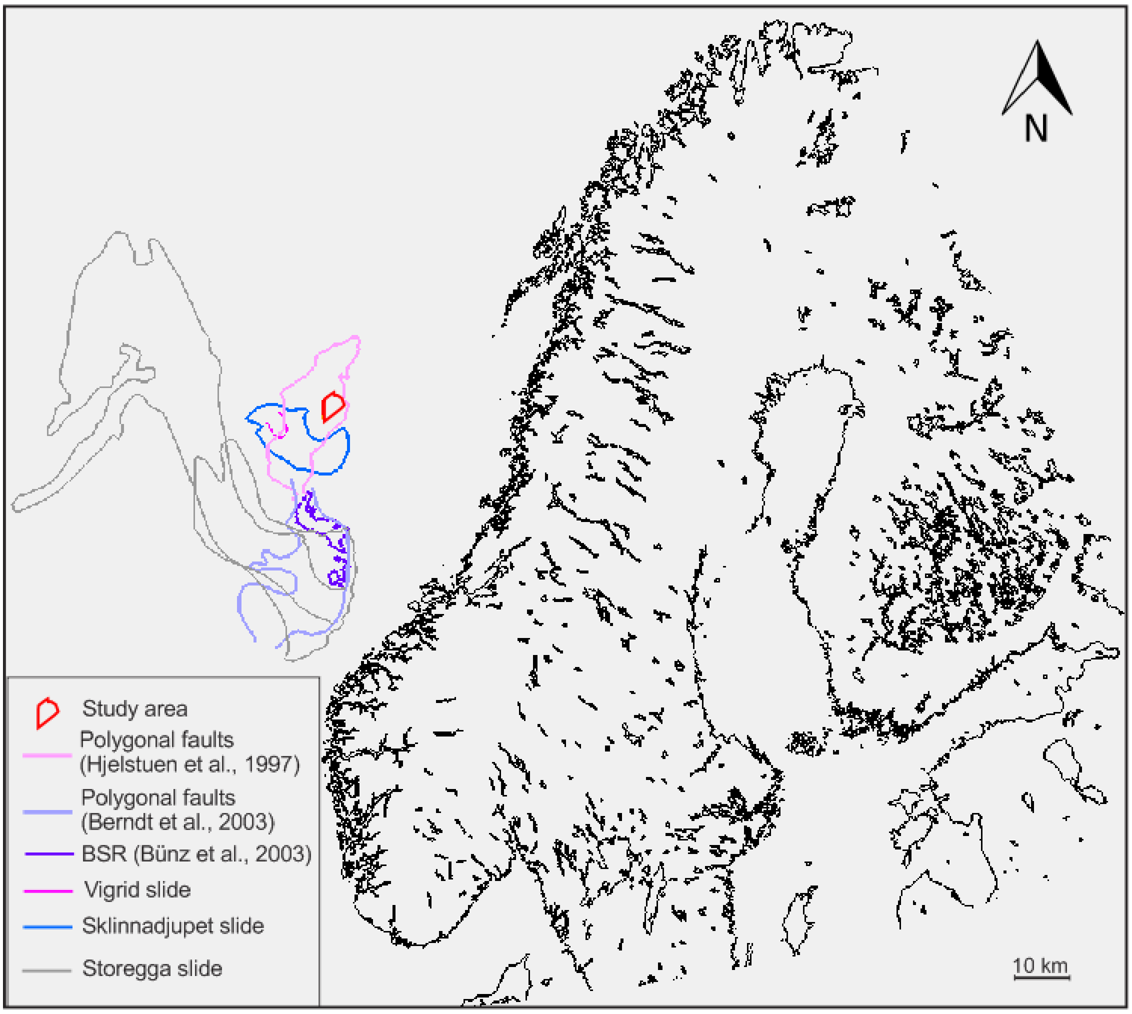

Figure 3.3: Map showing some of the previous work done in the region. The red polygon shows the specific study area for this paper.

3.3 Nomenclature

The nomenclature for the Norwegian Sea is presented in figure 3.4. This sections will give a short introduction to the lithostratigraphy of the study area. The oldest formation to be presented is the Upper-Jurassic Spekk Formation.

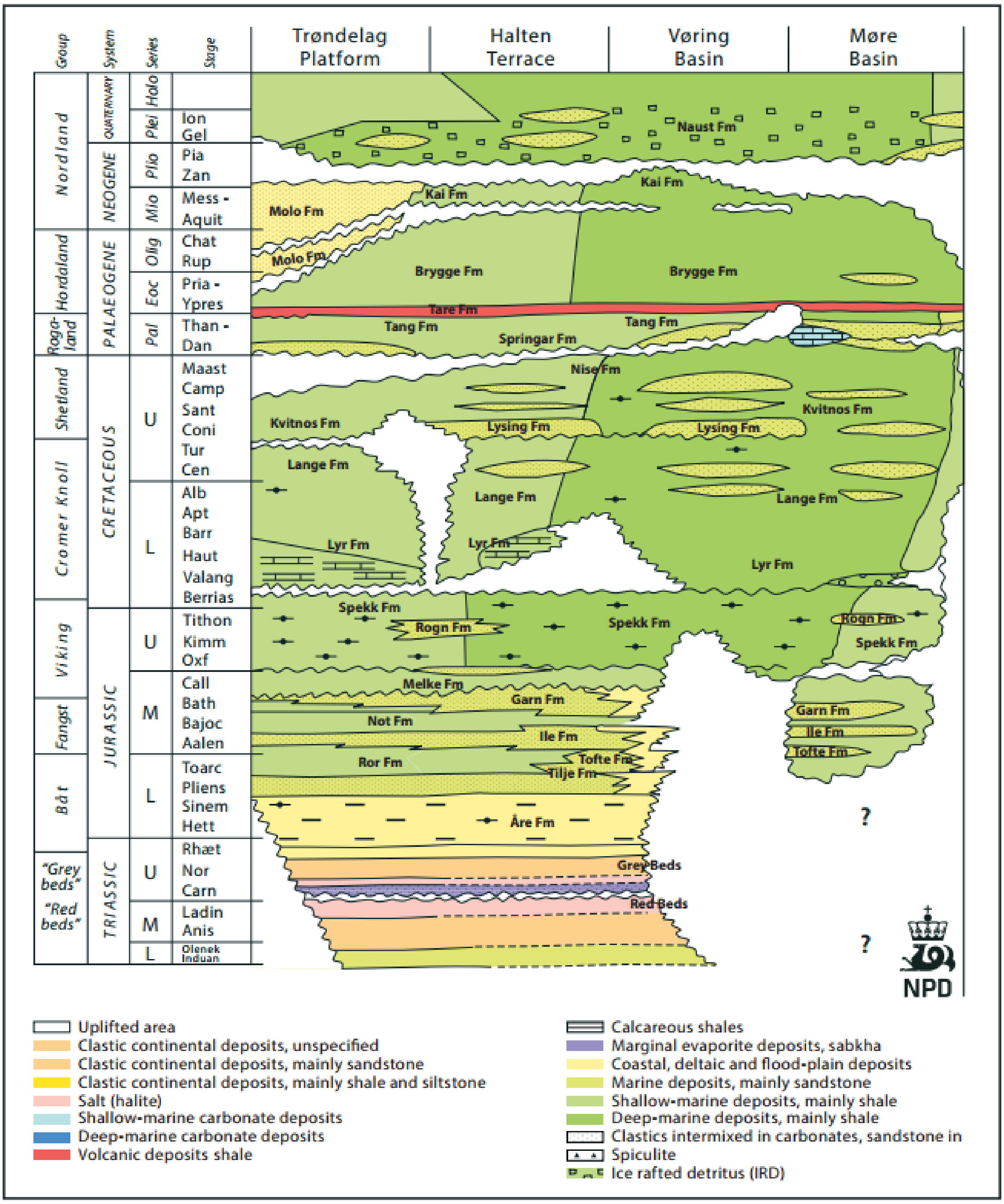

Figure 3.4: Norwegian Sea nomenclature defined by the Norwegian Petroleum directorate (NPD). The figure gives an overview over ages, groups, formations and lithology found in the region (NPD, 2012).

Spekk Formation belongs to the Viking Group. The formation is dominated by dark brown to dark grey shale, although parts of the unit may be silty. The formation has a very high organic content. IT was deposited in marine anoxic bottom water conditions and is therefore a well-preserved source rock in the Norwegian Sea. Spekk Formation is often correlated with the North Sea Draupne source rock. The Formation was deposited during Upper-Jurassic to Lower-Cretaceous (Dalland, Worsley, & Ofstad, 1988).

Lyr Formation belongs to the Cromer Knoll Group. The sediments were deposited under open marine conditions and consists of calcium carbonate-rich mudstone with interbedded carbonates. The carbonate content does however decrease towards the east in the Møre and Vøring Basins, as can be seen in Figure 3.4. Lyr Formation is also if Lower-Cretaceous age (Dalland et al., 1988).

Lange Formation also belongs to the Cromer Knoll Group. The formation is of Lower-Cretaceous age. The formation is clay-dominated with thin layers of carbonates and sandstones. The Lange sediments were deposited in a marine environment (Dalland et al., 1988).

Lysing Formation is a sandstone Upper-Cretaceous formation with dominantly fine to medium sized grains. The sandstones can be carbonate-cemented or be interbedded with shales. The interpretasions for the depositional environment varies from shallow to deep marine. Interpretations for the formation being submarine fan deposits exist as well (Dalland et al., 1988).

The Upper-Cretaceous Kvitnos Formation is a member of the Shetland Group. It consists of calcareous claystones with carbonate and sandstone stringers. The formation is continuous within the Vøring Basin. The sediments were deposited in an open marine environment (Dalland et al., 1988).

Nise Formation if also of Upper-Cretaceous age belonging to the Shetland Group. The lithology consists mainly of claystones. The claystones can be interbedded with carbonate and sandstone. The Nise Formation was deposited in an open marine setting (Dalland et al., 1988).

The last member of the Shetland Group is the Late-Createaceous Springar Formation, which consist of claystones interbedded with sandstones and carbonates. The sediments were deposited in an open marine environment (Dalland et al., 1988) .

Tang Formation belongs to the Rogaland Group. It is a claystone formation with minor sandstone and limestone-content. The Formation is of Paleocene age and was deposited in a deep marine environment (Dalland et al., 1988).

The next member of the Rogaland Group is the Late-Paleocene Tare Formation. The depositional environment for this formation was deep marine. It consists of claystones with variable content of tuff (Dalland et al., 1988).

The Brygge Formation from the Hordaland Group was deposited from Early Eocene to Early Miocene. At the present day shelf the Brygge sediments are clay-dominated. The oldest part of the Brygge Formation includes terrestrial sediments which were deposited before the opening of the Norwegian-Greenland Sea. After the Norwegian-Greenland Sea opening, ooze-dominated sediments were deposited. Clay-ooze is the main constituent in the Brygge Formation within the Vøring Basin. (Chand et al., 2011; Hjelstuen et al., 2004). Polygonal faults characterise the Brygge Formation, resulting in heavily deformed sediments (Berndt et al., 2003)

The Kai Formation consists mainly of fine-grained hemipelagic siliceous and calcareous ooze. The formation was deposited between Lower Miocene and Late Pliocene (Hjelstuen et al., 2004). Like the Brygge formation, the Kai Formation is also characterised by polygonal faults (Berndt et al., 2003). A cross-cutting reflector with high amplitude is well-defined within the Kai Formation. Because of its nature, it has been interpreted to be a diagenetic bottom-simulation reflection arising from the Opal A – Opal CT transition (Berndt et al., 2004; Brekke, 2000). The Kai Formation has its maximum thickness within the Vøring Basin with thicknesses around 750-1000ms TWT (Hjelstuen et al., 2004).

The Naust Formation was deposited during climate-driven cycles in Plio-Pleistocene. The sediments consist of glacigenic debris flows, basal tills and hemipelagic or glaciomarine oozes. The Naust Formation is characterised by large submarine slides e.g. Storegga slide, Sklinnadjupet slide and Trænadjupet slide (Chand et al., 2011; Dalland et al., 1988; Hjelstuen et al., 2004; Rise, Ottesen, Berg, & Lundin, 2005).

4 Data and methods

This chapter will first present the seismic and well data used in this thesis. The resolution of the seismic data will be discussed before the different interpretation and visualisation tools and methods will be presented. The chapter also includes a section regarding hydrate equilibrium modelling software used for finding the base of the gas hydrate stability zone (BGHSZ).

4.1 Database

4.1.1 Seismic data

The main part of the work was carried out using the three-dimensional (3D) seismic data set ST0827 from StatoilHydro. The data set is processed by CGG Veritas, Oslo, and has been 3D migrated. The extent of the data is approximately 850 km^2. The parameters for the data set are summarised in Table 1. The bandwidth and peak frequency were determined using spectral analysis.

3D seismic data set ST0827	
Distance between inlines	12.5m
Distance between crosslines	12.5m
Bin size	12.5m x 12.5 m
Record length	7500 ms
Sample interval	4 ms
Bandwidth (Hz)	4 - 86
Peak frequency (Hz)	32

Table 1: Seismic data parameters

Fles Fault Complex 1995 (FFC95) 2D data set from PGS Nopec was used in addition to ST0827. This 2D data set was mainly used in mapping the extent of a gas-hydrate related bottom-simulating reflector.

The polarity standard used in this study is the SEG of Sheriff (2006). The polarity convention is outlined in section 2.7 (Figure 2.15). The seismic data consists of zero-phase wavelet with normal polarity. An increase in acoustic impedance (positive reflection coefficient) gives a peak (red/yellow), whereas a decrease in acoustic impedance (negative reflection coefficient) gives a trough (blue) (Figure 4.1)

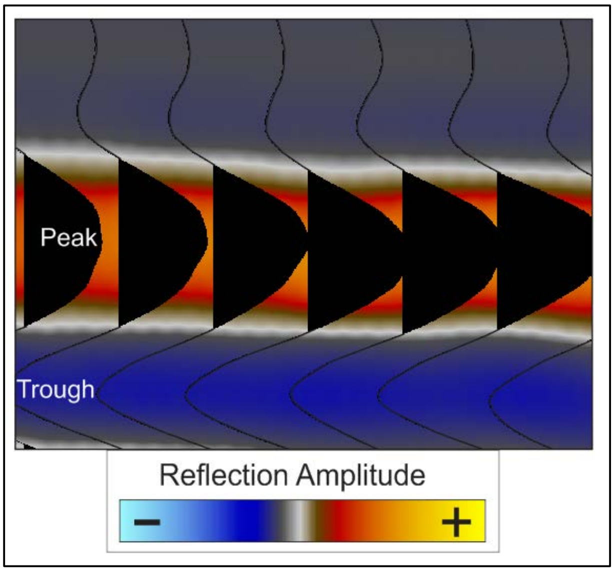

Figure 4.1: Polarity convention used in this study (SEG from Sheriff 2006). A positive reflection coefficient (peak) is given a red/yellow color, while the negative amplitude (trough) is given a blue color.

4.1.2 Well data

A set of conventional oil and gas boreholes were used for determining the geothermal gradient at the study site. These wells were also used for correlation and as an aid in the stratigraphic interpretation. The wells 6605/1-1, 6605/8-1 and 6605/8-2 were used for stratigraphic interpretation and correlation. The geothermal gradient was calculated using 6605/1-1, 6605/8-1, 6605/8-2 and 6604/10-1. The ages for the stratigraphic units are from well 6704/12-1, and from Hansen et al. (2005). Figure 4.2 shows the location of the wells relative to 3D data set ST0827 and the FFC95 2D lines.

Checkshot surveys for well 6605/8-2 (StatoilHydro) and 6605/8-1 (Norsk Hydro) were used in depth and thickness estimations. Checkshots give information about the velocity at different depths, which allows for time-depth conversion. The checkshots data used in this study contain both interval and average velocities for given depths.

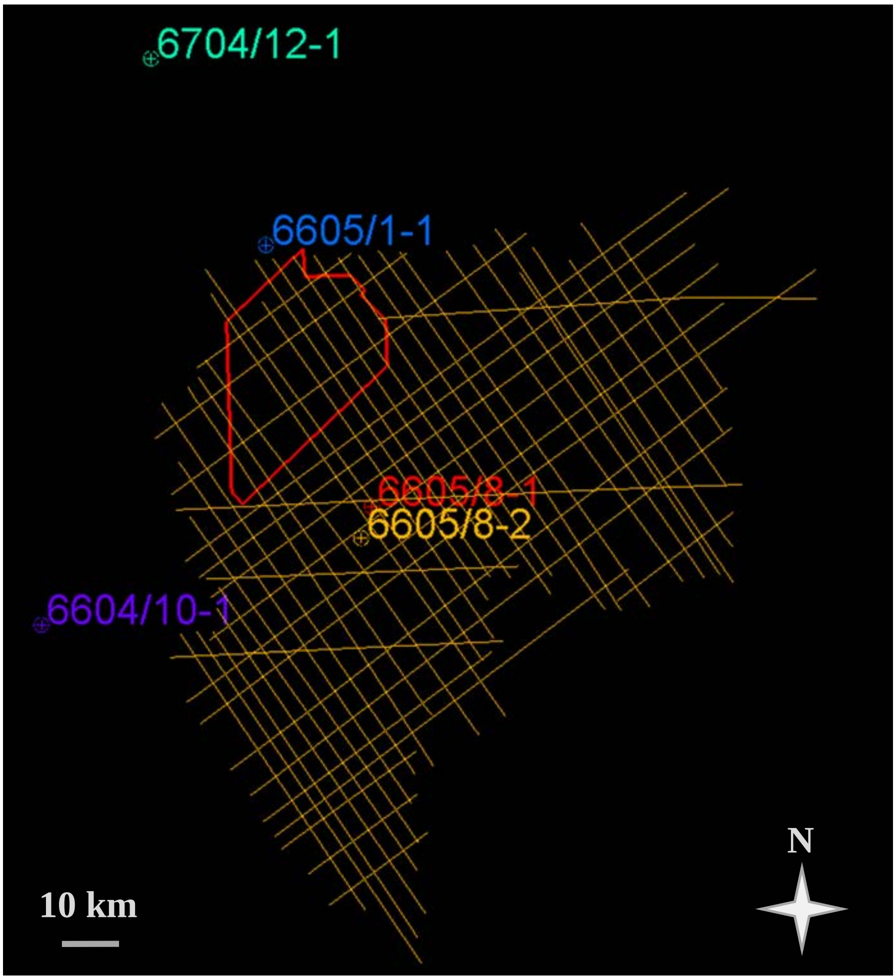

Figure 4.2: Map showing 3D seismic survey ST0827 as a red polygon. The orange lines show FFC95 2D lines. The locations of the wells 6704/12-1, 6605/1-1, 6605/8-1, 6605/8-2 and 6604/10-1 are shown with circles.

4.2 Seismic resolution

Seismic resolution is defined as the ability to distinguish between two individual reflectors, but it also determines how large a feature needs to be in order to be seen in seismic (Brown, 2004; Sheriff, 1985). The resolution of seismic data is determined by the wavelength (*Equation 16*).

$$\lambda = \frac{v}{f} \qquad \textit{(Equation 16)}$$

where λ is the wavelength (m), f is the frequency (Hz) and v is the velocity (m/s).

When seismic waves travel through the Earth, frequencies will be attenuated as the wave travels progressively deeper. High frequencies are attenuated more rapidly than low frequencies. The seismic velocities will generally increase with depth due to a higher grade of compaction. Since wavelength is proportional to the velocity and inversely proportional to frequency, the wavelengths will increase with depth (Figure 4.3) (Brown, 2004; Bulat, 2005). The seismic resolution will thus decrease with depth. This means that with increasing depth, a feature needs to be larger to be detected and that two individual reflectors need to be spaced further apart to be distinguished.

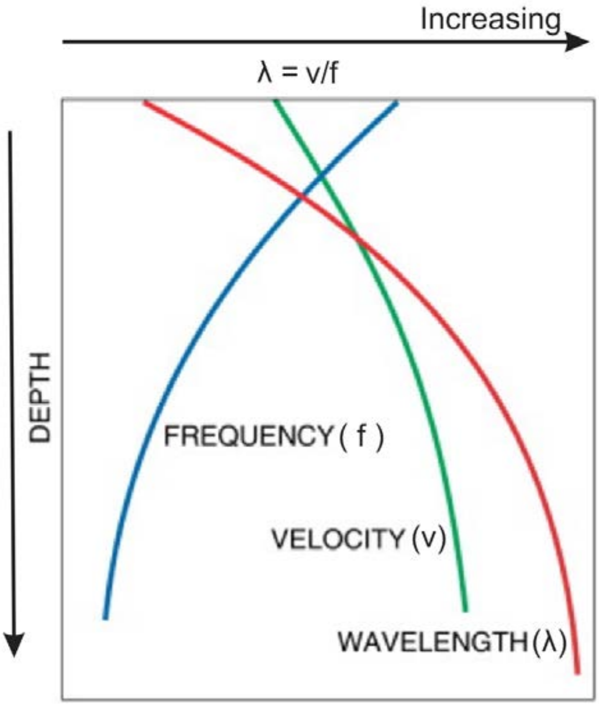

Figure 4.3: Illustration of how frequency decreases, while velocity and wavelength increase with depth. Figure modified from Brown (2004)

4.2.1 Vertical resolution

Vertical resolution refers to the ability to distinguish the top and base of a thinning sedimentary bed. Vertical resolution is also referred to as the limit of separability, i.e. the limit of when two seismic events corresponding to different depths can be separated. This limit is taken as 1/4 of the wavelength (*Equation 17*) (Badley, 1985; Brown, 2004; Bulat, 2005).

$$Vr = \frac{\lambda}{4} \qquad \textit{(Equation 17)}$$

Where Vr is the vertical resolution (m) and λ is the wavelength (m).

As long as two reflecting interfaces are separated by 1/2 of a wavelength or more, the wavelets won't interfere and two separate reflections will be produced. If the space between interfaces approaches 1/4 of the wavelength, constructive interference will begin and be maximised when the separation is equal to one-quarter of the wavelength. This thickness at which the constructive interference is at its maximum, is known as the "tuning thickness". When the separation of interfaces is less than 1/4 of the wavelength, destructive interference starts and continues until the limit of visibility is reached. The limit of visibility is generally taken to 1/30 of the wavelength. This is illustrated in figure 4.4, where a high-velocity wedge of limestone is encased in lower-velocity shale. The wavelet in this figure is a minimum-phase wavelet (Badley, 1985; Brown, 2004).

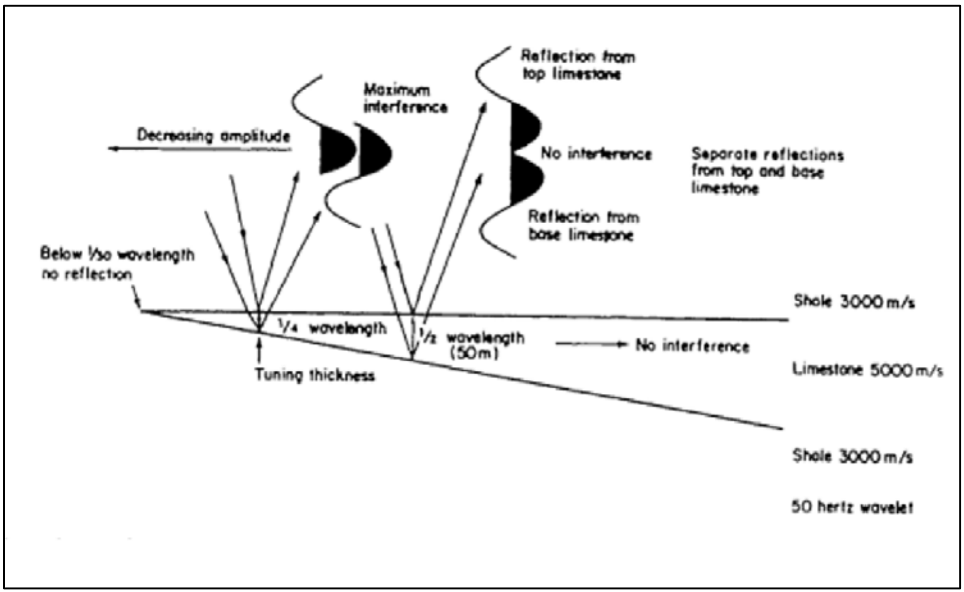

Figure 4.4: Illustration of the interference effects associated with a high-amplitude wedge encased in lower acoustic- impedance medium. Figure from Badley (1985).

4.2.2 Horizontal resolution

Horizontal resolution is the ability to distinguish between two reflectors displaced horizontally with respect to each other. The horizontal resolution also determines the size a feature needs to have to be detectable (Brown, 2004; Sheriff, 1985). Since seismic waves travel as wavefronts and not as rays, the reflection is not generated from a small point on a reflector but from a roughly circular zone instead. This circular area of the subsurface that reflects the seismic wave, is known as the Fresnel zone (Figure 4.5). The Fresnel zone of the first wavefront is dependent on the arrival of the following wavefront, which arrives 1/4 of the wavelength behind. The reflection from the second wavefront will interfere destructively with the reflection from the first. The horizontal resolution on unmigrated data is defined by the width (diameter) of the first Fresnel zone (*Equation 18*).

$$rf = \frac{v}{2}\sqrt{\frac{t}{f}} \qquad \textit{(Equation 18)}$$

Where rf is the Fresnel zone (diameter) (m), f is frequency (Hz), t is two-way time (s) and v is velocity (m/s).

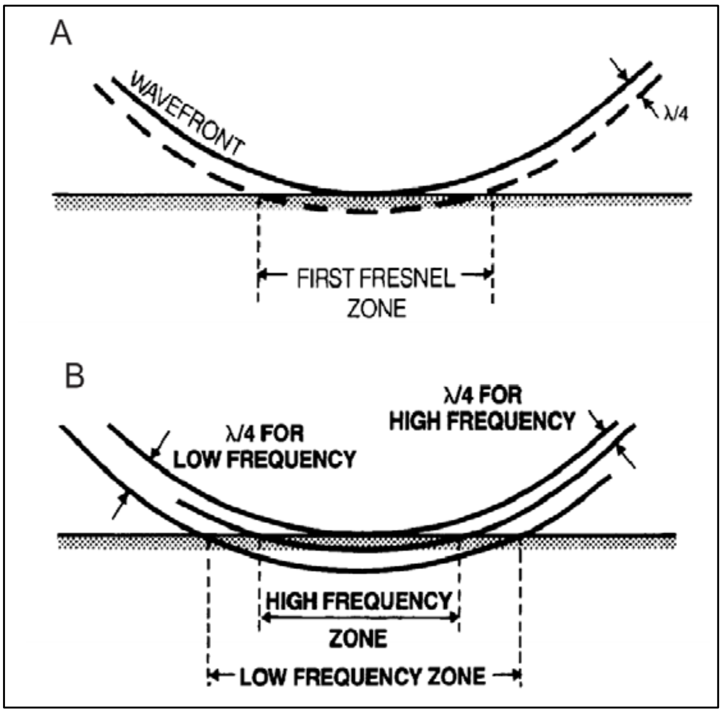

Figure 4.5: Reflection of wavefronts from the area known as the Fresnel zone. A) The diameter of the first Fresnel zone. B) Illustration on how the Fresnel zone depends on frequency (or wavelength). High frequency waves give a smaller Fresnel zone and a better horizontal resolution than Fresnel zones put up by low frequency waves. Modified from Sheriff (1985).

In the processing of seismic data, a technique known as migration will reduce the size of the Fresnel zone, thus improving the horizontal resolution (Brown, 2004). During migration, the 2D seismic data Fresnel zone is collapsed to an ellipse. For 3D the Fresnel zone is reduced to a small circle (Figure 4.6). The horizontal resolution for migrated seismic data is given by *Equation 19* (Brown, 2004; Bulat, 2005; Sheriff, 1985).

$$Hr = \frac{\lambda}{4} \qquad \textit{(Equation 19)}$$

Where Hr is the horizontal resolution (m) and λ wavelength (m).

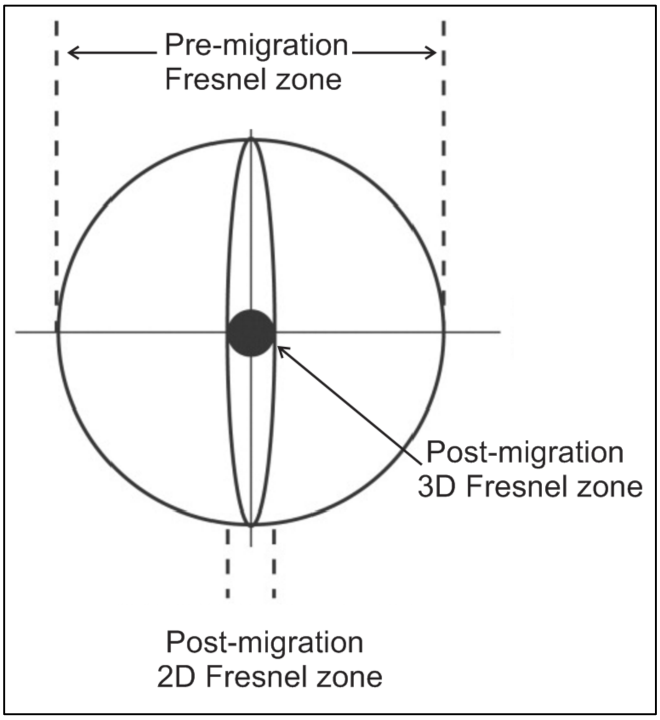

Figure 4.6: Fresnel zone for unmigrated and migrated seismic data. Migration on 2D seismic data only collapses the Fresnel zone in inline direction. Migration on 3D seismic data reduces the Fresnel zone to a small circle. Figure modified from Brow (2004).

4.2.3 Vertical and horizontal resolution for 3D survey ST0827

The vertical and horizontal resolution for the 3D seismic data set (ST0827) used in this study can be calculated using the peak frequency of 32 Hz and an average p-wave velocity of 2200 m/s. The wavelength of the data set can be calculated using *Equation 16*:

$$\lambda = \frac{v}{f} = \frac{2200\ m/s}{32\ Hz} = 68.75\ m$$

The vertical resolution is found using *Equation 17:*

$$Vr = \frac{\lambda}{4} = \frac{68.75\ m}{4} = 17.2\ m$$

The pre-migration horizontal resolution (width of Fresnel zone) is calculated using *Equation 18.* The horizontal resolution is here given for Top Kai (1850 ms TWT) and Top Brygge (2400 ms TWT).

$$rf_{Kai} = \frac{v}{2}\sqrt{\frac{t}{f}} = \frac{2200m/s}{2}\sqrt{\frac{1850\ ms}{32\ Hz}} = 264.5m$$

$$rf_{Brygge} = \frac{v}{2}\sqrt{\frac{t}{f}} = \frac{2200m/s}{2}\sqrt{\frac{2400\ ms}{32\ Hz}} = 301.2m$$

The post-migration horizontal resolution is found using Equation 19:

$$Hr = \frac{\lambda}{4} = \frac{68.75\ m}{4} = 17.2\ m$$

4.3 Interpretation and visualisation methods

The interpretation, attribute analysis and visualisations in this study are done using Schlumberger's Petrel 2014 software. The Petrel software includes several tools and features that have been used for seismic interpretation.

4.3.1 Interpretation of 3D and 2D seismic data

Seismic horizons were interpreted in the seismic data using seeded 2D autotracking. An increment of 50-100 was used for inline and crossline interpretation in the 3D seismic data set (Figure 4.7A). When needed, guided autotracking and manual tracking was used at a smaller increment. Seeded 3D autrotracking and the paintbrush tool was applied to complete the horizons. When needed, the 2D data set was used to supplement the 3D data. Seeds were then picked at an increment determined by the acquisition for the 2D data (Figure 4.7B). For the mapping of the BSR, manual tracking was frequently needed.

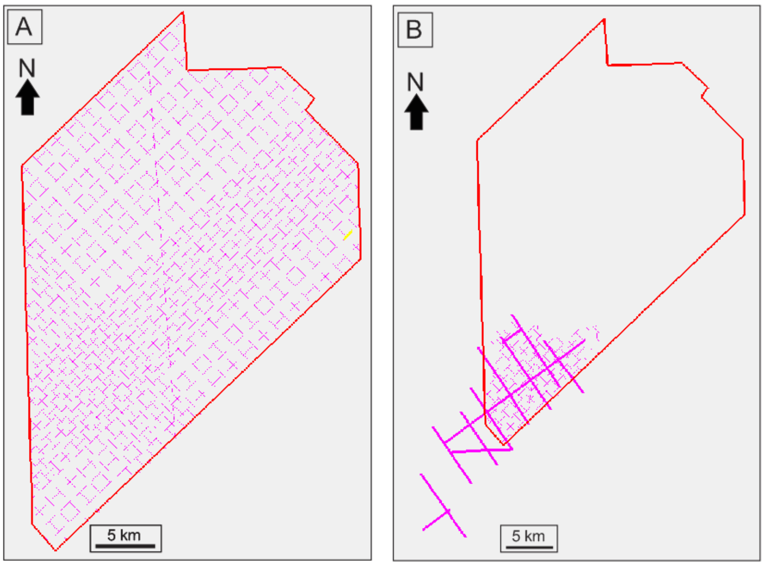

Figure 4.7: A) Example of horizon interpreted using the 3D data set. B) Example of interpretation where 2D lines were used in addition to the 3D data.

4.3.2 Seismic attributes

Already in the 1970s geoscientist used seismic attributes when doing seismic interpretation. Taner & Sheriff (1977) described how seismic attributes can be used in stratigraphic interpretation and hydrocarbon determination. Seismic attributes are components of seismic data that can be obtained by measurement, computation or other methods. They can provide information about features or patterns in the subsurface. Seismic attributes can be divided into two groups: Physical attributes and geometrical attributes.

Physical attributes are related to the physical parameters of the subsurface, e.g. lithology and fluid content. Examples of physical attributes are reflection strength, instantaneous frequency, instantaneous phase and polarity. Geometrical attributes such as dip, azimuth and discontinuity have an objective to enhance the visibility of subsurface characteristics (Chopra & Marfurt, 2005; Taner, Koehler, & Sheriff, 1979; Taner & Sheriff, 1977). In Petrel there are two options for using seismic attributes in the interpretation: volume attributes and surface attributes. Each exhibits numerous attribute tools, but nnly the attributes studied in this paper will be described.

A variance attribute cube (volume) can be created to highlight discontinuities. This method estimates the horizontal continuity of amplitude. The variance method measures differences from a mean value. This attribute is useful in detecting structural or stratigraphic features. It is especially useful when mapping faults (Schlumberger, 2010). In this study the variance attribute was used to highlight hydrothermal vents.

Another attribute found under the volume attributes is instantaneous frequency, which is defined as the time derivative of instantaneous phase. This attribute represents the mean frequency of the data spectrum (Schlumberger, 2010) . The instantaneous frequency attribute is often used to estimate seismic attenuation, e.g. the frequencies found above and beneath a BSR (BGHSZ).

Root-mean-square (RMS) amplitude attribute is used to highlight strong amplitudes. This methods calculates the square root of the sum of squared amplitudes divided by the number of samples within a specified volume (time window) The RMS attribute is often used to identify and map amplitude anomalies arising from e.g. hydrocarbons or lithology variations (Schlumberger, 2010)

4.3.5 Depth and thickness calculations

For depth and thickness calculations, the TWT from the seismic data is used together with velocities given by the checkshot surveys. The following equation has been used when calculating thicknesses:

$$z_i = \frac{v_i \,.\, (TWT_{base} - TWT_{top})}{2} \qquad \textit{(Equation 20)}$$

Where z_i is the interval thickness, v_i is the interval velocity, TWT_{base} and TWT_{top} are two-way-times given at the base and top of the interval.

For calculating the depth to a given reflector, the following equation was used:

$$z = \frac{v_{avg} TWT_z}{2} \qquad \textit{(Equation 21)}$$

Where z is the depth, v_{avg} is the average velocity from the surface to the given depth and TWT_z is the two-way-time at the reflector.

It needs to be stressed that the velocities from the checkshots are given for the exact location of the specific well (6605/8-1) or 6605/8-2). The data set (ST0827) is located approximately 20 km northwest of these wells. Thus the actual velocity for the intervals covered by the seismic data may vary from the ones found in the checkshots for the wells. The calculated depths and thicknesses should therefore be seen as estimates.

4.4 Hydrate equilibrium modelling

The CSMHYD program developed by Sloan (1998) was used when modelling the gas hydrate-stability in the study area. This software allows for a prediction of hydrate formation. The pressure and temperature conditions for gas hydrate-formation can be calculated with or without the presence of inhibitors, e.g. salt or alcohol. It is possible to vary the composition of the hydrate, i.e. how much of a given gas it should contain. The program also gives an overview over which hydrate structure is likely to form (see section 2.5.1 for the different structures).

5 Results

This chapter presents the interpretations and observations done for the 3D seismic data set ST0827 with supplementation from the FFC95 2D data set and welldata. The focus of the interpretation is determined by the objective. The two goals as presented in the objective are as follows: to understand controlling mechanisms for the occurrence and development of focussed fluid flow features, and to map a gas hydrate-related bottom-simulating reflector (BSR) and understand its origin. Seismic attribute volumes and surfaces have been created to highlight features and to extract more information from the seismic data.

5.1 Stratigraphy

The seismic stratigraphy for the study area was interpreted using correlation of well data from wells in the vicinity of the 3D data set (Figure 5.1). Because there are no wells included within the 3D data set used in this study, the horizons were traced from well 6607/12-1 and 6605/1-1 located within two other 3D seismic data sets. The location of the wells relative to the 3D survey is shown in Figure 4.2. The chronostratigraphic information is from Hansen et al. (2005), Hjelstuen et al. (2004) and Dumke et al. (2014). The focus areas in the mentioned papers are located northwest of ST0827, thus the need for correlation. The seismic stratigraphy is shown in Figure 5.2. The stratigraphic interpretation focuses on the uppermost 3.5-4.0 seconds of the section. The deeper formations are dominantly used for the interpretation of sill intrusions and to some extent hydrothermal vents.

The study area comprises several sedimentary formations. The shallowest is the Naust Formation, followed by Kai Formation, Brygge Formation, Tare Formation, Tang Formation and Springar Formation. Completion reports from wells 6605/1-1, 6605/8-1 and 6605/8-2 report deeper-lying formations, but these are not interpreted in this study. Deeper formations are Nise Formation, Kvitnos Formation, Lysing Formation and Lange Formation (NPDa, 2015; NPDb, 2015; NPDc, 2015)

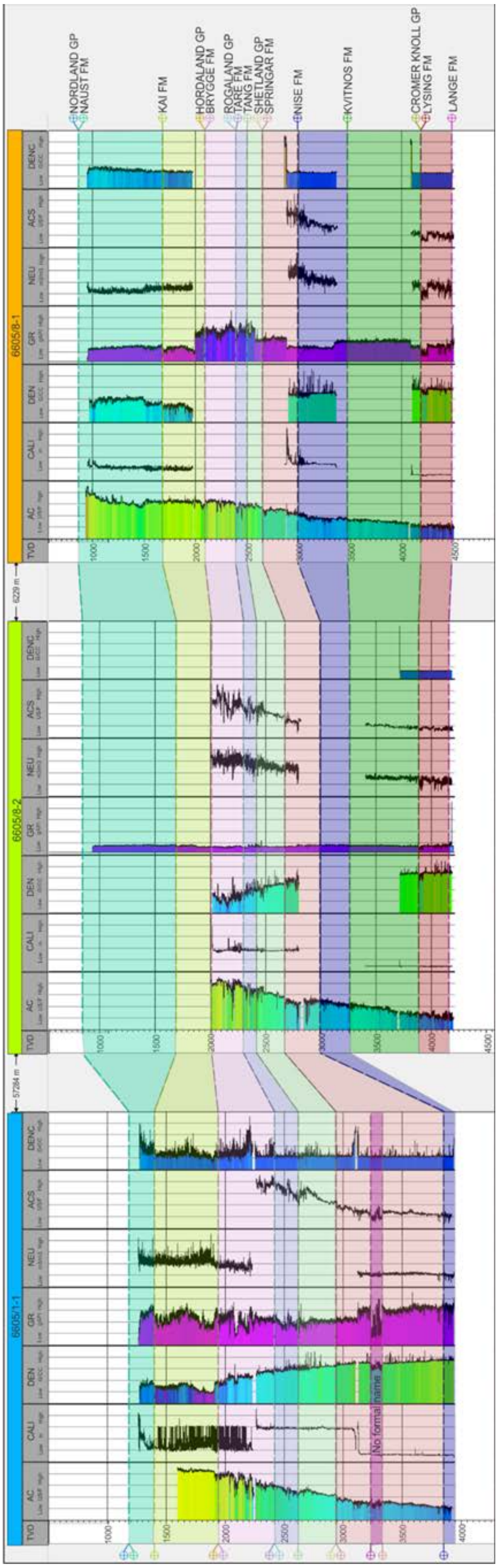

Figure 5.1: Well-correlation between wells 6605/5-1, 6605/8-2 and 6605/8-1. For location of wells, see Figure 4.2

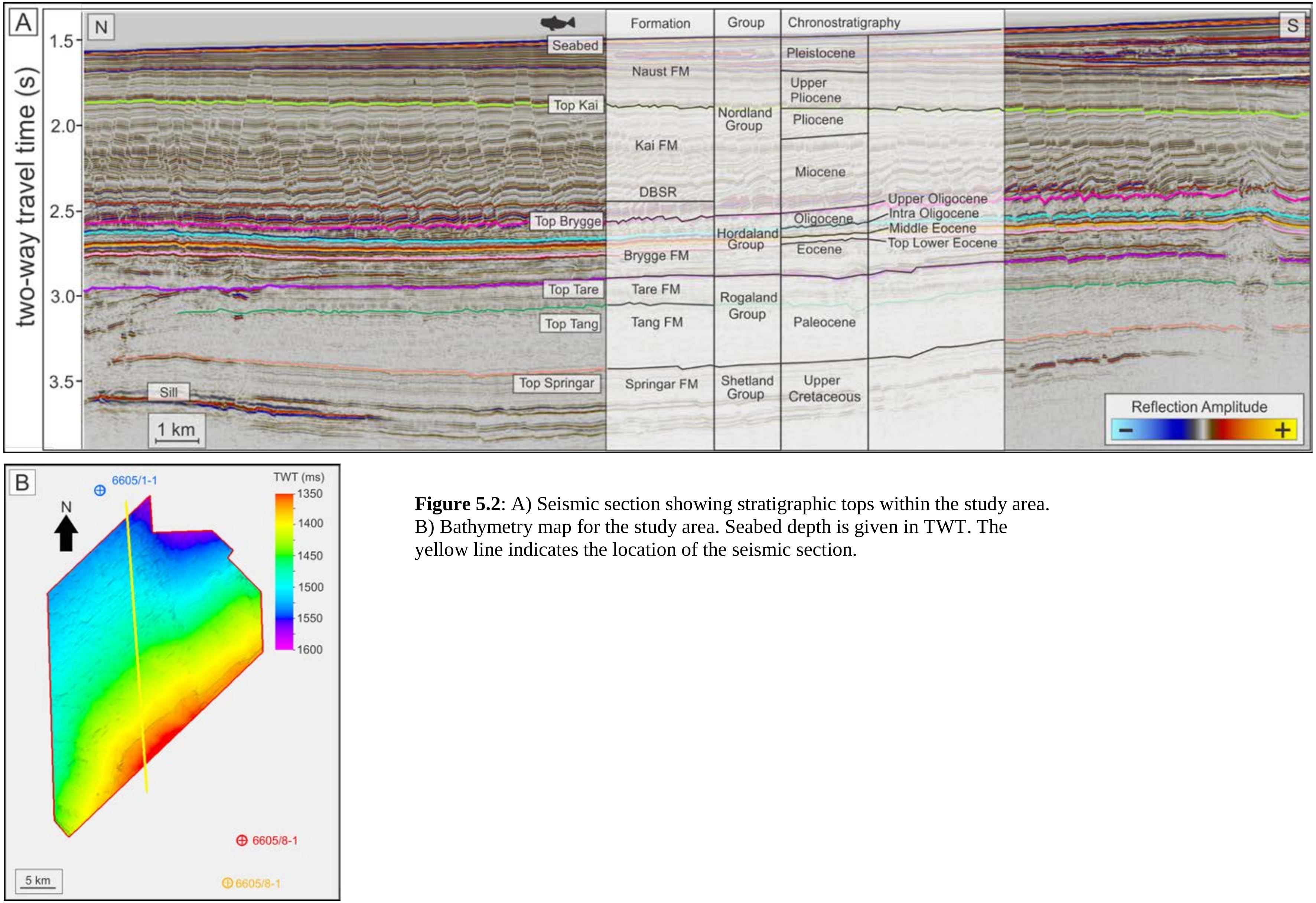

Figure 5.2: A) Seismic section showing stratigraphic tops within the study area. B) Bathymetry map for the study area. Seabed depth is given in TWT. The yellow line indicates the location of the seismic section.

5.1.1 Formations

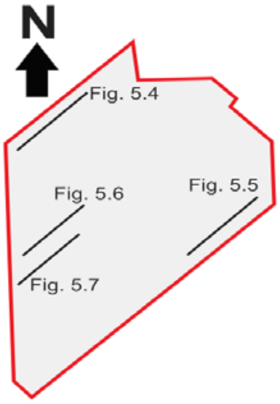

Figure 5.3: Location of seismic sections in Figure 5.4, 5.5, 5.6, and 5.7.

This subsection contains a brief presentation of the interpreted formations. The location for seismic sections are indicated in Figure 5.3. The Naust, Kai, Brygge, Tare, Tang and Springar formations are all present throughout the entire study area.

The Naust Formation (Figure 5.4) encompasses the uppermost unit of sediments. The internal reflections in the formation have medium to high amplitudes and are mostly continuous, except in the south-south-eastern part where the reflections are chaotic. These chaotic reflections are interpreted to be mass-transport deposits (Figure 5.5). Glacial debris flows are common in the Naust Formation (Hjelstuen et al., 2005; Rise et al., 2005). Naust formation isn't faulted, but seems slightly deformed by underlying faults. In the southernmost part, a BSR is detected. The BSR is sitting at approximately 1780 ms TWT. The mass-transport deposits and the BSR will be discussed in further detail later in this chapter.

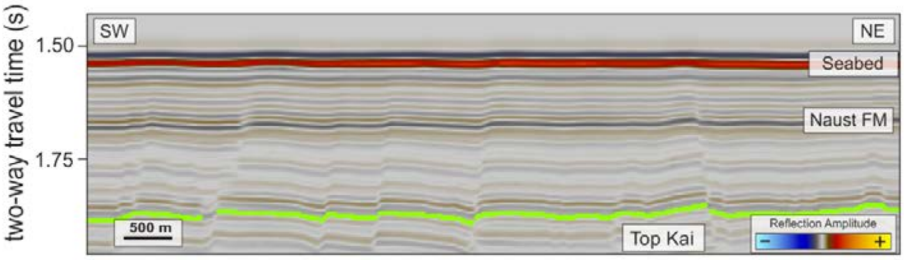

Figure 5.4: Seismic section from the north-west of the study area showing continuous well-stratified reflections of the Naust Formation. For location, see Figure 5.3.

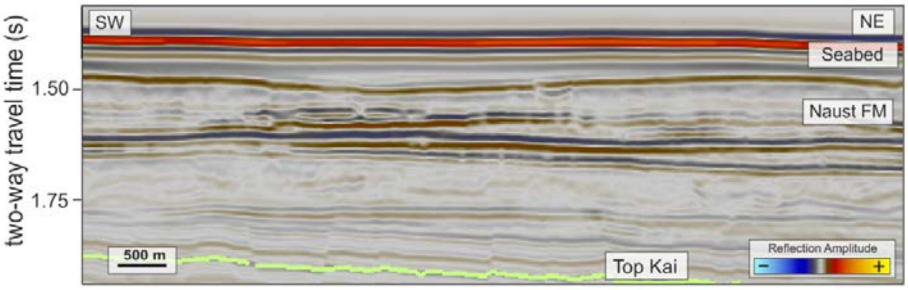

Figure 5.5: Seismic section showing chaotic reflections within the Naust Formation. The location of the line is indicated in Figure 5.3.

The Kai Formation is characterised by faults that cut through the entire formation, including the top horizon (Figure 5.6). However, the deepest part of the formation has a higher density of small-offset faults. These are interpreted to be polygonal faults. The Kai Formation consists of ooze-dominated sediments, and as mentioned in chapter 2, polygonal faults are common in fine-grained sediments (Cartwright et al., 2003) The uppermost part of the formation has reflections of a lower amplitude than those of deeper reflections. At the bottom of the Kai Formation, a crosscutting horizontal reflection appears. This is interpreted to be a diagenetic bottom-simulating reflector similar to that observed further south (and south-east) in the Vøring and Møre Basins by e.g. Andreassen et al, (2000), Bugge (1983), Bugge et al. (1988), Bünz et al. (2003), Mienert et al. (1998) and Chand et al. (2011).

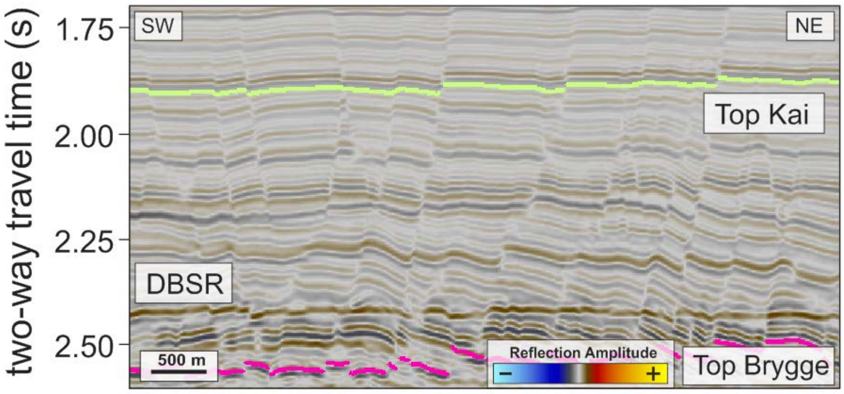

Figure 5.6: Seismic section showing the Kai Formation. Note the flat reflector interpreted to be a diagenesis-related bottom-simulating reflector (DBSR).

The Top Brygge horizon (pink) marking the boundary between the Kai Formation and Brygge Formations is heavily affected by small-offset faults interpreted to be polygonal faults. In the Vøring Basin the Brygge Formation consists dominantly of clay-ooze, suitable for polygonal faulting. These faults occur dominantly at the top of the formation with low amplitude reflections. The middle section is characterised by continuous intraformational reflectors of higher amplitudes. These are shown in Figure 5.2 as the Intra Oligocene, Middle Eocene and Top Lower Eocene horizons. The Brygge Formation is also characterised by mounds. Some of the mounds are formed mostly at the intraformational reflectors, whereas other mound-structures include the Top Brygge horizon as well.

The uppermost part of the Tare Formation is characterised by low amplitude reflections. The amplitudes increase towards the bottom of the formation. The Tare Formation is greatly affected by fluid flow features interpreted to be hydrothermal pipes (vents) (Figure 5.7). The pipes cut through the formation, leaving chaotic and disturbed reflections. In some areas, mound-structures can be found within the formation.

The Tang Formation encompasses low-amplitude reflections. As the overlying Tare Formation, Tang Formation too is affected by fluid flow features. No mounds are found within the Tang Formation.

Top Springar Formation is characterised by low-amplitude reflectors. Some intraformational high-amplitude reflectors occur. The lowermost part of the Springar Formation shows some reflectors cutting through the otherwise stratified reflections. These high-amplitude reflectors are interpreted to be sill intrusions.

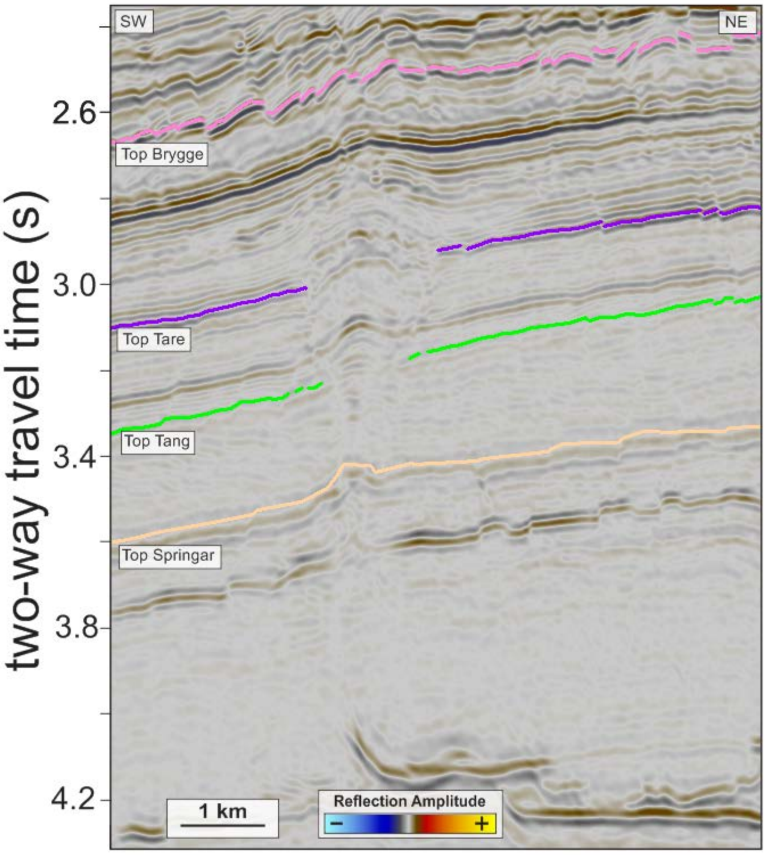

Figure 5.7: Seismic section showing Brygge, Tare, Tang and Springar formations including a fluid flow feature. Note the high-amplitude intraformational reflectors in Brygge Formation.

5.2 Faults

Deep-seated normal faults are observed in the survey. In plan view the faults can be seen as lineaments (Figure 5.8C). The lineaments are NNW-SSE trending. The faults displace the strata within the Upper Cretaceous Springar Formation up to Brygge Formation. At the top of the Brygge Formation small-offset faults become dominant. Figure 5.8 shows seismic sections over faults in the deeper part of the stratigraphy.

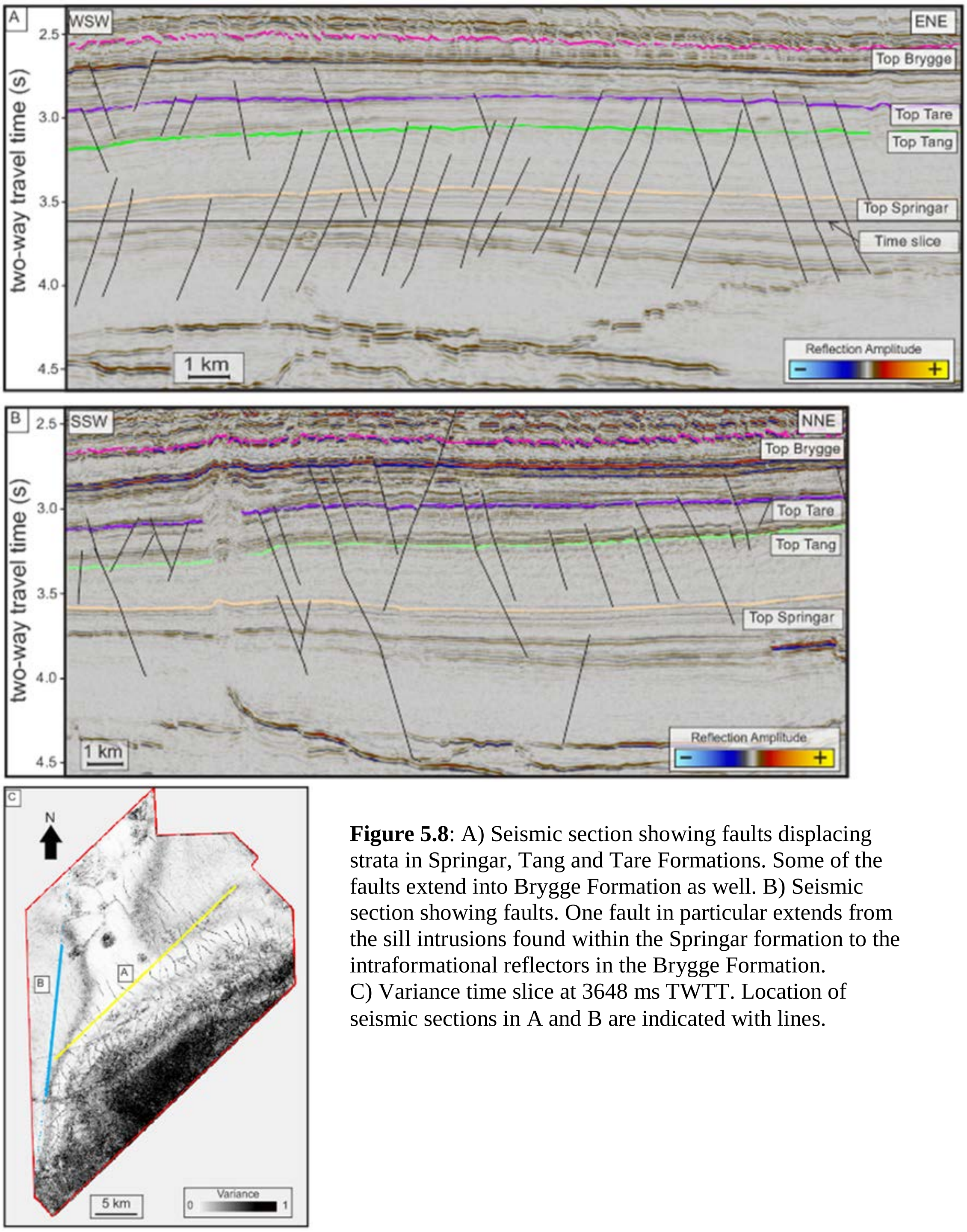

Figure 5.8: A) Seismic section showing faults displacing strata in Springar, Tang and Tare Formations. Some of the faults extend into Brygge Formation as well. B) Seismic section showing faults. One fault in particular extends from the sill intrusions found within the Springar formation to the intraformational reflectors in the Brygge Formation.
C) Variance time slice at 3648 ms TWTT. Location of seismic sections in A and B are indicated with lines.

5.2.1 Polygonal faults

Small-offset faults are abundant and have been mapped in the entire study area. The plan view-pattern formed by the faults shows a polygonal geometry with no consistent strike orientation. The planar pattern varies from highly polygonal, to curved to rectangular (Figure 5.9). Because of the appearance, these faults are interpreted to be polygonal faults comparable with other interpretations on the mid-Norwegian continental margin by e.g Berndt et al. (2003), Bünz et al. (2003), Chand et al. (2011) and Hustoft et al. (2007). In cross-section the faults have dominantly normal displacements. The faults have vertical throws between 10 ms and 25 ms TWT. Several different levels of the stratigraphy are heavily affected by these small-offset faults (Figure 5.10C). The faults occurring above the top Brygge Formation have a different spacing than those at Tare, Tang and Springar formations. The middle section of the Brygge Formation however does not show the same density of faults as the strata below and above do. A variance time slice shows how the middle part of the Brygge Formation is relatively quiet in terms of not being affected by faults (Figure 5.10A). Figure 5.10B shows how the transition from Top Brygge Formation into the bottom of the Kai Formation is characterised by polygonal faults. These faults are found in distinct layers, implying that they are not formed due to tectonic activity (Berndt et al., 2003; Bünz et al., 2003).

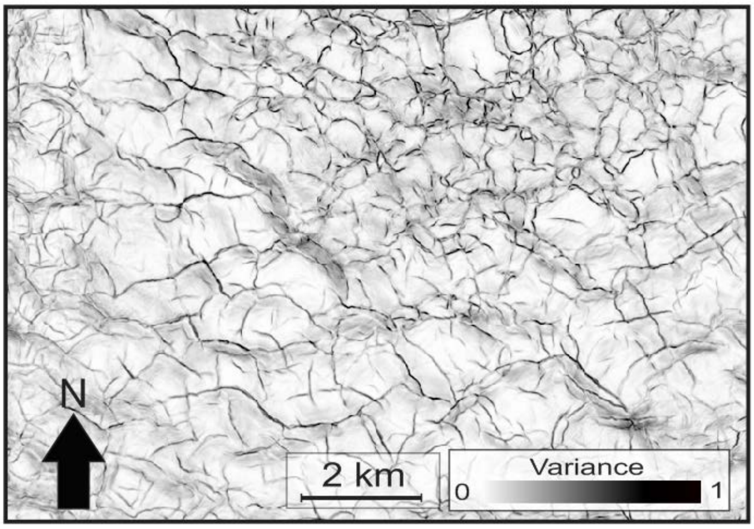

Figure 5.9: Variance map showing the polygonal pattern formed by small-offset faults. Location is shown in Figure 5.10B.

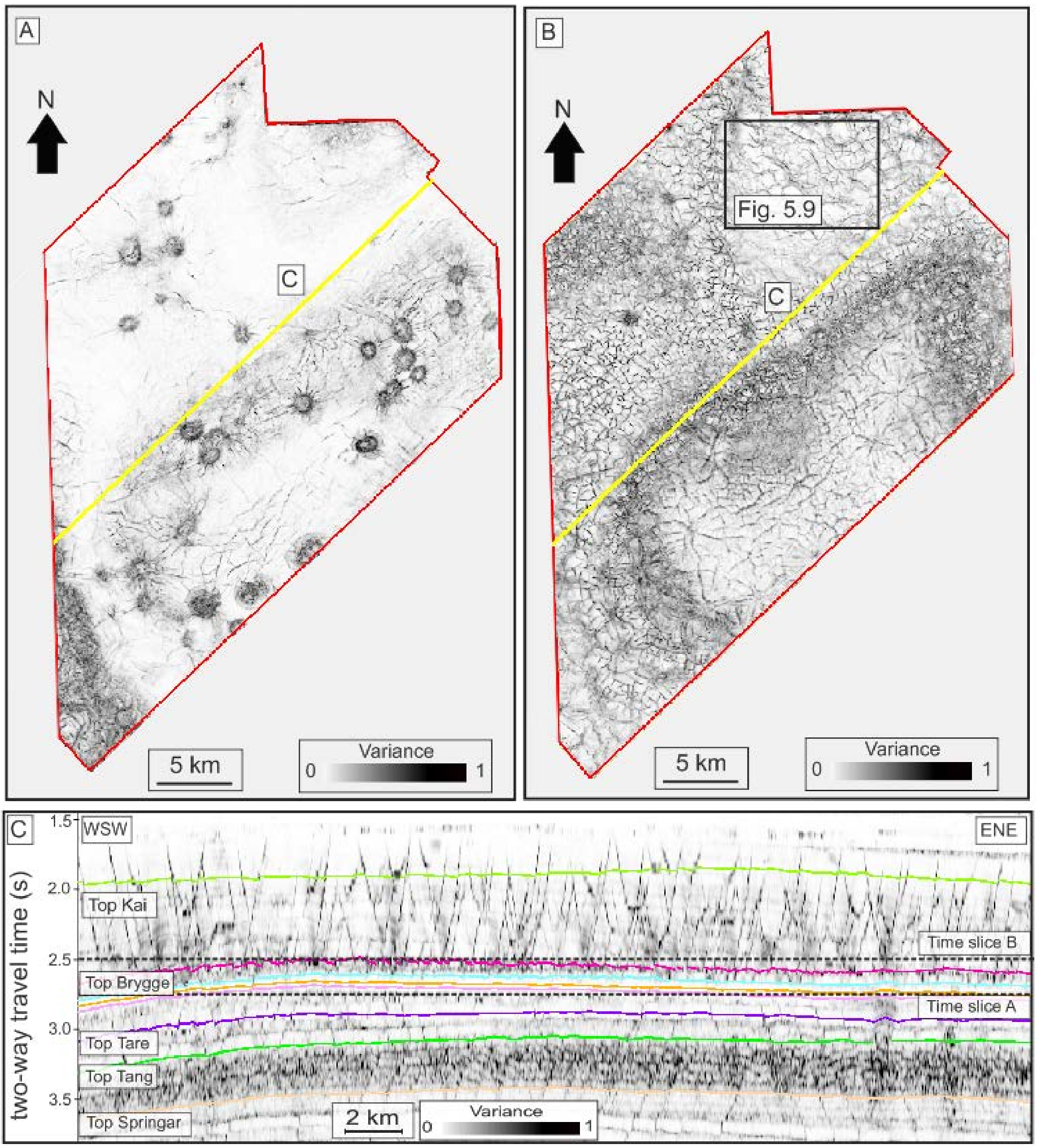

Figure 5.10: A) Variance time slice across the middle part of the Brygge Formation at 2750 ms TWTT. The circular features will be discussed later in this chapter. B) Variance Time Slice taken at the Top Brygge horizon/bottom of the Kai Formation at 2500 ms TWTT.C) Variance cross-section showing how the stratigraphy of the study area is affected by faults. Note how the faults continue across the Top Kai horizon and into the shallower Naust Formation.

5.3 Volcanic intrusions

As outlined in chapter 3, the area has been subject to intrusive events. These events can be detected in the seismic data as high amplitude-reflectors occurring among otherwise low amplitude-reflections (Figure 5.11). In the study area, such high amplitude-reflections occur in Upper Cretaceous strata between 3.8 to 5.5 s throughout the survey. This coincides with the volcanic events during Paleocene-Eocene that emplaced sills in both Vøring and Møre Basins (Berndt, Planke, & Alvestad, 2001; Planke et al., 2005). The reflections start with a peak, indicating an increase in acoustic impedance. This is expected for sill intrusions as they tend to possess higher densities and velocities than sedimentary rocks. As Figure 5.11 shows, the reflections terminate abruptly.

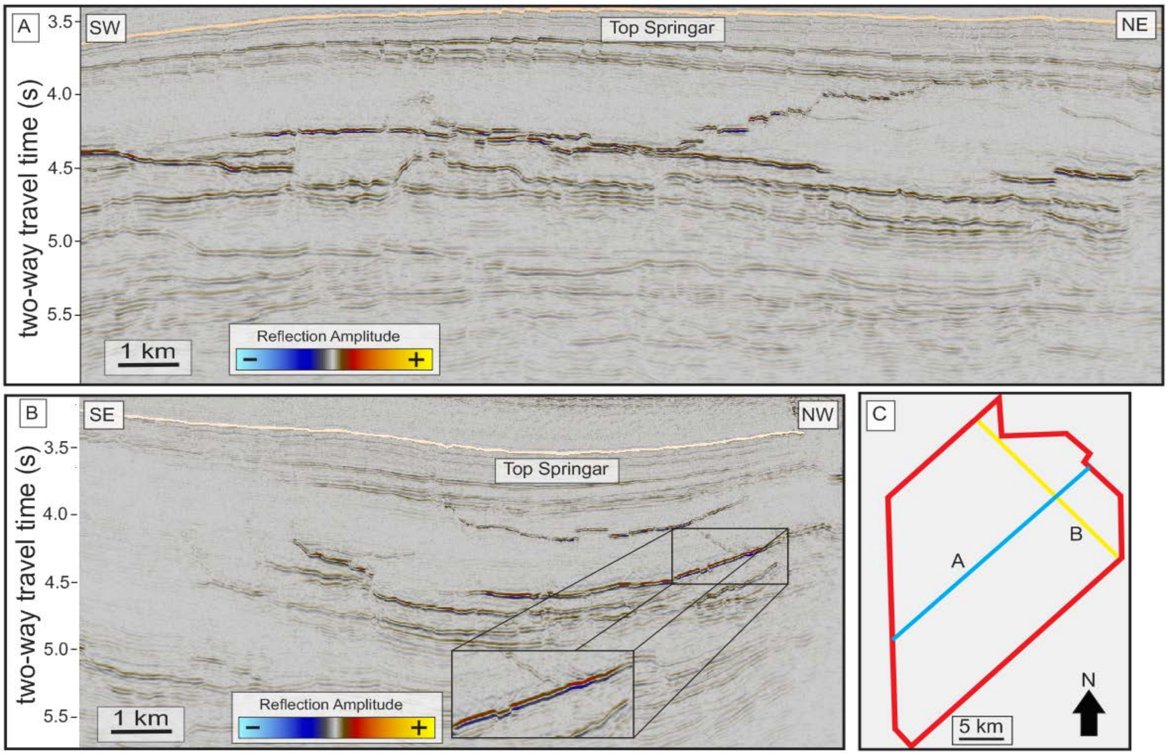

Figure 5.11: A) Seismic section showing high amplitude-reflections within Upper Cretaceous strata beneath the Top Springar horizon. Note how the reflections in A are present throughout the survey.
B) Seismic section showing high amplitude-reflections in crossline direction. A close-up shows how the reflections occur as peaks (positive amplitudes). Note how the strong amplitudes are absent in the SE.
C) Location of seismic sections in A and B are indicated with blue and yellow line, respectively.

High amplitudes, abrupt terminations, local transgression and a saucer-shape configuration are criteria proposed by Planke et al. (2005) to interpret a reflection to be a sill. Configurations in addition to saucer-shaped sill facies units are shown in Figure 5.12. The two main groups are layer parallel and saucer-shaped sill units. In addition, planar transgressive facies and fault block facies units were identified (Planke et al., 2005).

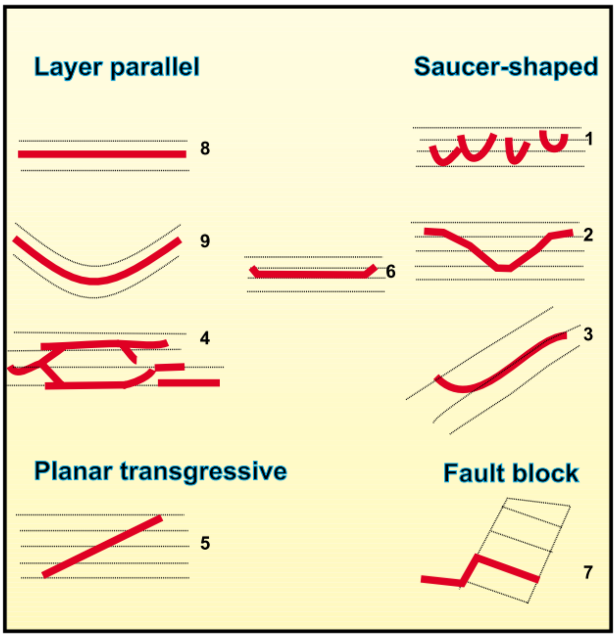

Figure 5.12: Illustrations of the configuration of sill facies units. Under the Saucer-shaped units there are 3 subgroups: shallow intrusions (1), rough saucer-shaped (2) and climbing saucer-shaped (3). Rough layer-parallel (4), Smooth layer-parallel (8) and basin parallel (9) are the subgroups for the layer-parallel units. Number 6 is the slightly saucer-shaped unit, which falls between the two main groups. In addition, planar transgressive sill units and fault block configurations exist. From Planke et al. (2005).

The sill intrusion in this study seem to fall mostly under the layer parallel-group, more specifically subgroup 4: Rough layer-parallel sill units. The sills are characterised by several layers of sills that for the most part follow the layers. As can be seen in Figure 5.11A, the different layers of sills are connected by transgressing segments.

5.4 Fluid flow expressions

Several fluid flow indicators were revealed during the interpretation of the seismic data. The fluid flow expressions appear as vertical zones of distorted reflections. In some cases amplitude anomalies such as bright spots occur in association with the fluid flow feature. The fluid flow features will be presented together with associated amplitude anomalies in the following subsections.

5.4.1 Faults as migration pathways

As discussed in chapter 2, faults make up the largest group of seal bypass systems. The abundant polygonal faults are assumed to be of particular importance for fluid flow in the study area. Polygonal faults belong to the supratrap family of faults, as defined by Cartwright et al. (2007). Supratrap faults are faults embedded within a sealing sequence. It is suggested that the dilatancy in polygonal faults occurs during active slip, and that fluids can migrate through the faults whenever there is a slip event (Cartwright et al., 2007). Indications for a fault acting as a fluid migration pathway can be e.g. bright spots occurring along the fault. This also indicates that gas is present. Fluid flow features on the seabed found in relation to faults extending up to or close to the seabed, may also indicate that the fault is acting as a fluid conduit (Ligtenberg, 2005; Løseth et al., 2009).

The seismic data revealed several indicators for faults acting as migration pathways. High amplitudes associated with faults, acoustic masking in the proximity of faults and seabed expressions were identified. The seabed expressions will however be presented later.
Bright spots associated with faults are identified in the seismic data as shown in Figure 5.11A&B. These relatively small high-amplitude anomalies are found mostly within the Kai Formation at 2000-2200 ms TWTT. Fault-related bright spots are the most common in the northern part of the survey (Figure 5.12C).

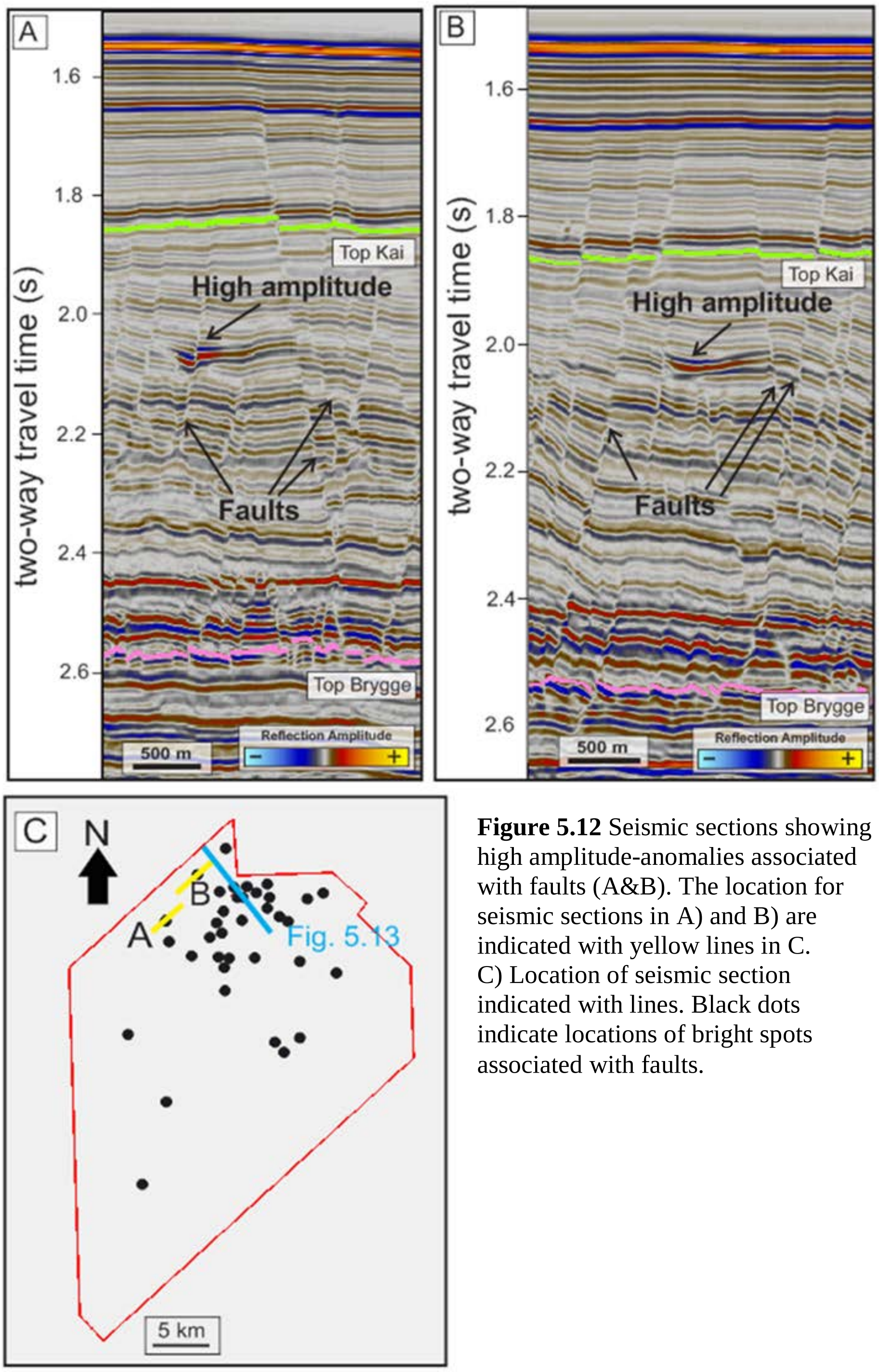

Figure 5.12 Seismic sections showing high amplitude-anomalies associated with faults (A&B). The location for seismic sections in A) and B) are indicated with yellow lines in C. C) Location of seismic section indicated with lines. Black dots indicate locations of bright spots associated with faults.

Acoustic masking and chaotic reflections associated with faults are common as well. As mentioned in chapter 2, acoustic masking are areas with low seismic reflectivity commonly caused by the presence of interstitial gas bubbles (Andreassen et al., 2007). Figure 5.13 shows mainly the Kai Formation with faults cutting through the strata. Both acoustic masking bright spots (high amplitudes) are observed in the vicinity of polygonal faults.

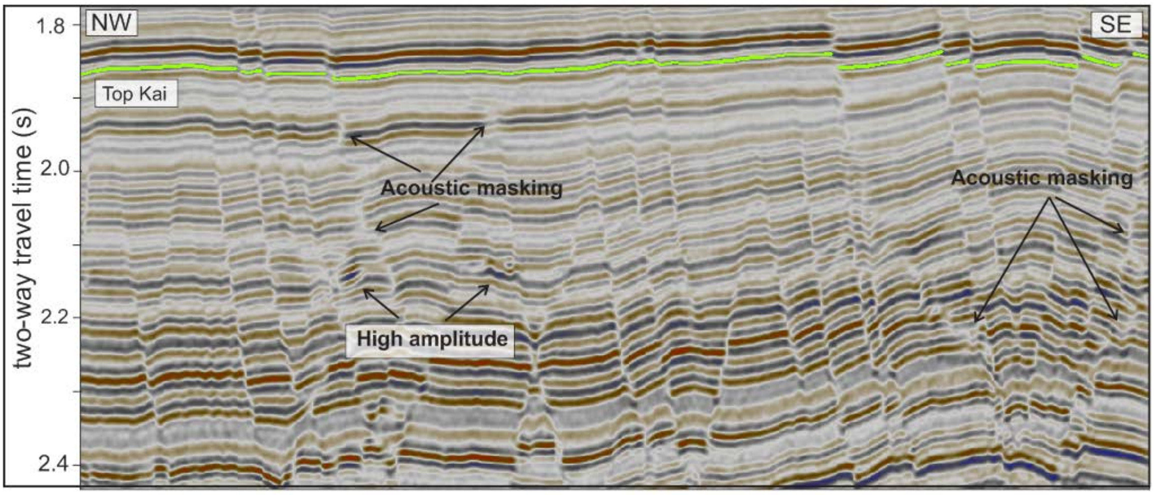

Figure 5.13: Seismic profile showing high amplitudes and acoustic masking as indicators for faults acting as fluid migration pathways. The location of the seismic profile is shown in Figure 5.12C. Note also how the amplitude of the reflection at approximately 1950 ms TWTT (Just below Top Kai) decreases when going from NW to SE.

5.4.2 Hydrothermal vents

The second major group of features indicating fluid flow, are features consisting of a pipe with acoustic masking and terminations with either an crater or up-doming (Figure 5.16). The pipes are found directly above the sill intrusions presented previously (Figure 5.11). The shape of these features and their occurrence in connection with sill intrusions lead to the interpretation of these features being hydrothermal vents, also referred to as hydrothermal pipes. Similar features have been mapped extensively in the Vøring and Møre Basins by Planke et al. (2005). Roughly 35 hydrothermal vents are observed within the study area (Figure 5.10 and Figure 5.14). In planar view the hydrothermal vents are seen as roughly circular chaotic zones. On a variance map the vents are detected as zones with high variance (red/yellow colour in Figure 5.14). The diameters of the vent tops (terminations) generally vary between 400 m to 1500m. A few vents with craters of 2500 to 4000m were observed, e.g. figure 5.16C. The vertical extent of the hydrothermal vents from sill to top, varied from 600 ms TWT to 1800 ms. The extent seems to be determined by the depth of the sill, as the sill intrusions occur in different layers of varying depths (Figure 5.11 & Figure 5.16). Radial faults are common around the terminations of hydrothermal vents, particularly those that have mounds at the top of the vent. They are common when up-doming of sediments occur. This kind of deformation can lead to new fluid flow pathways as they have an impact of seal integrity (Cartwright et al., 2007).

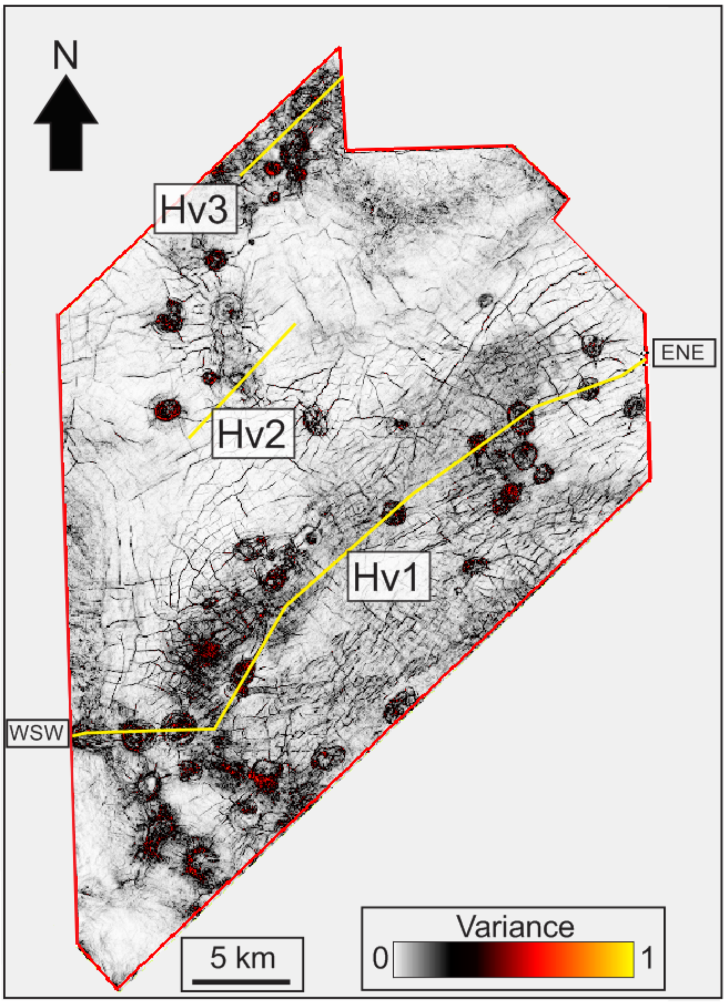

Figure 5.14: Variance time slice taken at 2950 ms TWTT showing the occurrence of hydrothermal vents. Hv1, Hv2 and Hv3 lines show the locations of seismic sections presented in Figure 5.15.

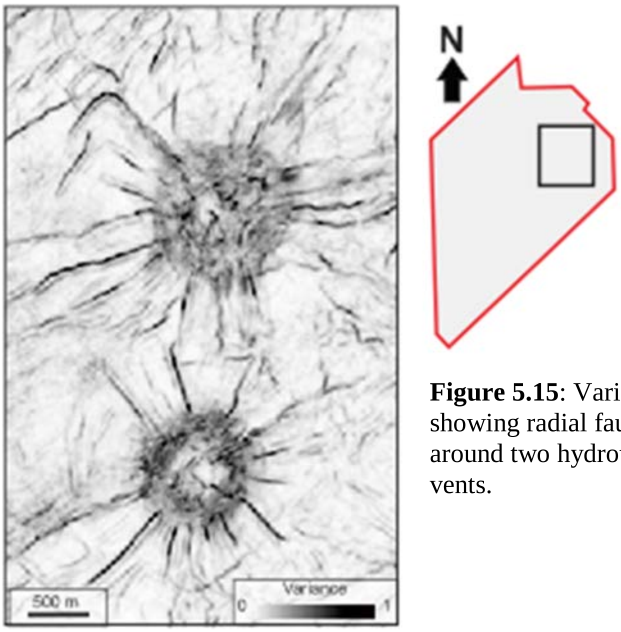

Figure 5.15: Variance map showing radial faults around two hydrothermal vents.

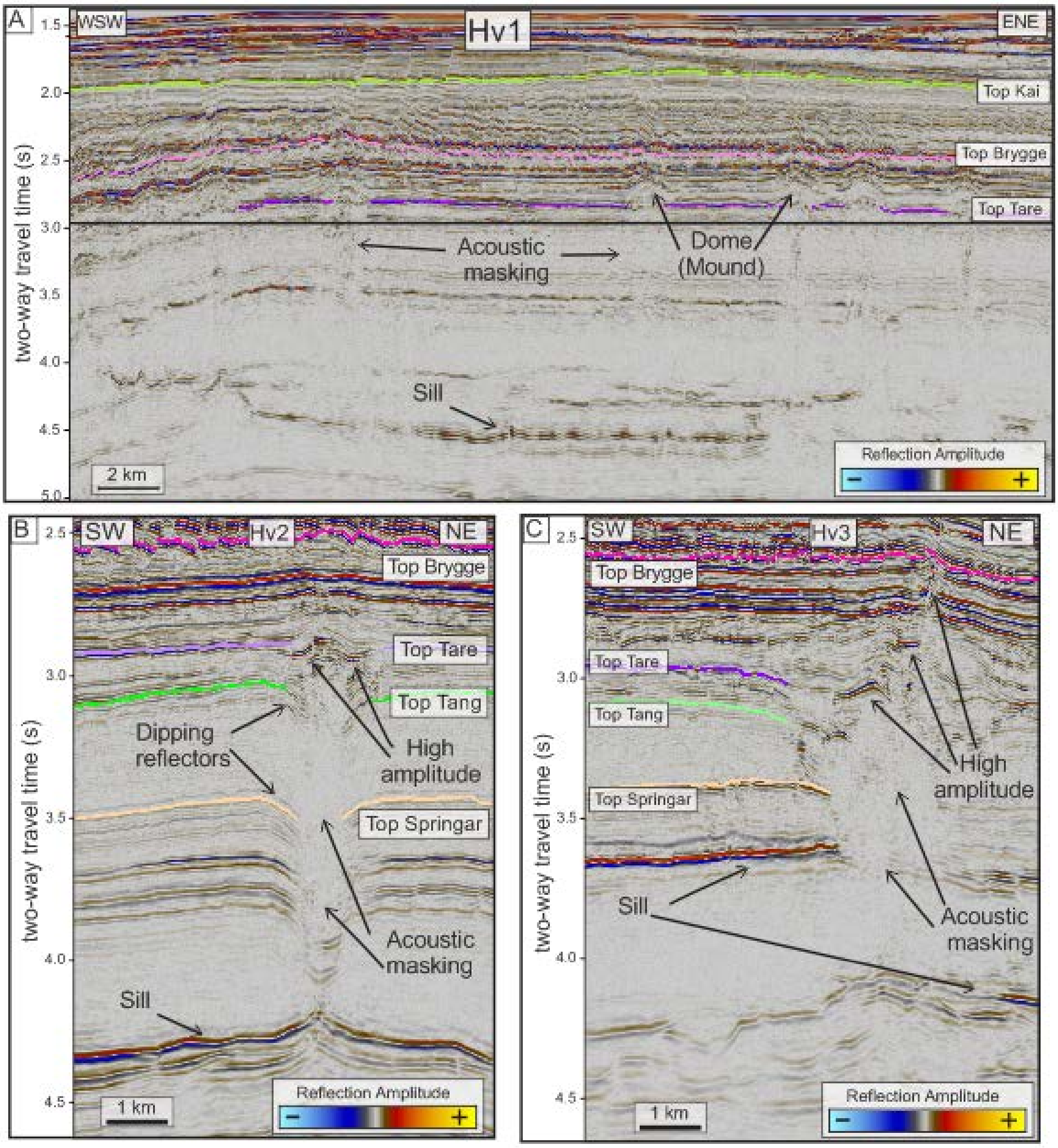

Figure 5.16: For locations of seismic sections Hv1, Hv2, Hv3 the reader is referred to Figure 5.14. A) Seismic section (Hv1) showing several hydrothermal vents. The pipes have chaotic reflections and are acoustically masked. The terminations have domes or mounds that affect the intraformational reflections within Brygge Formation. In some cases the Top Brygge horizon is affected as well.
B) Seismic section showing a hydrothermal vent where the lower part (pipe) shows acoustic masking and the top vent includes high amplitude- reflections. Some doming of the Top Tare Horizon occurs.
C) Hydrothermal vent with the largest diameter (4km) mapped in this study. The top vent shows several levels with high amplitude-reflections. For this particular vent, the Top Brygge Horizon is affected and shows some doming.

5.4.3 Pipes

Pipes are only observed in the southern part of the study area. The pipes show vertical acoustic masking starting at approximately 3.5 s below the surface going all the way up to the seafloor. In the deeper part of the section the reflections are more dimmed than disturbed (Figure 5.17). Within the Naust Formation the reflections are both acoustically masked and disturbed. Signs of pull-up and push-down of reflectors are observed. These pipes cut through a feature interpreted to be a gas hydrate-related BSR, but this will be discussed later. Examples of pipes found directly above hydrothermal vents are seen, but pipes occurring without the presence of a hydrothermal vent are identified as well.

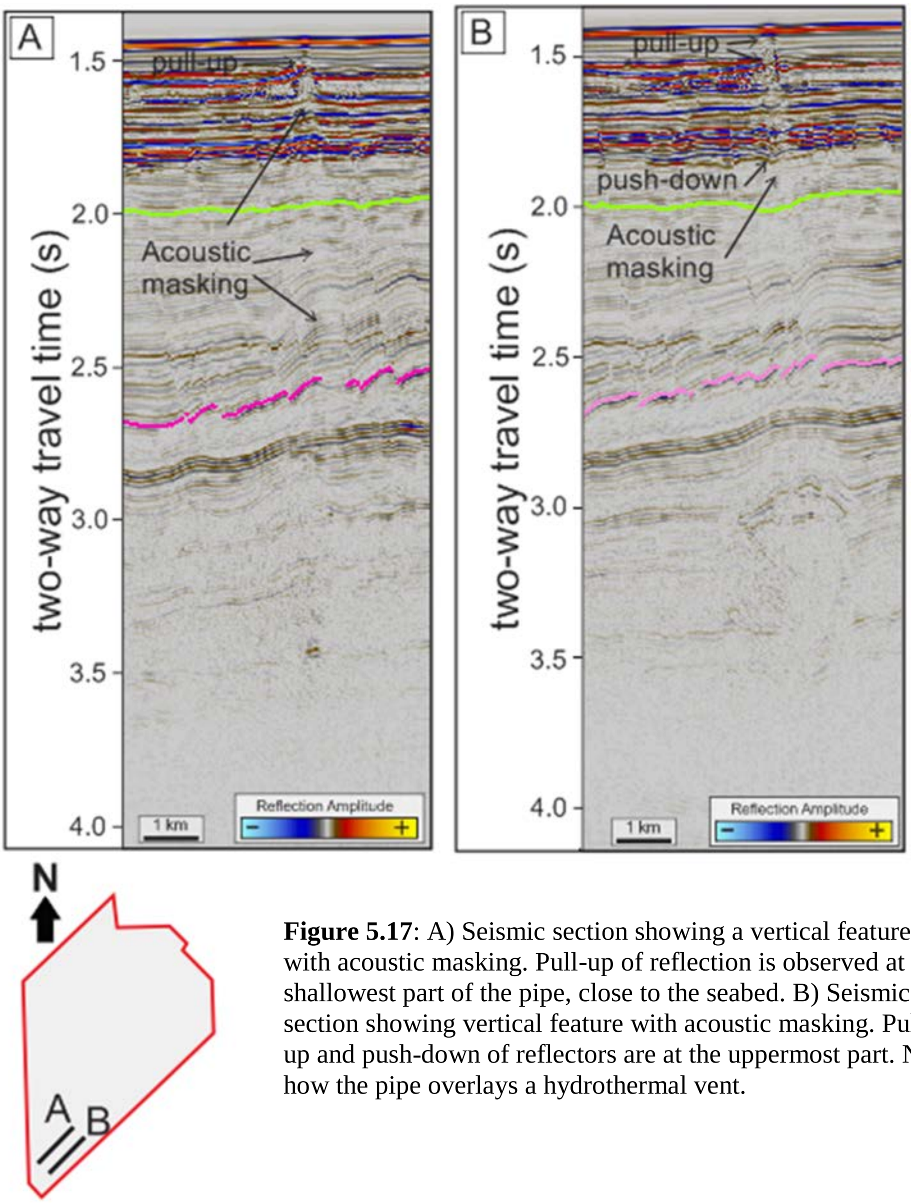

Figure 5.17: A) Seismic section showing a vertical feature with acoustic masking. Pull-up of reflection is observed at the shallowest part of the pipe, close to the seabed. B) Seismic section showing vertical feature with acoustic masking. Pull-up and push-down of reflectors are at the uppermost part. Note how the pipe overlays a hydrothermal vent.

5.4.4 Seabed expressions

The study area shows very few seabed expressions of fluid flow. Seabed expressions such as pockmarks have however been reported at Nyegga (Westbrook et al., 2008) (Hjelstuen et al., 2010; Hustoft, Dugan, & Mienert, 2009; Plaza-Faverola et al., 2010). Seabed expression 1 has a diameter of 230 m, while seabed expression 2 has a diameter of 345 m. Because of the character of the seabed reflection, more details cannot be acquired. The pipes shown in Figure 5.18C are the same pipes as shown in Figure 5.17A&B. Note how the BSR is deflected upward directly within the pipe. This behavior suggests a localised heatflow anomaly. This can be explained by warm fluids ascending through the hydrothermal vents (Gay, Lopez, Berndt, & Seranne, 2007; Pecher et al., 2010).

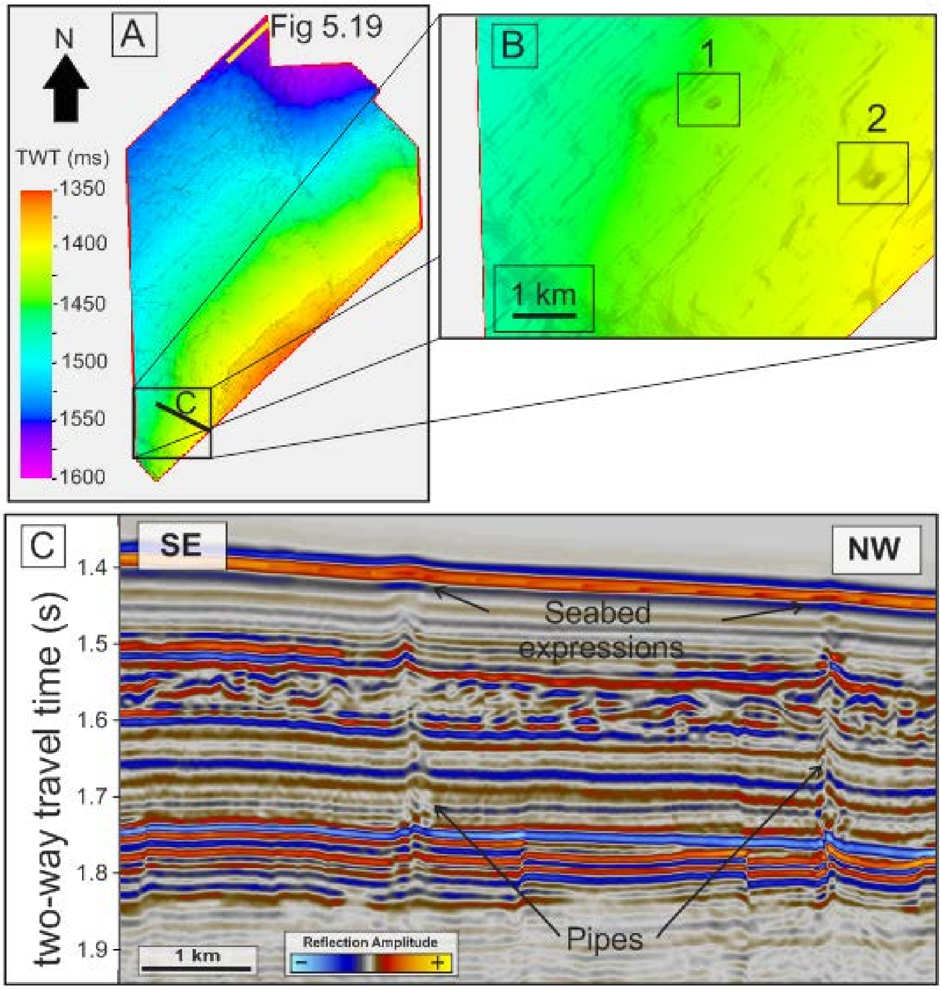

Figure 5.18: A) Time-structure map of seafloor with 20x vertical exaggeration. B) Close-up of seafloor revealing 2 fluid flow expressions.
C) Seismic line crossing the two seabed expressions shown in B. The location of the seismic profile is shown as the black line in A).

Weak seabed expressions are found in abundance above polygonal faults terminating close to the seabed (Figure 5.19). These expressions are however not visible on the time-structure map of the seabed. Because of the fluid flow indicators (acoustic masking and bright spots) identified together with polygonal faults in this area, these seabed expressions are interpreted to be expression of fluid flow.

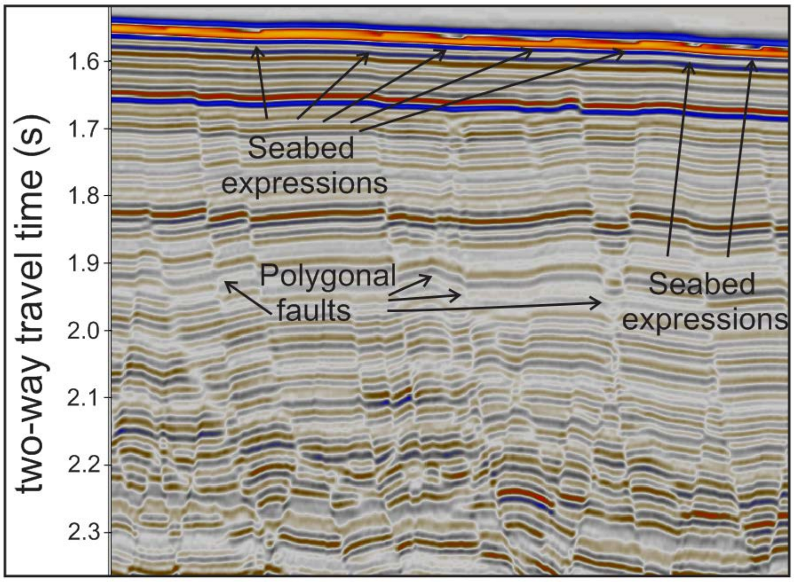

Figure 5.19: Seismic sections showing polygonal faults terminating close to the seabed. Weak expressions can be seen on the seabed. The location of this seismic profile is indicated by the yellow line in Figure 5.18.

5.5 Depositional features

Numerous high amplitude anomalies are found within the Naust Formation. These anomalies are frequently located beneath disturbed reflections interpreted to be mass-transport deposits. These mass-transport deposits can be interbedded glacigenic debris flow deposits, which are common on the mid-Norwegian continental margin (Berndt et al., 2004; Bünz & Mienert, 2004; Chand et al., 2011; Hjelstuen et al., 2005). These deposits can be identified on variance maps (Figure 5.20A,B). The flow direction is taken to be from SE to NW, approximately the same as the seafloor relief. The associated high amplitudes are found at different levels within the Naust Formation. RMS-amplitude maps can be used to reveal the high-amplitude anomalies (Figure 5.21), but interpretation has to be done with care as many of these high amplitudes might result from tuning-effects when the deposit thins out (tuning thickness).

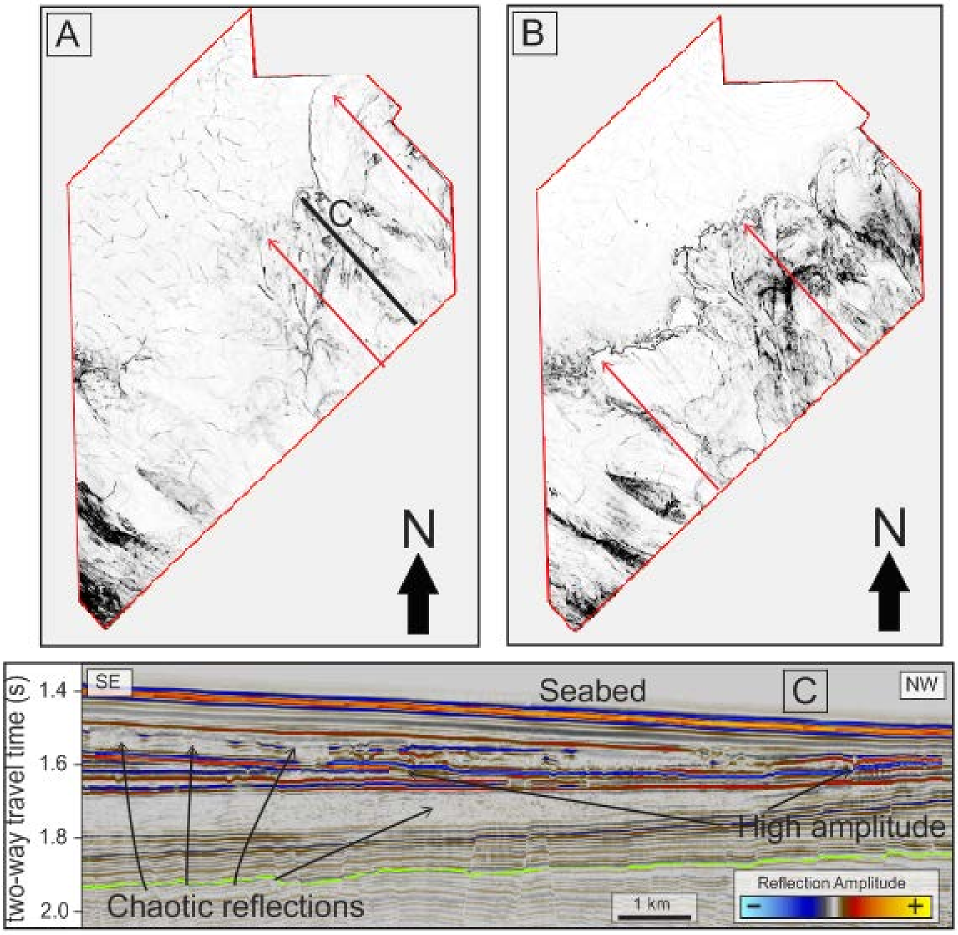

Figure 5.20: A) Variance time slice at 1612 ms TWTT. Red arrows indicate direction of mass transport. Black line indicates the location of seismic sections shown in C).
B) Variance time slice at 1576 ms TWTT. Red arrows indicate direction of mass transport.
C) Seismic section showing mass-transport deposits (Chaotic reflections) and high amplitudes. Note how the polygonal faults reach the deposits.

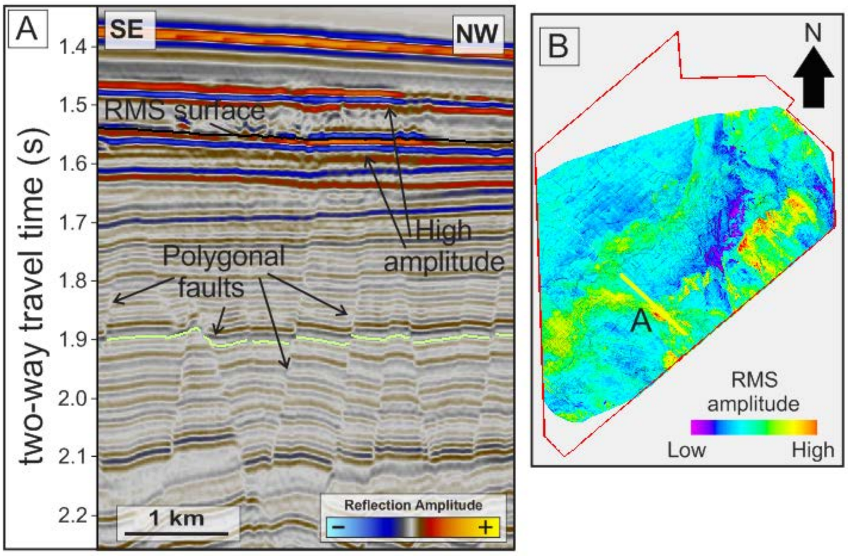

Figure 5.21: A) Seismic section showing high amplitude-reflections interbedded in mass-transport deposits. B) RMS map created over RMS surface in A with 100ms window.

5.6 Gas hydrates

This section will present seismic data inferring the presence of gas hydrates. The results from hydrate stability-modelling will also be explained and presented.

5.6.1 Seismic character of the BSR

In the 3D seismic data set high amplitude-reflections terminating abruptly are identified. The enhanced reflections terminate against a horizon that is crosscutting the sedimentary strata at a low angle (Figure 5.22). This crosscutting horizon mimics the seafloor and has a polarity opposite to the seabed-reflection (Figure 5.22A). This behavior is interpreted to arise from a BSR, a bottom-simulating reflector. Because the BSR appears at ~350 ms TWTT it is believed to result from the presence of gas hydrates.

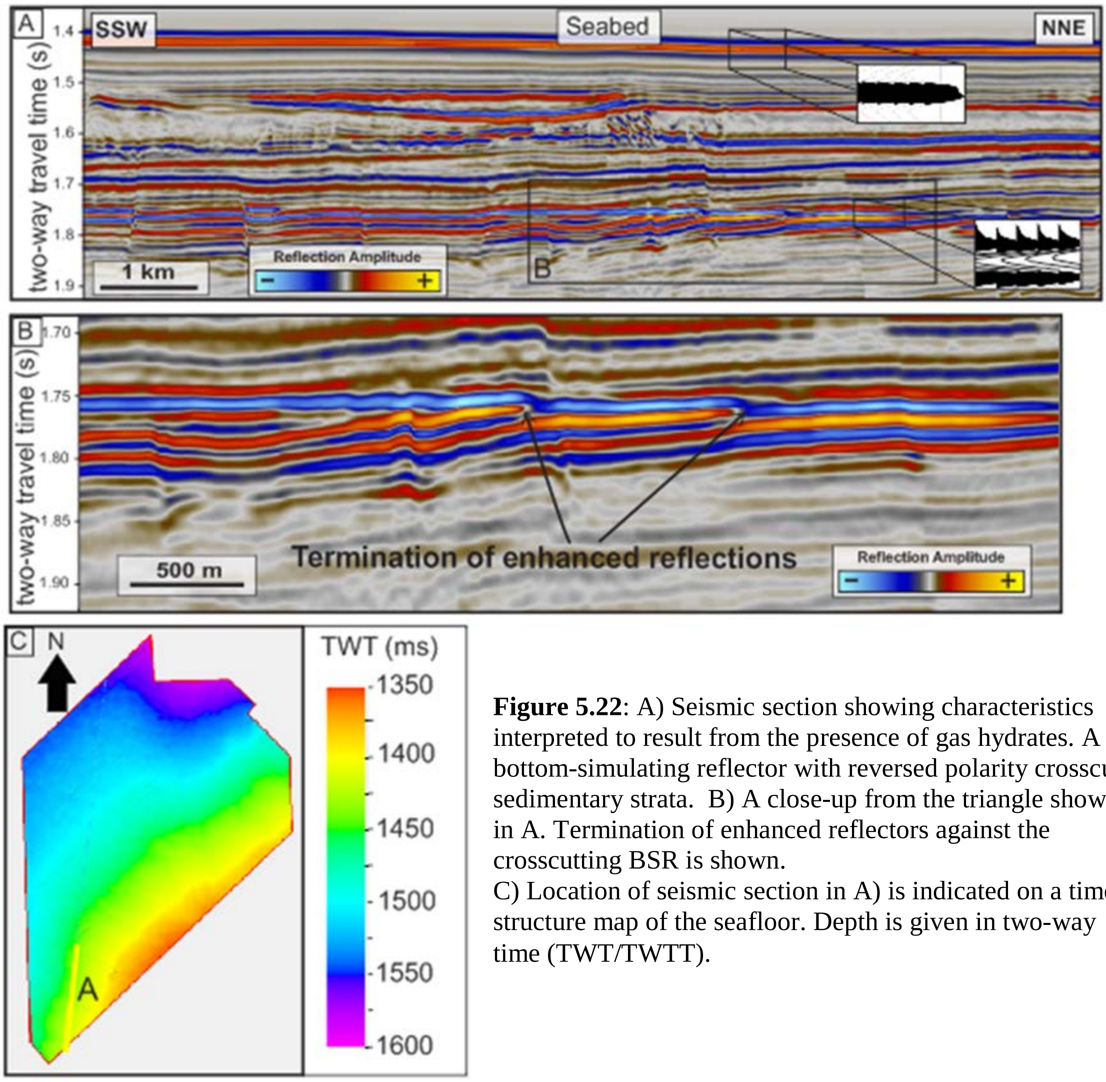

Figure 5.22: A) Seismic section showing characteristics interpreted to result from the presence of gas hydrates. A bottom-simulating reflector with reversed polarity crosscuts sedimentary strata. B) A close-up from the triangle shown in A. Termination of enhanced reflectors against the crosscutting BSR is shown.
C) Location of seismic section in A) is indicated on a time-structure map of the seafloor. Depth is given in two-way time (TWT/TWTT).

The BSR commonly marks the transition from gas hydrates in the sediments, to free gas sitting beneath the gas hydrates. The opposite polarity indicates a negative reflection coefficient, which is an expected response from trapped gas. Since the BSR marks the transition from gas hydrate to free gas, it also indicates the base of the gas hydrate stability zone (BGHSZ). The BSR is only observed in the southernmost part of the survey. 2D seismic data allowed the BSR to be mapped outside the 3D survey. Figure 5.23 shows the depth to the BSR given in ms two-way time below the sea surface.

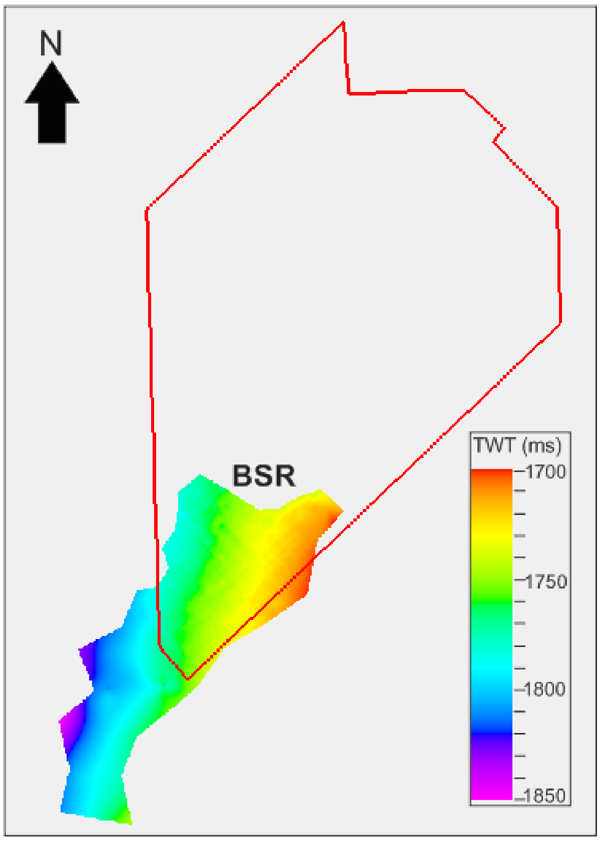

Figure 5.23: Distribution of the BSR. Depth is given in two-way time.

5.6.2 Hydrate stability zone and BGHSZ

As mentioned in chapter 4, the CSMHYD program was used to model the hydrate stability zone (or hydrate equilibrium). There are no CTD (conductivity, temperature, and depth) stations in this study area, so there are no scientific data for bottom water temperatures. There are however CTD reading were however acquired by the Storegga Slide, roughly 270 km from the 3D survey used in this study. Mienert et al. (2005) found bottom water temperatures of around -1°C at 950 m depth. The bottom water temperatures from these readings are used in the modelling of the hydrate stability zone.

The water depth within the 3D survey is found using the two-way time to the seafloor, and lies between 1010m and 1200m. Thus -1°C is used. The geothermal gradient is estimated from the subsurface temperatures measured in the conventional boreholes presented in chapter 4. The geothermal gradient is estimated to be 51°C/km. Using these estimates and a salt water concentration of 3,5%, the conditions for hydrate-stability were calculated. The results are shown in Figure 5.24. The CSMHYD software calculates equilibrium pressures for given temperatures with the presence of inhibitors (here average salt water). The pressures are converted to depth using the equation for hydrostatic pressure in chapter 2, the water depth within the survey, average salt water density of 1024 kg/m^3 and sediment densities from well 6605/8-1. This is the only well with density readings for shallow depths, depths where the gas hydrates are inferred to be. For this well, the density readings start at 970 m, almost right at the seafloor. For location of the well, see Figure 4.2.

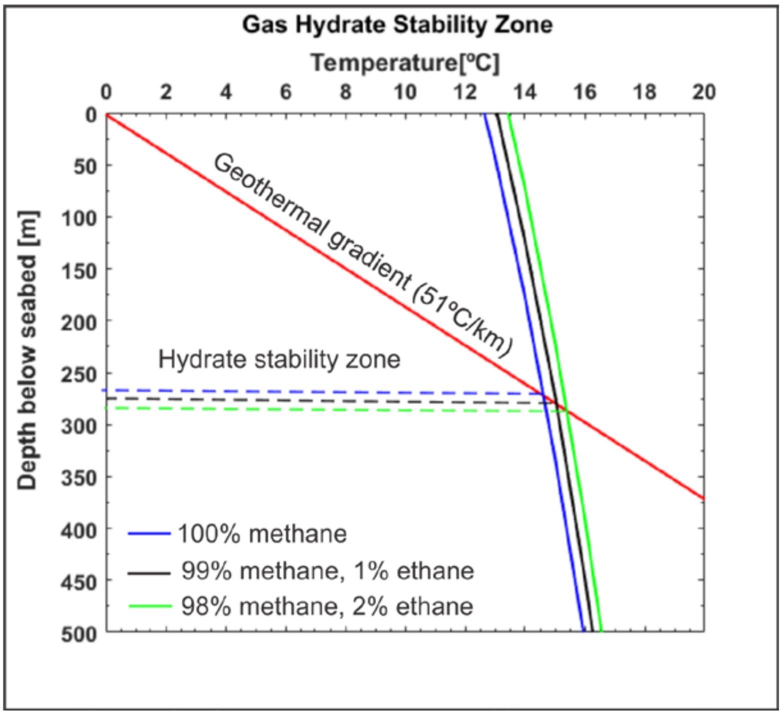

Figure 5.24: Diagram showing the modelled gas hydrate stability zone. Gas hydrates are stable above the stippled lines, that is, above the point where the geothermal gradient meets the hydrate stability curves. The hydrate stability curves are

The hydrate stability curves were modelled for three different gas compositions. The blue curve is the stability curve for pure methane, the black curve for 99% methane together with 1% ethane and finally the green curve for 98% methane with 2% ethane. Because methane generally makes up so much of natural gas, the green curve is considered to be the least likely one. Using the hydrate stability-depth found in Figure 5.24, the hydrate stability-curves were generated for the seismic data. The seabed reflection was shifted down the amount of time corresponding to the depths for the stippled lines in Figure 5.24. The hydrate stability-curves show the BGHSZ. The result can be seen in Figure 5.25.

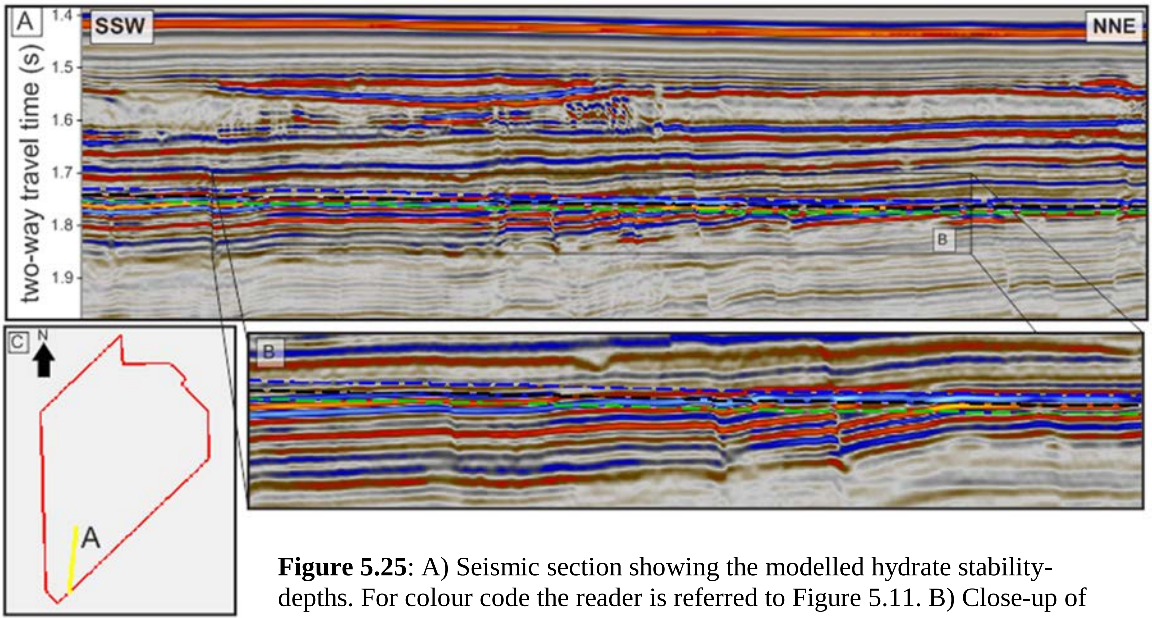

Figure 5.25: A) Seismic section showing the modelled hydrate stability-depths. For colour code the reader is referred to Figure 5.11. B) Close-up of the BSR in A). C) Survey outline. Yellow line indicates the location of seismic section shown in A).

As can be seen in Figure 5.25, the BSR does not follow any of the lines exactly. The BSR seems to lay between the stability-line for 100% methane (blue) and the line for 99% methane with 1% ethane (black).

6 Discussion

The previous chapter presented results obtained from the 3D seismic data set ST0827 supplemented by 2D seismic data set FFC95 and welldata. The stratigraphy, faults, volcanic intrusions, fluid flow expressions with associated amplitude anomalies, depositional features and BSR were presented. The focus of the discussion chapter is to further investigate the fluid migration and accumulation to get a better understanding of the controlling mechanisms behind their occurrence and behaviour. Focus is also directed to understanding the origin of the BSR and its connection to fluid migration. The geological controls of the BSR appearance will also be discussed.

6.1 Fluid migration and accumulation

As presented in chapter 5, fluid migration features are common within the study area. The most abundant pathways are polygonal faults and hydrothermal vents. Pipes and chimneys however, are perhaps not as common as expected.

6.1.1 Controlling mechanisms for fluid flow

The fine-grained sediments of Kai and Brygge Formations make up excellent hosts for the formation of polygonal faults. Polygonal faults are formed through dewatering of fine-grained sediments. Fluid is expelled as the sediments contract. Polygonal faults form as a response to syneresis of colloidal sediments and as a response to compaction due to gravitational loading (Cartwright et al., 2003; Cartwright & Dewhurst, 1998). Once the faults are created, they may act as fluid conduits. Cartwright et al. (2007) proposed that fluid migration will most likely happen when there is movement, this due to the increased dilatancy of faults during slip events. The observed slide events or debris flows give a sudden sediment loading. This can reactivate the underlying polygonal faults, allowing fluids to migrate through.

During the development of polygonal fault systems, significant amounts of fluids are expelled (up to 60 %). With these amounts, polygonal faults systems will act as major sources for fluid flow in a region. During and after reactivation, polygonal faults can act as pathways for fluids ascending from greater depths (Berndt et al., 2003; Hustoft et al., 2007). There are roughly 35 hydrothermal vents indicating that fluids have indeed migrated from depths beneath the polygonal faults. With reactivation of faults due to sudden sediment loading caused by debris flows, it seems reasonable to assume that the polygonal faults allow the fluids from the hydrothermal vents to migrate. The amplitude anomalies found in relation with polygonal faults suggest that migration has occurred along the faults. The combination of hydrothermal vents and polygonal faults can thus be important for both the regional fluid flow as well as local fluid migration. For the case where the polygonal faults within the Kai Formation have deformed and fractured the overlying Naust Formation sediments, fluids may migrate through fracture zones all the way to the seabed. Figure 6.1 shows a seismic section where both hydrothermal vents and polygonal faults are present. High amplitude anomalies and acoustic masking are identified. The polygonal faults seem to affect sediments all the way to the seafloor.

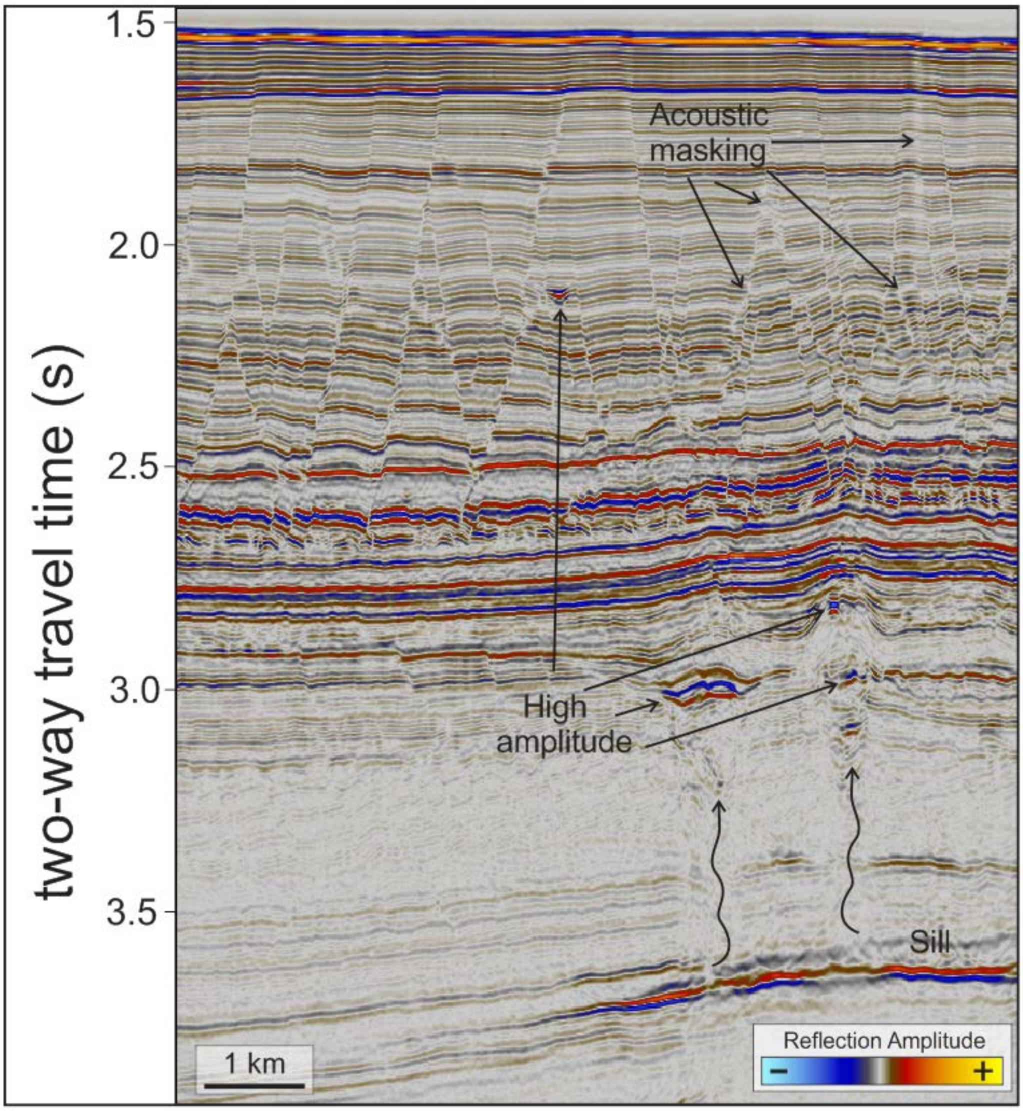

Figure 6.1: Seismic section showing two hydrothermal vents. High amplitude anomalies are observed both in and above the hydrothermal vents. Polygonal faults are located above the hydrothermal vents. The faults affect the sediments all the way to the seabed. Acoustic masking is seen as both sub-vertical and vertical zones. A bright spot at roughly 2.2 s TWT is detected in proximity of the polygonal faults

This combination of fluid flow through hydrothermal vents and polygonal faults appears to be a relatively common system of fluid flow within the study area. This is frequently observed together with high amplitude reflections in the strata adjacent to the faults. A schematic model is therefore proposed for fluid flow controlled by hydrothermal vents and polygonal faults (Figure 6.2). The high amplitude anomalies stem from a p-wave velocity reduction due to the presence of gas. Permeable layers capped by impermeable layers within the Kai Formation are proposed as traps. The schematic model in Figure 6.2 presents a fluid migration model for the areas where debris flow deposits are absent. Based on the observations where the seabed was deformed by underlying faults (Figure 5.19), the fractured zone in the model has been taken to the seabed. The white dots represent migrating gas. The gas starts the migration by the sill intrusions, then migrating upwards and creating hydrothermal vents. The sediments above the mound are fractured from the forced folding, and fluid migrates through. When migration occurs along the polygonal faults, some gas migrates laterally into adjacent strata. If the gas gets trapped, high amplitudes occur due to the negative reflection coefficient caused by the presence of gas.

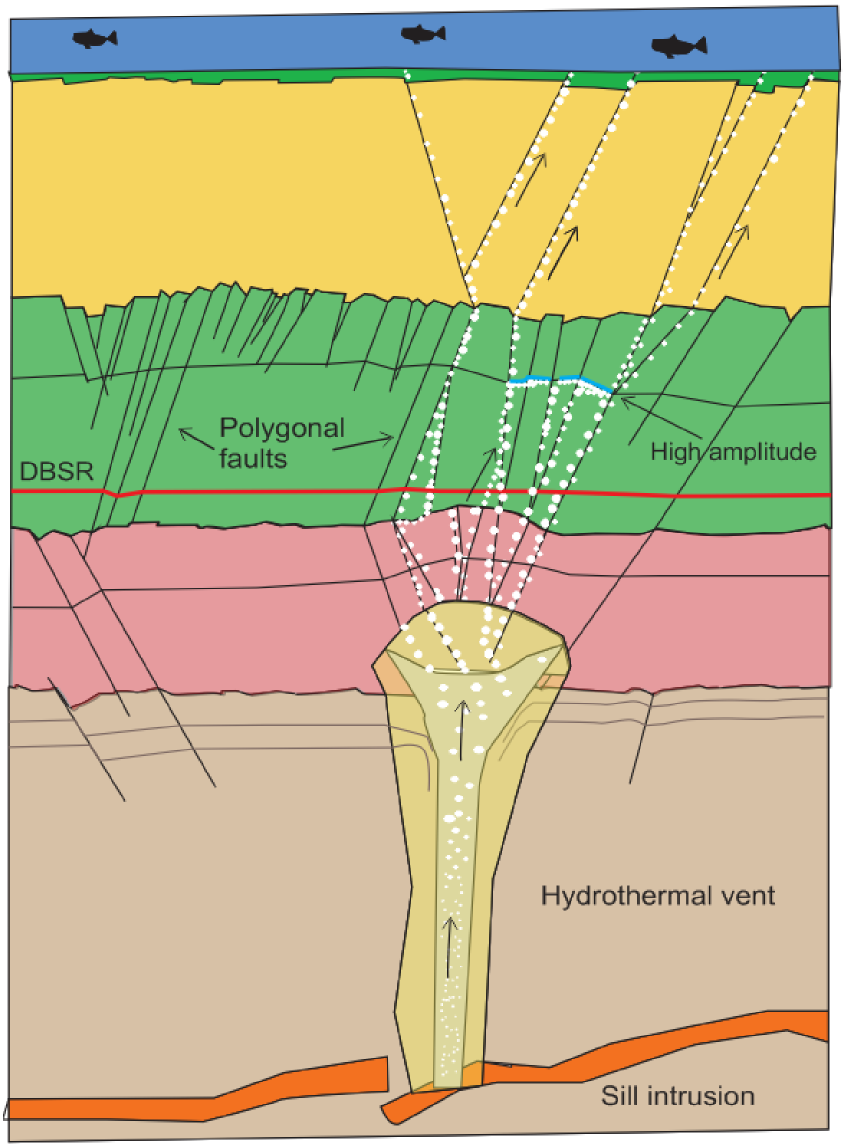

Figure 6.2: Schematic model of fluid flow starting by hydrothermal venting, continuing to fault related migration where gas may get trapped in permeable layers capped by impermeable layer. Some of the gas continues migrating upwards through fracture zones created by the underlying polygonal faults.

Acoustic pipe structures have also been identified in the study area, commonly in relation with hydrothermal vents and in areas where gas hydrates are inferred through the identification of a BSR. As discussed in chapter 2, gas hydrates are sensitive to pressure and temperature changes. One possible explanation for this behaviour is that warm fluids have migrated through the hydrothermal vents, been focussed upwards through polygonal faults and then dissociated the gas hydrate. The gas from the gas hydrate then escapes, leaving acoustic pipes as in Figure 5.17 and Figure 5.18.

A schematic model is presented in Figure 6.3 for the fluid flow controlled by hydrothermal vents, polygonal faults and migration through pipes cutting the gas hydrate-related BSR. In this model debris flow deposits are present. Pipes extending from polygonal fault-terminations allow gas to get trapped in interbedded layers of the debris flow deposits. This model proposes that warm fluids flow up through the hydrothermal vent, further along polygonal faults up to the BSR where the warm fluids then affect the hydrate stability. The temperature increases and the hydrate starts to dissociate. If enough of the gas hydrates in the sediments decomposes, fluids (including the gas from the hydrates) may flow up to through the seabed and create seabed fluid flow expressions.

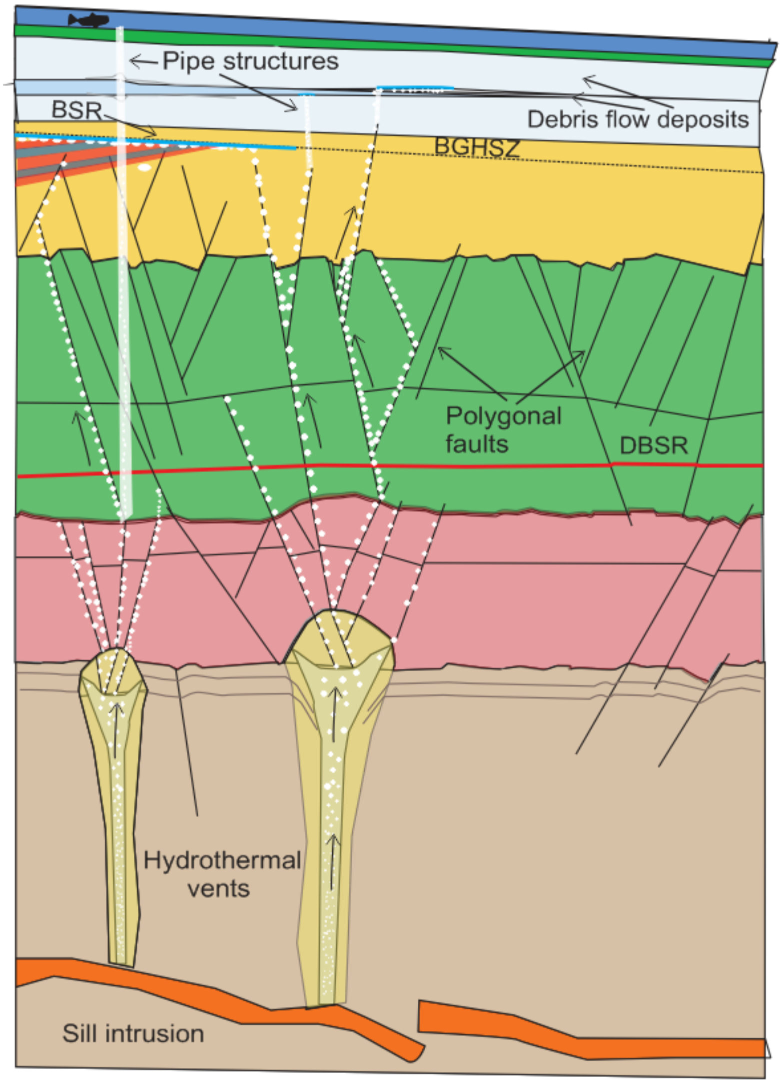

Figure 6.3: Schematic model of fluid flow through hydrothermal vents and polygonal faults. An acoustic pipe extending from the top of a hydrothermal vent cuts through the gas hydrate-related BSR and reaches the seabed. Enhanced reflections terminate against the BGHSZ, given by the BSR. Pipe structures also extend from the terminations of polygonal faults up to impermeable debris flow deposits that allow the entrapment of gas. The gas accumulations give high amplitude anomalies.

6.1.2 Fluid accumulation mechanisms

Some of the accumulation mechanisms have already been mentioned. Gas may accumulate below the gas hydrate as seen in Figure 6.3, or it may accumulate below glacigenic debris flow deposits. Reworked sediments tend to have lower porosities and permeabilities due to their unsorted grain distribution. In many areas within the Vøring Basin, glacigenic debris prevents the formation of pockmarks (Chand et al., 2011). A schematic model for this accumulation mechanism is presented in Figure 6.4. Naust Formation is not faulted, but deformation and acoustic masking occurs above zones with extensive polygonal faulting.

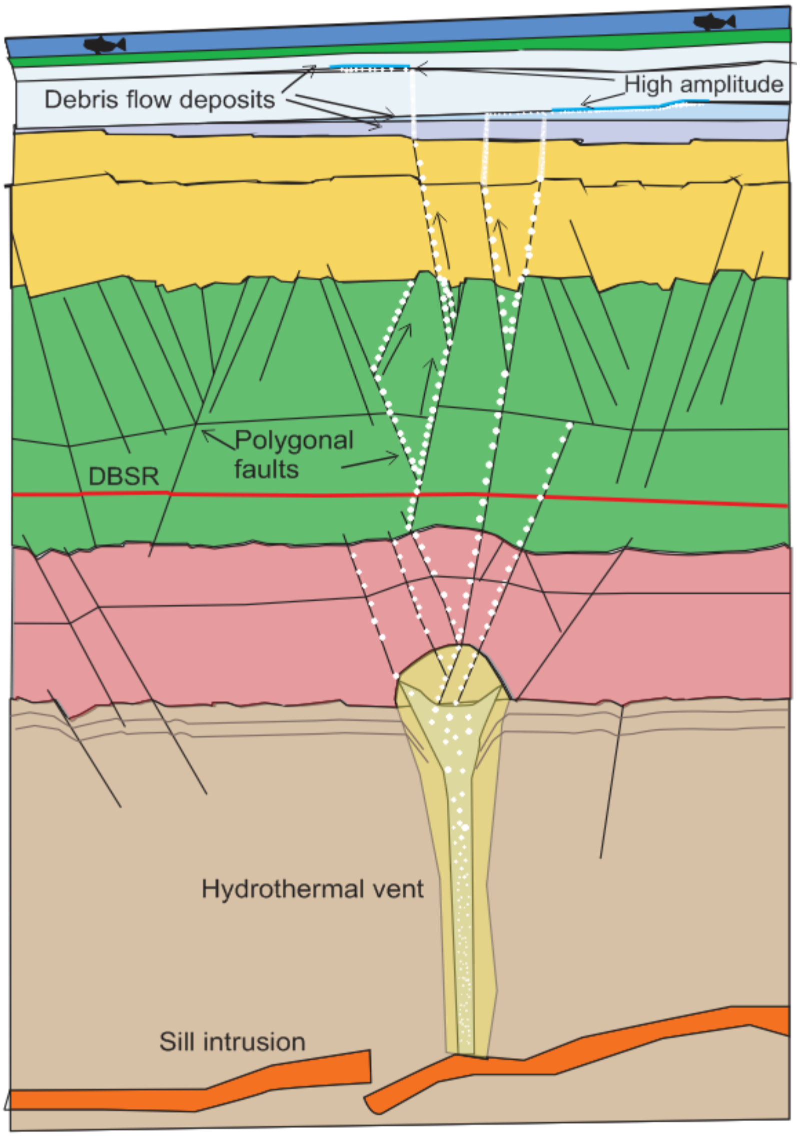

Figure 6.4: Schematic model of fluid flow starting from a hydrothermal vent, getting focussed by polygonal faults then continuing upwards through pipes until entrapment by interbedded glacigenic debris flow deposits. The accumulated gas gives high amplitude anomalies in seismic data.

6.2 Gas hydrate

In this section the BSR appearance will be discussed in terms of its lateral extent and frequency distribution. The relation between fluid flow features and gas hydrate will be discussed.

6.2.1 Lateral extent

The gas hydrate-related BSR could only be mapped in the southernmost part of the study area. It was mapped further south using 2D data (Figure 5.23). The extent of the BSR is shown in Figure 6.5. The blue, stippled line is the estimated BGHSZ with pure methante. In chapter 2, the prerequisites for hydrate formation and hydrate stability were outlined. For hydrates to form the ambient pressure and temperature conditions need to be right. Hydrate formation also requires the presence of water, hydrate forming gas, and the absence of inhibitors. Figure 6.6 shows the outline of the BSR together with a variance map. Note the amount of hydrothermal vents that terminate within the BSR-outline. The fact that several hydrothermal vents terminate in the vicinity of the BSR boundary, suggests that the hydrothermal vents alone are not a controlling mechanism for the lateral extent of the BSR. The lateral extent of the BSR can be controlled by the polygonal faults. If the polygonal faults are inhibiting the flow hydrate forming gas, gas hydrates may not form. The lateral extent can also be determined by the amount of free gas, better yet, the amount of gas available to create the BSR reflection arising from the transition between gas hydrate and free gas. As mentioned in chapter 2, the occurrence of a BSR is determined by the presence of free gas trapped underneath the hydrate. Pipes structures cutting through the BSR have been observed. The pipes also show indications of fluid migrating from the BSR. The fact that these pipes cut through the BSR might lead to leakage of the free gas trapped beneath the hydrate, reducing the volume.

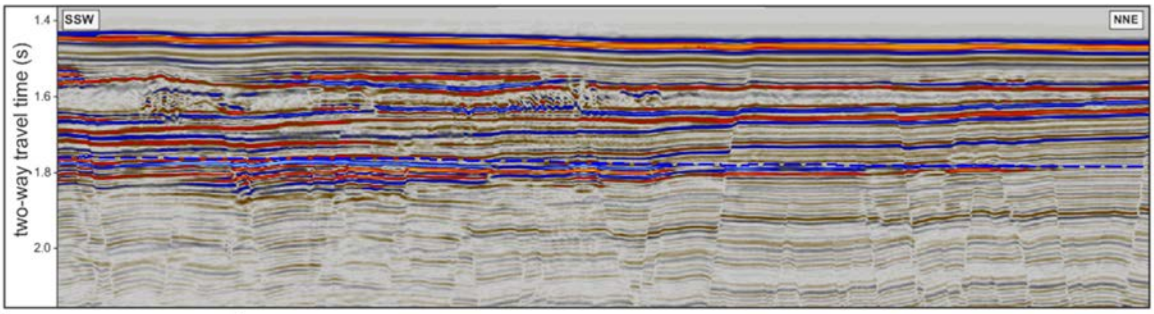

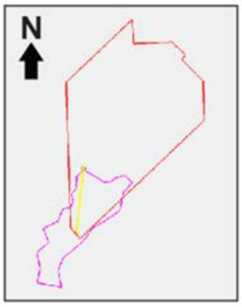

Figure 6.5: Seismic section showing the extent of the gas hydrate. Map indicates the location of the seismic section. The pink line indicates the extent of the BSR.

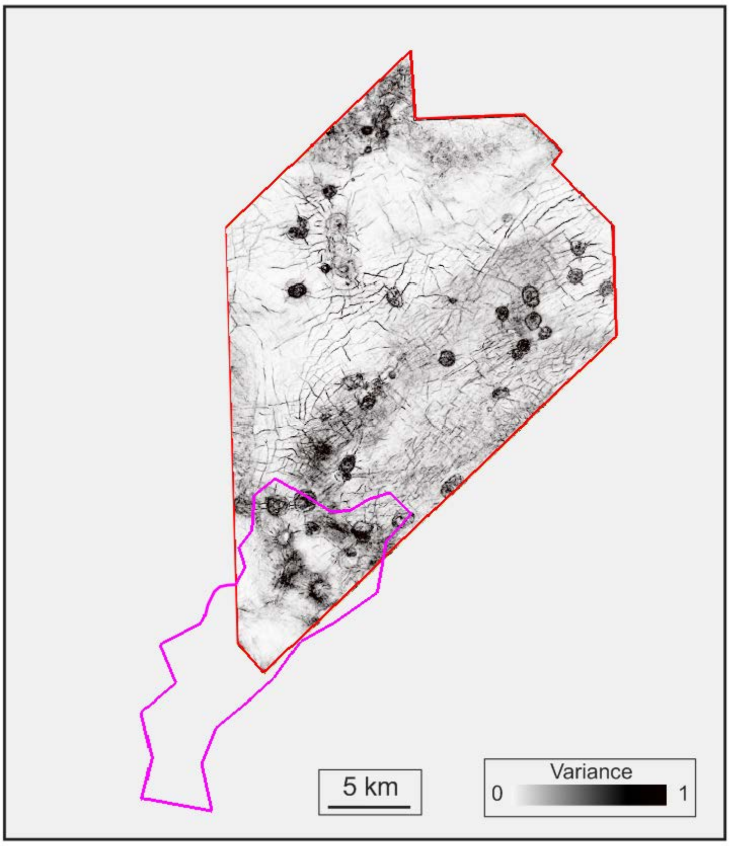

Figure 6.6: Variance map showing hydrothermal vents in planar view. The pink polygon shows the BSR extent. Note how several of the hydrothermal vents are within the BSR boundary.

6.2.2 Frequency distribution

A common characteristic of the BSR is that the frequencies vary across the BSR. The frequencies are often significantly lower in the free gas zone beneath the BSR than that of the gas hydrates in the sediments. Figure 6.7 shows an example of the frequency distribution across the BGHSZ. The expected behavior is that the zone with low frequencies follows the BSR (Berndt et al., 2004; Hustoft et al., 2007). The frequency of the BSR from this study does not show the same characteristics. An instantaneous frequency attribute is generated for the seismic data. The result is shown in Figure 6.8.

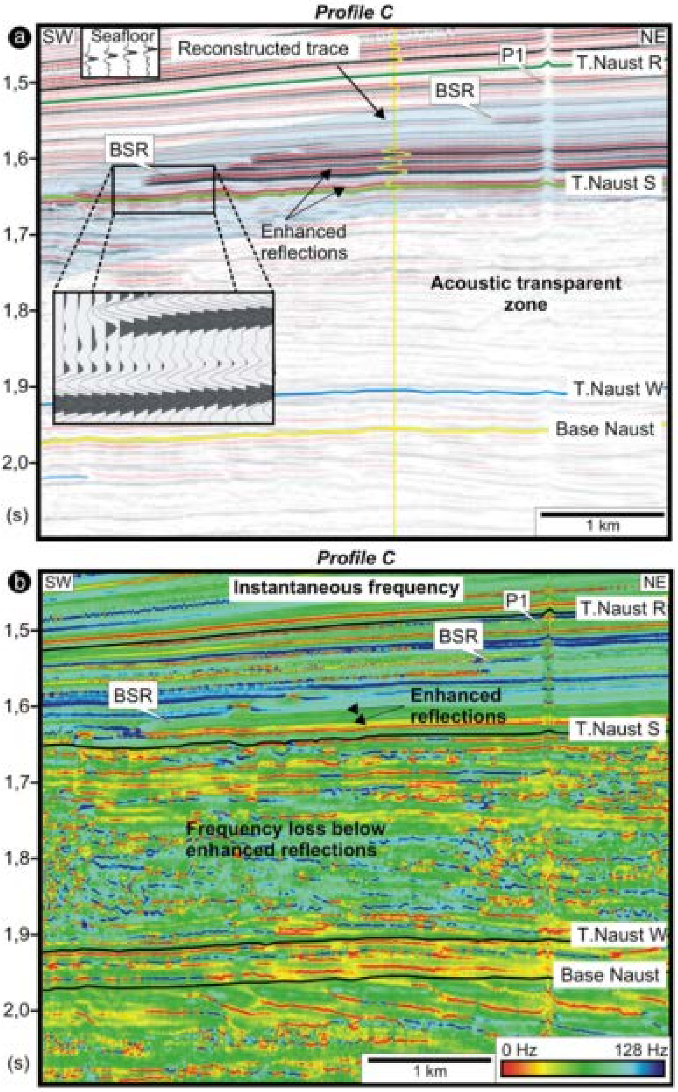

Figure 6.7: a) Seismic section showing a BSR from the mid-Norwegian continental margin. Several BSR characteristics occur, such as termination of enhanced reflections and reversed polarity. b) Instantaneous frequency attribute generated for the seismic section. Note have the frequencies are lower below the enhanced reflections. From Hustoft et al. (2007).

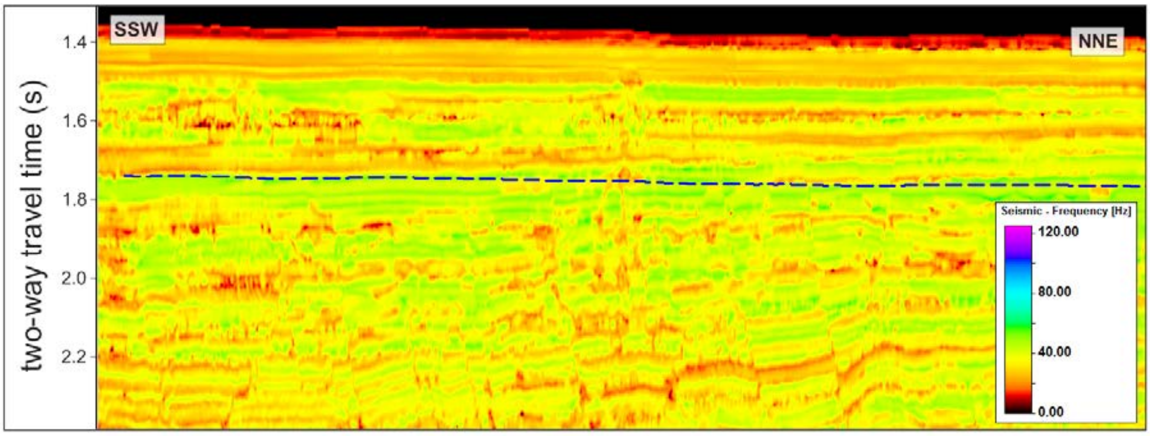

Figure 6.8: Instantaneous frequency generated for the seismic section shown in Figure 6.5.

A possible explanation for the absence of frequency loss beneath the BSR is that there might be little free gas present. This can again be a result of the pipe structures cutting through the BSR.

6.2.3 Fluid flow features and gas hydrate origin

Two models for BSR formation are suggested. The first model consists of a theory that a constant supply of gas from directly beneath the BGHSZ is required for gas hydrate formation(Bünz et al., 2003; Haacke et al., 2007; Pecher, Kukowski, Huebscher, Greinert, & Bialas, 2001). Beneath the gas-hydrate related BSR in the study area both hydrothermal vents and polygonal faults occur (Figure 6.6). Because of the presence of sill intrusions and hydrothermal vents, it seems reasonably to assume a flux of thermogenic gases from beneath.. There is a strong correlation between fluid flow (gas flux) and hydrate formation (Pecher et al., 2001). Biogenic gases can however also be generated and migrated up to the BSR. Chand et al. (2011) argued that the biogenic zone in the area extends to depths deeper than the Kai Formation. Thus a biogenic methane flux from the Kai Formation is possible. The BSR reflection appeared to be between the BGHSZ for 100% methane, and that of 99% methane and 1|% ethane. The origin of the hydrate-forming gases may explain this behaviour.
On the contrary, advective heatflow may cause a local upwarming at the base of the gas hydrate stability zone, leading to gas hydrate dissociation (Pecher et al., 2010).

The second model for hydrate formation is one that suggest recycling of gases due to either tectonic uplift or high sedimentation. Both will result in the BGHSZ shifting to a shallower level. This will result in dissociation of the present gas hydrates. The free gas will then migrate up to the new BGHSZ. The study area has not been uplifted since Neogene times, thus the uplift theory is not likely for this study area. The area has been subject to glacigenic deposition after Late Pliocene-Pleistocene. The sedimentation rates and thicknesses are however not believed to be thick enough to shift the BGHSZ, thus recycling of methane is not a likely mechanism for gas hydrate formation in the study area (Bünz et al., 2003).

The controlling mechanisms for the gas hydrate formation in the study area are therefore concluded to be a combination between hydrothermal vents and polygonal faults. The formation is dependent on a flux of either thermogenic gases from greater depths, and/or biogenic methane derived from the Kai Formation. Geochemical studies for the specific area need to be carried out for an exact conclusion of the hydrate-forming gas.

7 Conclusions

The 3D seismic survey ST0827 in the outer Vøring Basin reveals a complex fluid flow system consisting of hydrothermal vents, polygonal faults and acoustic pipes. The hydrothermal vents extend from sill intrusions at 3.8 to 5.5s TWT to the Brygge Formation. The top vents terminate either as craters, or up-doming mounds. For the latter case, the up-doming manner results in radial, concentric faults impacting the seal integrity.

The top of the fine-grained Brygge Formation is characterized by polygonal faulting. The polygonal faults continue through the ooze-dominated Kai Formation. The Kai formation is overlain the Naust Formation, in which glacigenic debris flow units are observed. As polygonal faults can be sensitive to movement, the rapid loading from the debris flows is assumed to have reactivated polygonal faults in the area, thus allowing fluid to flow through the faults. Fluid flow indicators such as bright spots and acoustic masking in the proximity of the faults imply that fluid flow along faults has occurred. Fluid flow through polygonal faults is one of the main controlling mechanisms for the fluid flow development in the study area. Above the termination of faults, high amplitude anomalies are found within the interbedded debris flow deposits, implying entrapment of gas. Glacigenic deposits make up one of the main accumulation mechanisms in the study area.

The north-north-western part of the study area has not been subject to glacial deposition. Here deformations within the Naust Formation extend all the way to the seabed. Acoustic masking all the way to the seabed reflection is observed. However, because of the character of the seabed reflection, no clear pockmarks were found in relation to termination fault r fracture zones.

The 3D seismic data enabled identification and mapping of a gas-hydrate related bottom-simulation reflector (BSR). The BSR marks the base of the gas hydrate stability zone (BGHSZ). The BSR has a behaviour in which it crosscuts the sedimentary strata. Enhanced reflections terminate against the polarity-reversed BSR reflection. The enhanced reflections indicate the presence of free gas under the BGHSZ. The frequency distribution of the BSR does not show the expected frequency loss for the free gas zone beneath the BGHSZ. A possible explanation for this is proposed as follows: Acoustic pipes are observed to cut through the BSR, showing clear indications of fluid flow above the BSR. This might lead to gas leakage, reducing the amount of free gas trapped underneath the gas hydrates. It is suggested that these pipe structures are caused by localised advective fluid flux.

The formation and origin of the gas hydrate and the gas-hydrate related BSR within the study area seem to be closely related to the fluid flow in the area. A fluid flux of thermogenic origin is believed to be a result from the hydrothermal vents and sill intrusions in the area. However, biogenic methane flux from the Kai formation is also suggested as a source. With the geothermal gradients as estimated for the study area, the Kai Formation should be in the biogenic zone. The observed BSR appears between the modelled BGHSZ for 100% methane and the BGHSZ for 99% methane including 1% ethane. This supports the theory for the origin of the gas hydrate being a combination of thermogenic gases from deeper depths, and biogenic gases from the Kai Formation.

Literature

Akpabio, M. G. (2013). *Cold Flow in long distance subsea pipelines.* (Master of Science), NTNU - Norwegian University of Science and Technology.

Andreassen, K., Mienert, J., Bryn, P., & Singh, S. C. (2000). A Double Gas-Hydrate Related Bottom Simulating Reflector at the Norwegian Continental Margin. *Annals of the New York Academy of Sciences, 912*(1), 126-135. doi:10.1111/j.1749-6632.2000.tb06766.x

Andreassen, K., Nilssen, E. G., & Ødegaard, C. M. (2007). Analysis of shallow gas and fluid migration within the Plio-Pleistocene sedimentary succession of the SW Barents Sea continental margin using 3D seismic data. *Geo-Marine Letters, 27*(2-4), 155-171.

Badley, M. E. (1985). *Practical seismic interpretation* International Human Resources Development Corporation

Barker, J. W., & Gomez, R. K. (1989). Formation of Hydrates During Deepwater Drilling Operations. *Journal of Petroleum Technology, 41*(3). doi:10.2118/16130-PA

Berg, R. R. (1975). Capillary pressure in stratigraphic traps. *America Association of Petroleum Geologists - bulletin 59*, 939-956.

Berndt, C. (2005). Focused fluid flow in passive continental margins. *Philosophical Transactions of the Royal Society A: Mathematical, Physical and Engineering Sciences, 363*(1837), 2855-2871.

Berndt, C., Bünz, S., Clayton, T., Mienert, J., & Saunders, M. (2004). Seismic character of bottom simulating reflectors: examples from the mid-Norwegian margin. *Marine and Petroleum Geology, 21*(6), 723-733. doi:http://dx.doi.org/10.1016/j.marpetgeo.2004.02.003

Berndt, C., Bünz, S., & Mienert, J. (2003). Polygonal fault systems on the mid-Norwegian margin: a long-term source for fluid flow. *Geological Society, London, Special Publications, 216*(1), 283-290. doi:10.1144/gsl.sp.2003.216.01.18

Berndt, C., Planke, S., & Alvestad, E. T., F. Rasmussen, T. (2001). Seismic volcanostratigraphy of the Norwegian Margin: constraints on tectonomagmatic break-up processes. *Journal of the Geological Society, 158*, 413-426.

Biddle, K. T., & Wielchowsky, C. C. (1994). Hydrocarbon traps. *America Association of Petroleum Geologists - memoirs, 60*, 219-235.

Birkedal, K. A. (2013). *Empirical and Numerical Evaluation of Mechanisms in Gas Production from CH4-Hydrates.* (Philosophiae Doctor (PhD) Doctoral thesis), University of Bergen.

Bjørlykke, K. (2010). *Petroleum geoscience: From sedimentary environments to rock physics*: springer.

Blystad, P., Brekke, H., Færseth, R. B., Larsen, B. T., Skogseid, J., & Tørudbakken, B. (1995). *NPD-BULLETIN No 8, Structural elements of the Norwegian Continental Shelf - Part II: The Norwegian Sea Region*: The Norwegian Petroleum Directorate (NPD).

Bondevik, S., Løvholt, F., Harbitz, C., Mangerud, J., Dawson, A., & Svendsen, J. I. (2005). The Storegga Slide tsunami—comparing field observations with numerical simulations. *Marine and Petroleum Geology, 22*(1–2), 195-208. doi:http://dx.doi.org/10.1016/j.marpetgeo.2004.10.003

Bouriak, S., Vanneste, M., & Saoutkine, A. (2000). Inferred gas hydrates and clay diapirs near the Storegga Slide on the southern edge of the Vøring Plateau, offshore Norway. *Marine Geology, 163*(1–4), 125-148. doi:http://dx.doi.org/10.1016/S0025-3227(99)00115-2

Brekke, H. (2000). The tectonic evolution of the Norwegian Sea Continental Margin with emphasis on the Voring and More Basins: Dynamics of the Norwegian Margin. *The Geological Society of London, 167*, 327-378.

Brown, A. R. (2004). Interpretation of Three-Dimensional Seismic Data. *American Association of Petroleum Geologists and the Society of Exploration Geophysicists, Memoir 42*.

Bryn, P., Berg, K., Forsberg, C. F., Solheim, A., & Kvalstad, T. J. (2005). Explaining the Storegga Slide. *Marine and Petroleum Geology, 22*(1–2), 11-19. doi:http://dx.doi.org/10.1016/j.marpetgeo.2004.12.003

Bryn, P., Berg, K., Lien, R., & Solheim, A. (2005). Submarine slides on the Mid-Norwegian Continental Margin—A challenge to the oil industry. In J. P. N. E. E. Bjørn T.G Wandås & G. Felix (Eds.), *Norwegian Petroleum Society Special Publications* (Vol. Volume 12, pp. 255-263): Elsevier.

Bugge, T., Belderson, R. H., & Kenyon, N. H. (1988). The Storegga Slide. *Philosophical Transactions of the Royal Society of London A: Mathematical, Physical and Engineering Sciences, 325*(1586), 357-388. doi:10.1098/rsta.1988.0055

Bulat, J. (2005). Some considerations on the interpretation of seabed images based on commercial 3D seismic in the Faroe-Shetland Channel. *Basin Research, 17*(1), 21-42. doi:10.1111/j.1365-2117.2005.00253.x

Bünz, S., & Mienert, J. (2004). Acoustic imaging of gas hydrate and free gas at the Storegga Slide. *Journal of Geophysical Research: Solid Earth, 109*.

Bünz, S., Mienert, J., & Berndt, C. (2003). Geological controls on the Storegga gas-hydrate system of the mid-Norwegian continental margin. *Earth and Planetary Science Letters, 209*(3–4), 291-307. doi:http://dx.doi.org/10.1016/S0012-821X(03)00097-9

Cartwright, J., Huuse, M., & Aplin, A. (2007). Seal bypass systems. *AAPG bulletin, 91*(8), 1141-1166.

Cartwright, J., James, D., & Bolton, A. (2003). The genesis of polygonal fault systems: a review. *Geological Society, London, Special Publications, 216*(1), 223-243. doi:10.1144/gsl.sp.2003.216.01.15

Cartwright, J. A., & Dewhurst, D. N. (1998). Layer-bound compaction faults in fine-grained sediments. *Geological Society of America Bulletin, 110*(10), 1242-1257. doi:10.1130/0016-7606(1998)110<1242:lbcfif>2.3.co;2

Castagna, J. P. (1993). *Offset-dependent Reflectivity: Theory and Practice of AVO Analysis*: Society of Exploration Geophysicists.

Cathles, L. M., Su, Z., & Chen, D. (2010). The physics of gas chimney and pockmark formation, with implications for assessment of seafloor hazards and gas sequestration. *Marine and Petroleum Geology, 27*(1), 82-91. doi:http://dx.doi.org/10.1016/j.marpetgeo.2009.09.010

Chand, S., & Minshull, T. A. (2003). Seismic constraints on the effects of gas hydrate on sediment physical properties and fluid flow: a review. *Geofluids, 3*(4), 275-289.

Chand, S., Rise, L., Knies, J., Haflidason, H., Hjelstuen, B. O., & Bøe, R. (2011). Stratigraphic development of the south Vøring margin (Mid-Norway) since early Cenozoic time and its influence on subsurface fluid flow. *Marine and Petroleum Geology, 28*(7), 1350-1363. doi:http://dx.doi.org/10.1016/j.marpetgeo.2011.01.005

Chopra, S., & Marfurt, K. K. (2005). Seismic attributes - A historical perspective. *GEOPHYSICS, 70*(5), 3SO -28SO.

Clennel, M. B., Judd, A., & Hovland, M. (2000). Movement and accumulation of methane in marine sediments: relation to gas hydrate systems *Natural Gas Hydrate in Oceanic and Permafrost Environments*. Dordrecth: Kluwer Academic Publishers

Clennell, M. B., Hovland, M., Booth, J. S., Henry, P., & Winters, W. J. (1999). Formation of natural gas hydrates in marine sediments: 1. Conceptual model of gas hydrate growth conditioned by host sediment properties. *Journal of Geophysical Research: Solid Earth, 104*(B10), 22985-23003. doi:10.1029/1999JB900175

Dalland, A., Worsley, D., & Ofstad, K. (1988). A lithostratigraphic scheme for the Mesozoic and Cenozoic succesions offshore mid- and northern Norway. *Norwegian Petroleum Directorate, NPD - bulletin 4*.

Demirbas, A. (2010). Methane hydrates as potential energy resource: Part 1 – Importance, resource and recovery facilities. *Energy Conversion and Management, 51*(7), 1547-1561. doi:http://dx.doi.org/10.1016/j.enconman.2010.02.013

Dewhurst, D. N., Cartwright, J. A., & Lonergan, L. (1999). The development of polygonal fault systems by syneresis of colloidal sediments. *Marine and Petroleum Geology, 16*(8), 793-810. doi:http://dx.doi.org/10.1016/S0264-8172(99)00035-5

Dumke, I., Berndt, C., Crutchley, G. J., Krause, S., Liebetrau, V., Gay, A., & Couillard, M. (2014). Seal bypass at the Giant Gjallar Vent (Norwegian Sea): Indications for a new phase of fluid venting at a 56-Ma-old fluid migration system. *Marine Geology, 351*, 38-52. doi:http://dx.doi.org/10.1016/j.margeo.2014.03.006

Durand, B. (1988). Understanding of HC migration in sedimentary basins (present state of knowledge). *Organic Geochemistry, 13*(1–3), 445-459. doi:http://dx.doi.org/10.1016/0146-6380(88)90066-6

EIA. (2013). *International Energy Outlook 2013*. Retrieved from http://www.eia.gov/forecasts/ieo/pdf/0484(2013).pdf

England, W. A., Mackenzie, A. S., Mann, D. M., & Quigley, T. M. (1987). The movement and entrapment of petroleum fluids in the subsurface. *Geological Society of London, 144*, 327-347.

Etiope, G., & Schoell, M. (2014). Abiotic Gas: Atypical, But Not Rare. *Elements, 10*(4), 291-296. doi:10.2113/gselements.10.4.291

Etiope, G., & Sherwood Lollar, B. (2013). Abiotic methane on earth *Reviews of Geophysics, 51*(2), 276-299. doi:10.1002/rog.20011

Fossen, H., & Gabrielsen, R. H. (2005). *Strukturgeologi*. Bergen: Fagbokforlaget Vigmostad og Bjørke AS.

Gay, A., Lopez, M., Berndt, C., & Seranne, M. (2007). Geological controls on focused fluid flow associated with seafloor seeps in the Lower Congo Basin. *Marine Geology, 244*(1), 68-92.

Grassle, J. F. (1985). Hydrothermal Vent Animals: Distribution and Biology. *Science, 229*(4715), 713-717. doi:10.1126/science.229.4715.713

Gudmundsson, J. S. (2002). *Cold Flow Hydrate Technology*. Paper presented at the 4th International Conference on Gas Hydrates, Yokohama.

Gudmundsson, J. S., & Børrehaug, A. (1996). *Frozen Hydrate for Transport of Natural Gas*. Paper presented at the 2nd International Conference on Natural Gas Hydrate, Toulouse, France.

Haacke, R. R., Westbrook, G. K., & Hyndman, R. D. (2007). Gas hydrate, fluid flow and free gas: Formation of the bottom-simulating reflector. *Earth and Planetary Science Letters, 261*(3–4), 407-420. doi:http://dx.doi.org/10.1016/j.epsl.2007.07.008

Haflidason, H., Lien, R., Sejrup, H. P., Forsberg, C. F., & Bryn, P. (2005). The dating and morphometry of the Storegga Slide. *Marine and Petroleum Geology, 22*(1–2), 123-136. doi:http://dx.doi.org/10.1016/j.marpetgeo.2004.10.008

Hammerschmidt, E. G. (1934). Formation of Gas Hydrates in Natural Gas Transmission Lines. *Industrial & Engineering Chemistry, 26*(8), 851-855. doi:10.1021/ie50296a010

Hansen, J. P. V., Cartwright, J. A., Huuse, M., & Clausen, O. R. (2005). 3D seismic expression of fluid migration and mud remobilization on the Gjallar Ridge, offshore mid-Norway. *Basin Research, 17*(1), 123-139. doi:10.1111/j.1365-2117.2005.00257.x

Heggland, R. (1997). Detection of gas migration from a deep source by the use of exploration 3D seismic data. *Marine Geology*, *137*(1–2), 41-47. doi:http://dx.doi.org/10.1016/S0025-3227(96)00077-1

Heggland, R. (1998). Gas seepage as an indicator of deeper prospective reservoirs. A study based on exploration 3D seismic data. *Marine and Petroleum Geology, 15*(1), 1-9. doi:http://dx.doi.org/10.1016/S0264-8172(97)00060-3

Hindle, A. D. (1997). Petroleum migration pathways and charge concentration; a three-dimensional model. *AAPG bulletin, 81*(9), 1451-1481. Retrieved from http://aapgbull.geoscienceworld.org/content/81/9/1451.abstract

Hjelstuen, B. O., Eldholm, O., & Skogseid, J. (1997). Vøring Plateau diapir fields and their structural and depositional settings. *Marine Geology*, *144*(1–3), 33-57. doi:http://dx.doi.org/10.1016/S0025-3227(97)00085-6

Hjelstuen, B. O., Haflidason, H., Sejrup, H. P., & Nygård, A. (2010). Sedimentary and structural control on pockmark development—evidence from the Nyegga pockmark field, NW European margin. *Geo-Marine Letters, 30*(3-4), 221-230. doi:10.1007/s00367-009-0172-4

Hjelstuen, B. O., Sejrup, H. P., Haflidason, H., Berg, K., & Bryn, P. (2004). Neogene and Quaternary depositional environments on the Norwegian continental margin, 62°N–68°N. *Marine Geology, 213*(1–4), 257-276. doi:http://dx.doi.org/10.1016/j.margeo.2004.10.009

Hjelstuen, B. O., Sejrup, H. P., Haflidason, H., Nygård, A., Ceramicola, S., & Bryn, P. (2005). Late Cenozoic glacial history and evolution of the Storegga Slide area and adjacent slide flank regions, Norwegian continental margin. *Marine and Petroleum Geology, 22*(1–2), 57-69. doi:http://dx.doi.org/10.1016/j.marpetgeo.2004.10.002

Holditch, S. A., & Chianelli, R. R. (2008). Factors That Will Influence Oil and Gas Supply and Demand in the 21st Century. *MRS Bulletin, 33*, 317-323.

Hornbach, M. J., Holbrook, W. S., Gorman, A. R., Hackwith, K. L., Lizarralde, D., & Pecher, I. (2001). Direct seismic detection of methane hydrate on the Blake Ridge. *GEOPHYSICS, 68*(1), 92-100.

Houghton, J. T. (2009). *Global Warming - the complete briefing*. Cambridge; New York: Cambridge University Press.

Hovland, M., Gardner, J. V., & Judd, A. (2002). The significance of pocmarks to understanding fluid flow processes and geohazards. *Geofluids, 2*, 127-136.

Hustoft, S., Dugan, B., & Mienert, J. (2009). Effects of rapid sedimentation on developing the Nyegga pockmark field: Constraints from hydrological modeling and 3-D seismic data, offshore mid-Norway. *Geochemistry, Geophysics, Geosystems, 10*(6). doi:http://dx.doi.org/10.1029/2009GC002409

Hustoft, S., Mienert, J., Bünz, S., & Nouzé, H. (2007). High-resolution 3D-seismic data indicate focussed fluid migration pathways above polygonal fault systems of the mid-Norwegian margin. *Marine Geology*, *245*(1), 89-106.

IEA. (2013). *World Energy Outlook 2013*. Retrieved from

Ilahi, M. (2006). *Evaluation of Cold Flow Concepts.* (Master of Science thesis), NTNU - Norwegian University of Science and Technology.

IPCC, Solomon, S., Qin, D., Manning, M., Chen, Z., Marquis, M., Averyt, K. B., Tignor, M., & Miller, H. L. (2007). *Climate change 2007 : the physical science basis : contribution of Working Group I to the Fourth Assessment Report of the Intergovernmental Panel on Climate Change*. Retrieved from IPPC 2007:

Ivanov, M., Blinova, V., Kozlova, E., Westbrook, G. K., A. Mazzini, & Minshull, T. N., H. (2007). First sampling of gas hydrate from the Vøring Plateau. *EOS, Transactions - American Geophysical Union, 88*(19), 209-212. doi:10.1029/2007EO190001

Jamtveit, B., Svensen, H., Podladchikov, Y. Y., & Planke, S. (2004). Hydrothermal vent complexes associated with sill intrusions in sedimentary basins *The Geological Society of London, Physical Geology of High-Level Magmatic Systems(Special publications)*, 233-241.

Judd, A., & Hovland, M. (2007). *Seabed fluid flow - The impact on geology, biology and the marine environment* New York: Cambridge University Press.

Judd, A. G., & Hovland, M. (1992). The evidence of shallow gas in marine sediments. *Continental Shelf Research, 12*(10), 1081-1095. doi:http://dx.doi.org/10.1016/0278-4343(92)90070-Z

Jung, W.-Y., & Vogt, P. R. (2004). Effects of bottom water warming and sea level rise on Holocene hydrate dissociation and mass wasting along the Norwegian-Barents Continental Margin. *Journal of Geophysical Research: Solid Earth, 109*(B6).

Kvenvolden, K. A. (1993). Gas hydrates—geological perspective and global change. *Reviews of Geophysics, 31*(2), 173-187. doi:10.1029/93RG00268

Kvenvolden, K. A. (1998). A primer on the geological occurrence of gas hydrate. *Geological Society of London, Special Publications, 137*, 9-30. doi:10.1144/GSL.SP.1998.137.01.02

Kvenvolden, K. A. (1999). Potential effects of gas hydrate on human welfare. *Proceedings of the National Academy of Sciences, 96*(7), 3420-3426. doi:10.1073/pnas.96.7.3420

Ligtenberg, J. H. (2005). Detection of fluid migration pathways in seismic data: implications for fault seal analysis. *Basin Research, 17*(1), 141-153.

Liu, B., Pan, H., Wang, X., Li, F., Sun, C., & Chen, G. (2013). Evaluation of Different CH4-CO2 Replacement Processes in Hydrate-Bearing Sediments by Measuring P-Wave Velocity. *Energies, 6*(12), 6242. Retrieved from http://www.mdpi.com/1996-1073/6/12/6242

Lonergan, L., Cartwright, J., & Jolly, R. (1998). The geometry of polygonal fault systems in Tertiary mudrocks of the North Sea. *Journal of Structural Geology, 20*(5), 529-548. doi:http://dx.doi.org/10.1016/S0191-8141(97)00113-2

Løseth, H., Gading, M., & Wensaas, L. (2009). Hydrocarbon leakage interpreted on seismic data. *Marine and Petroleum Geology, 26*(7), 1304-1319. doi:http://dx.doi.org/10.1016/j.marpetgeo.2008.09.008

Løseth, H., Wensaas, L., Arntsen, B., Hanken, N.-M., Basire, C., & Graue, K. (2011). 1000 m long gas blow-out pipes. *Marine and Petroleum Geology, 28*(5), 1047-1060. doi:http://dx.doi.org/10.1016/j.marpetgeo.2010.10.001

MacKay, M. E., Jarrard, R. D., Westbrook, G. K., & Hyndman, R. D. (1994). Origin of bottom-simulating reflectors: Geophysical evidence from the Cascadia accretionary prism. *Geology, 22*(5), 459-462. Retrieved from http://geology.gsapubs.org/content/22/5/459.abstract

Magoon, L. B., & Dow, W. G. (1994). The Petroleum System. *The petroleum system—From source to trap: AAPG Memoir, 60*, 3-24.

Makogon, Y. F. (2010). Natural gas hydrates – A promising source of energy. *Journal of Natural Gas Science and Engineering, 2*(1), 49-59. doi:http://dx.doi.org/10.1016/j.jngse.2009.12.004

Marshall, J., & Plumb, R. A. (2008). *Atmosphere, Ocean and Climate Dynamics*: Elsevier Academic Press

Matthews, M. D. (1996). Migration - A view from the top. In D. Schumacher & M. A. Abrams (Eds.), *Hydorcarbon Migration and its Near-Surface Expression*: American Association of Petroleum Geologists, memoir 66.

Max, M. D. (2003). *Natural Gas Hydrate: In Oceanic and Permafrost Environments*. Netherlands: Kluwer Academic Publishers.

McIver, R. D. (1982). Role of Naturally Occurring Gas Hydrates in Sediment Transport. *AAPG bulletin, 66*(6), 789-792.

Mienert, J., Vanneste, M., Bünz, S., Andreassen, K., Haflidason, H., & Sejrup, H. P. (2005). Ocean warming and gas hydrate stability on the mid-Norwegian margin at the Storegga Slide. *Marine and Petroleum Geology, 22*(1–2), 233-244. doi:http://dx.doi.org/10.1016/j.marpetgeo.2004.10.018

Moridis, G. J. C., T. S (2003). *Strategies for gas production from hydrate accumulations under various geological and reservoir conditions.* Paper presented at the TOUGH Symposium 2003, Lawrence Berkeley National Laboratory, Berkeley, California,.

NPD. (2012). *CO2 Storage Atlas - Norwegian Sea*: Norwegian Petroleum Directorate.

NPDa. (2015). Wellbore 6605/8-1. Retrieved from http://www.npd.no/engelsk/cwi/pbl/wellbore_composite_logs/4984.pdf

NPDb. (2015). Wellbore 6605/8-2. Retrieved from http://www.npd.no/engelsk/cwi/pbl/wellbore_composite_logs/5812.pdf

NPDc. (2015). Wellbore 6605/1-1. Retrieved from http://www.npd.no/engelsk/cwi/pbl/wellbore_composite_logs/5979.pdf

Osborne, M. J., & Swarbrick, R. E. (1997). Mechanisms for Generating Overpressure in Sedimentary Basins: A Reevaluation. *American Association of Petroleum Geologists - bulletin, 81*(6).

Ottesen, D., Rise, L., Andersen, E. S., & Bugge, T. E., T. . (2009). Geological evolution of the Norwegian continental shelf between 61ºN and 68ºN during the last 3 million years. *Norwegian Journal of Geology, 89*, 251-265.

Pecher, I. A., Henrys, S. A., Wood, W. T., Kukowski, N., Crutchley, G. J., Fohrmann, M., Kilner, J., Senger, K., Gorman, A. R., Coffin, R. B., Greinert, J., & Faure, K. (2010). Focussed fluid flow on the Hikurangi Margin, New Zealand — Evidence from possible local upwarping of the base of gas hydrate stability. *Marine Geology, 272*(1–4), 99-113. doi:http://dx.doi.org/10.1016/j.margeo.2009.10.006

Pecher, I. A., Kukowski, N., Huebscher, C., Greinert, J., & Bialas, J. (2001). The link between bottom-simulating reflections and methane flux into the gas hydrate stability zone – new evidence from Lima Basin, Peru Margin. *Earth and Planetary Science Letters, 185*(3–4), 343-354. doi:http://dx.doi.org/10.1016/S0012-821X(00)00376-9

Planke, S., Rasmussen, T., Rey, S. S., & Myklebust, R. (2005). *Seismic characteristics and distribution of volcanic intrusions and hydrothermal vent complexes in the Vøring and Møre basins*. Paper presented at the Petroleum Geology: North-West Europe and Global Perspectives-Proceedings of the 6th Petroleum Geology Conference, London.

Plaza-Faverola, A., Bünz, S., & Mienert, J. (2010). Fluid distributions inferred from P-wave velocity and reflection seismic amplitude anomalies beneath the Nyegga pockmark field of the mid-Norwegian margin. *Marine and Petroleum Geology, 27*(1), 46-60. doi:http://dx.doi.org/10.1016/j.marpetgeo.2009.07.007

Plaza-Faverola, A., Bünz, S., & Mienert, J. (2011). Repeated fluid expulsion through sub-seabed chimneys offshore Norway in response to glacial cycles. *Earth and Planetary Science Letters, 305*(3–4), 297-308. doi:http://dx.doi.org/10.1016/j.epsl.2011.03.001

Plaza-Faverola, A., Bünz, S., & Mienert, J. (2012). The free gas zone beneath gas hydrate bearing sediments and its link to fluid flow: 3-D seismic imaging offshore mid-Norway. *Marine Geology, 291–294*, 211-226. doi:http://dx.doi.org/10.1016/j.margeo.2011.07.002

Raum, T., Mjelde, R., Shimamura, H., Murai, Y., Bråstein, E., Karpuz, R. M., Kravik, K., & Kolstø, H. J. (2006). Crustal structure and evolution of the southern Vøring Basin and Vøring Transform Margin, NE Atlantic. *Tectonophysics, 415*(1–4), 167-202. doi:http://dx.doi.org/10.1016/j.tecto.2005.12.008

Reynolds, J. M. (2011). *An introduction to Applied and Environmental Geophysics* (2nd ed.): Wiley-Blackwell, John Wiley & Sons, Ltd.

Rise, L., Ottesen, D., Berg, K., & Lundin, E. (2005). Large-scale development of the mid-Norwegian margin during the last 3 million years. *Marine and Petroleum Geology, 22*(1–2), 33-44. doi:http://dx.doi.org/10.1016/j.marpetgeo.2004.10.010

Rise, L., Ottesen, D., Longva, O., Solheim, A., Andersen, E. S., & Ayers, S. (2006). The Sklinnadjupet slide and its relation to the Elsterian glaciation on the mid-Norwegian margin. *Marine and Petroleum Geology, 23*(5), 569-583. doi:http://dx.doi.org/10.1016/j.marpetgeo.2006.05.005

Ruppel, C., & Noserale, D. (2012). Gas Hydrates and Climate Warming—Why a Methane Catastrophe Is Unlikely.

Schlumberger. (2010). *Petrel 2010 - Interpreter's Guide to Seismic Attributes*

Schowalter, T. T. (1979). Mechanics of secondary hydrocarbon migration and entrapment *American Association of Petroleum Geologists - bulletin 63*, 723-760.

Schroeder, D. V. (2000). *An introduction to thermal physics*. United States: Addison Wesley Longman.

Selley, R. C. (1998). *Elements of petroleum geology*: Gulf Professional Publishing.

Senger, K. (2009). *First-order estimation of in-place natural gas resources at the Nyegga gas hydrate prospect, mid-Norwegian Margin.* (Master degree Master's Thesis in Geology), UiT The Arctic University of Norway (University of Tromsø).

Sheriff, R. E. (1985). Aspects of Seismic Resolution. *American Association of Petroleum Geologists, Memoir 39*(Seismic Stratigraphy II).

Sheriff, R. E. (2006). *Enclyclopedic dictionary of exploration geophysics, 4th edition*. Tulsa: Society of Exploration Geophysicists.

Sheriff, R. E., & Geldart, L. P. (1995). *Exploration Seismology* (2nd ed.). New York, United States of America: Cambridge University Press.

Sherwood Lollar, B., Lacrampe-Couloume, G., Slater, G. F., Ward, J., Moser, D. P., Gihring, T. M., Lin, L. H., & Onstott, T. C. (2006). Unravelling abiogenic and biogenic sources of methane in the Earth's deep subsurface. *Chemical Geology, 226*(3–4), 328-339. doi:http://dx.doi.org/10.1016/j.chemgeo.2005.09.027

Sloan, E. D. (1998). Gas Hydrates: Review of Physical/Chemical Properties. *Energy & Fuels, 12*(2), 191-196. doi:10.1021/ef970164+

Sloan, E. D. (2005). A changing hydrate paradigm—from apprehension to avoidance to risk management. *Fluid Phase Equilibria, 228–229*, 67-74. doi:http://dx.doi.org/10.1016/j.fluid.2004.08.009

Sloan, E. D., & Koh, C. A. (2007). *Clathrate hydrates of natural gases*: CRC press ,Taylor & Francis Group.

Sloan, E. D. J., Koh, C. A., & Sum, A. K. (2010). Gas Hydrate Stability and Sampling: The Future as Related to the Phase Diagram. *Energies, 3*(12), 1991. Retrieved from http://www.mdpi.com/1996-1073/3/12/1991

Taheri, Z., Shabani, M. R., Nazari, K., & Mehdizaheh, A. (2014). Natural gas transportation and storage by hydrate technology: Iran case study. *Journal of Natural Gas Science and Engineering, 21*, 846-849. doi:http://dx.doi.org/10.1016/j.jngse.2014.09.026

Taner, M. T., Koehler, F., & Sheriff, R. E. (1979). Complex seismic trace analysis. *GEOPHYSICS, 44*(6), 1041-1063. doi:doi:10.1190/1.1440994

Taner, M. T., & Sheriff, R. E. (1977). Application of Amplitude, Frequency, and Other Attributes to Stratigraphic and Hydrocarbon Determination: Section 2. Application of Seismic Reflection Configuration to Stratigraphic Interpretation. *American Association of Petroleum Geologists, Memoir 26 - Seismic Stratigraphy-Applications to Hydrocarbon Exploration*, 301-327.

Thrasher, J., Fleet, A. J., Hay, S. J., Hovland, M., & Düppenbecker, S. (1996). Understanding Geology as the Key to Using Seepage in Exploration: The Spectrum of Seepage Styles. In D. A. Schumarcher, M. A. (Ed.), *Memoir 66*: The American Association of Petroleum Geologists.

Tissot, B. P., & Welte, D. H. (1978). *An Introduction to Migration and Accumulation of Oil and Gas*: Springer Berlin Heidelberg.

Tissot, B. P., & Welte, D. H. (1984). Petroleum formation and occurrence.

Vadakkepuliyambatta, S., Bünz, S., Mienert, J., & Chand, S. (2013). Distribution of subsurface fluid-flow systems in the SW Barents Sea. *Marine and Petroleum Geology, 43*, 208-221.

Vanneste, M., De Batist, M., & Golmshtok, A. K., A.

Versteeg, W. (2001). Multi-frequency seismic study of gas hydrate-bearing sediments in Lake Baikal, Siberia. *Marine Geology, 172*(1-2), 1-21.

Veeken, P. C. H. (2007). *Seismic stratigraphy, basin analysis and reservoir characterisation* (Vol. 37): Elsevier.

Veeken, P. C. H., & Moerkerken, B. v. (2013). *Seismic Stratigraphy and Depositional Facies Models*. Houten, The Netherlands: EAGE Publications bv.

Westbrook, G. K., Exley, R., Minshull, T. A., Nouze, H., Gailler, A., Jose, T., Ker, S., & Plaza-Faverola, A. (2008). *High-resolution 3D seismic investigations of hydrate-bearing fluid escape chimneys in the Nyegga region of the Voring Plateau, Norway*. Paper presented at the 6th International Conference on Natural Gas Hydrates, Vancouver BC, Canada.

Yakushev, V. S., & Collett, T. S. (1992). *Gas Hydrates In Arctic Regions: Risk To Drilling And Production* Paper presented at the The Second International Offshore and Polar Engineering Conference, 14-19 June, San Francisco, California, USA

Zerpa, L. E., Salager, J.-L., Koh, C. A., Sloan, E. D., & Sum, A. K. (2011). Surface Chemistry and Gas Hydrates in Flow Assurance. *Industrial & Engineering Chemistry Research, 50*(1), 188-197. doi:10.1021/ie100873k